# Dual-spray Synthesis and Reactions

Shaan Rashid

Thesis submitted to the
Faculty of Graduate & Postdoctoral Studies
in partial fulfillment of the requirements for the
MSc. degree in Chemistry

Department of Chemistry and Biomolecular Sciences
Faculty of Science
University of Ottawa

# Abstract

By using two electrospray emitters containing different solutions ("dual-spray") we have recently conducted in-source hydrogen/deuterium exchange (HDX) reactions and synthesized organometallic species. For dual-spray HDX reactions, peptide and protein solutions were electrosprayed through one emitter and the deuterating agent $D_2O$ through the secondary electrospray emitter. Clear shifts in isotope distributions indicated hydrogen-deuterium exchange occurring within the ion source. By ion mobility, simultaneous deuterium exchange for two isobaric species, the oxytocin monomer and dimer, was observed. Lysozyme has a linear relation between the charge state and the average number of exchanges, indicating that lysozyme becomes increasingly unfolded as the charge state increases. Based on deuterium uptake data and the lack of a temperature dependence, the dual-spray HDX reaction is thought to occur mostly in the gas phase. Tris(2,2'-bipyridine)ruthenium(II) and similar complexes containing the 1,10-phenanthroline ligand were formed by spraying a ligand solution and the ruthenium trichloride solution through two independent ESI emitters. This was confirmed by comparing ion mobility drift time, mass spectra, and CID fragmentation with the reference standard compounds. Tris(2,2'-bipyridine)iron(II), tris(1,10-phenantroline)iron(II) and mixed ligand complexes of iron(II) formed by dual-spray showed two additional hydrogens bonded to the complex. By CID, these unique gas phase complexes showed similar initial ligand loss to the reference standards however the secondary ligand loss showed dissimilar dissociation channels and energetics. Using DFT calculations, geometry optimizations for the $[Fe(phen)_3 + 2H]^{2+}$ complex and its fragment ions were done. After the initial ligand loss, the additional hydrogens are believed to transfer to the central iron atom. The relative energy of the dissociation channels showed good agreement with experimental breakdown curves.

# Acknowledgements

First and foremost, I would like to thank my supervisor, Dr. Paul Mayer, for giving me the opportunity to conduct this research as a part of my Master's in Chemistry. I greatly appreciate the help you have given me while discussing the results of the experiments that I conducted. Thank you for always being available to respond to any questions I had.

Thank you Ameneh Gholami, Sean Overton, and Sharon Curtis for taking the time to train me on the operation of the Synapt. I would also like to thank Sean Overton (again), Bihac Mazigh, and Patrick Leal for being excellent collaborators and working very diligently so that our work can be published. Thank you Eduardo Solano for explaining computational methods to me and answer any questions I had regarding Gaussian software. A special thank you to Sander Mommers, who fixed any instrumental problems with the Synapt.

In addition, I would like to acknowledge all other members of the Mayer group including: Justin Renaud, Mosammat Khan, Sabria Mohamed, Iden Djavani, Barbara Francisco, Peter Chen, Jaleh Halvachizadeh, Jeffery Butson, Naomi Mattli-Lewis, and Anaïs Ryc. To all members of the lab, it was a pleasure to get to know all of you. Thank you for your helpfulness and support. I hope you all succeed in your future endeavors.

Last but certainly not least, I would like to thank my parents and brother for being helpful and supportive throughout my Masters.

# Table of Contents

# List of Figures and Tables

## Appendix

# List of Abbreviations

| | |
|---|---|
| ESI | Electrospray Ionization |
| HDX | Hydrogen/Deuterium Exchange |
| MS | Mass spectrometry |
| DESI | Desorption Electrospray Ionization |
| EESI | Extractive Electrospray Ionization |
| bpy | 2,2’-bipyridine |
| phen | 1,10-phenanthroline |
| CID | Collision Induced Dissociation |
| IEM | Ion Evaporation Model |
| CRM | Charge Residue Model |
| CEM | Charge Ejection Model |
| TOF | Time of Flight |
| IMS | Ion Mobility Spectrometry |
| TWIMS | Travelling Wave Ion Mobility Spectrometry |
| ECD | Electron Capture Dissociation |
| RRKM | Rice–Ramsperger–Kassel–Marcus |
| MALDI | Matrix Assisted Laser Desorption Ionization |
| CSD | Charge State Distribution |
| U | Unfolded |
| F | Folded |
| PES | Potential Energy Surface |
| DFT | Density Functional Theory |
| HPLC | High Performance Liquid Chromatography |
| IR | Infrared |
| NMR | Nuclear Magnetic Resonance |
| Phe-Leu-Glu-Glu-Leu | Phenylalanine-Leucine-Glutamic Acid-Glutamic Acid-Leucine |

# Chapter 1. Introduction

## 1.1 Objective

Electrospray ionization (ESI) is one of the most effective ionization sources for introducing samples into a mass spectrometer. However, the charged microdroplets generated by ESI can cause unwanted side reactions due to increasing concentration of reagents and collision frequencies. Increased reaction rates within electrospray droplets may cause unwanted complications during sample analysis. This property of ESI can be exploited to conduct specific reactions within the ion source of the mass spectrometer. The goal of this research is to conduct specific reactions within the ESI source by electrospraying two different solutions through two independent ESI emitters, a process we have termed "dual-spray". The first series of reactions involves peptide and protein hydrogen/deuterium exchange (HDX) reactions which is used to probe gas phase conformations of these species. Dual-spray HDX reactions are compared to solution phase HDX reactions to determine its effectiveness for probing gas phase structures. Synthesis of organometallic species, specifically the formation of transition metal-pyridyl complexes, is another reaction type that is investigated using the dual-spray reaction. Comparing the spectral characteristics of reference standards allow for the characterization of the products generated by the dual-spray reaction.

## 1.2 ESI reaction rates and in-source reactions

Chemical reactions within droplets are typically used to compartmentalize reactions in small volumes (femtoliter to microliter) in order to provide rapid mixing of reagents, control the time scale of reactions, and regulate temperature and interfacial properties. The use of microfluidic devices allows for droplets to be used as micro-reactors[1]. Since ESI sources utilize charged droplets to generate gas phase ions, they can also be used to conduct reactions at elevated rates. Due to solvent evaporation in ESI droplets, the concentration of analytes and the pH within the charged droplets reach extreme values[2]. Accelerated bimolecular reaction rates within electrospray droplets have been reported in desorption electrospray ionization (DESI) experiments due to the increased concentration of reagents and collision frequencies within charged microdroplets[2]. Taking advantage of higher reaction rates, synthesis of 1,4-dihydropyridine derivatives via the Hantzch reaction can occur in electrosprayed droplets from a nano-spray source[3]. ESI has also been used for the controlled synthesis of transition-metal complex/solvent clusters by using a solvent vapor nitrogen purge[4]. In-source hydrogen-deuterium exchange (HDX) reactions by saturating the ESI source with vapors of a deuterating agent have been explored by Kostyukevich and co-workers[5] who found that the solvent composition of the charged microdroplets was indeed changed. Formation of unique gas phase species can also be achieved using ESI. Cluster ions formed by ESI are an example of distinctive gas phase species that can be generated by ESI. Arginine cluster ions with up to 24 arginine molecules have been shown to be formed by the electrospray process[6]. Also ESI is known to form organometallic species which may not be present in solution; transition metal-polyether-pyridyl mixed ligand complexes have been generated via ESI despite the large difference in the binding constants of the polyether and pyridyl ligands in solution[7] . Collectively, these experiments demonstrate that ESI is a dynamic process and charged microdroplets can be used as reaction vessels.

For this research, the Synapt G1 HDMS instrument was used. This machine is an ion mobility mass spectrometer which is equipped with a dual electrospray source. Dual electrospray emitters, which are typically used for accurate mass measurements on the Synapt G1 mass spectrometer, can be used for in-source reactions by electrospraying two separate solutions through the individual emitters. Ion/ion reactions can be carried out using a dual electrospray apparatus with opposite polarities on each ESI emitter [8], [9]. Covalent labelling of protonated peptides using 4-formyl-1,3-benzenedisulfonic acid (FBDSA) anions can be achieved using a dual-spray apparatus for enhanced ultraviolet dissociation[10]. The ambient ionization technique known as extractive electrospray ionization (EESI) also uses a dual emitter setup to analyze untreated milk[11], urine[11], and non-volatile compounds in breath[12].

We have performed in-source hydrogen deuterium exchange (HDX) reactions using the established Waters source design on the Synapt G1 instrument which implements two electrospray emitters[13]. Also attempted in this research is the synthesis of various metal-pyridyl complexes by spraying two distinct solutions through two independent electrospray emitters ("dual-spray"). Figure 1.1 shows a diagram of the dual-electrospray source used for the reactions conducted.  The dual-spray HDX reactions and dual-spray synthesis reactions we have explored will be discussed throughout this dissertation.

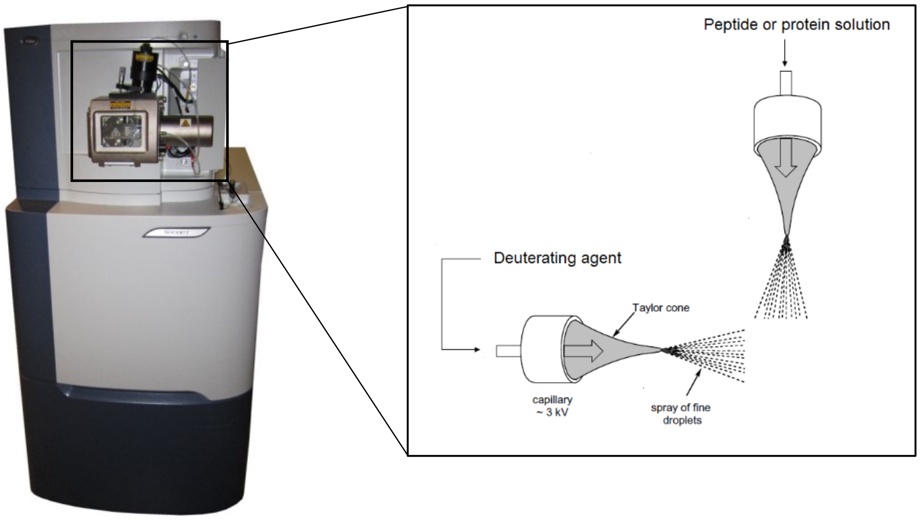

**Figure 1.1** Image of Synapt G1 HDMS instrument used and schematic diagram of the dual-electrospray apparatus used. In this case, the dual-spray hydrogen-deuterium exchange (HDX) reaction is shown.

## 1.3 Hydrogen Deuterium Exchange (HDX) Mass spectrometry

Hydrogen/deuterium exchange (HDX) mass spectrometry serves as an important tool for probing protein structure and dynamics[14]. In recent years, it has become one of the most prominent tools for the characterization of a protein's structure and it is commonly used to study protein interactions with small molecules, other proteins, and DNA/RNA[15]. The principle of HDX relies on the fact that hydrogen atoms covalently bonded to heteroatoms such as nitrogen, oxygen, and sulfur are labile and thus can exchange with deuterium when exposed to a deuteration agent such as $D_2O$. Exchange may occur with labile hydrogens of the amino acid side chains and the backbone amides; the latter is more important for probing protein structure. Typically, backbone amide hydrogens that are within natively folded elements (α helices and β sheets) of the protein experience very slow exchange with deuterium since these amides are involved in intramolecular hydrogen bonding and access of the solvent is restricted[16]. The amides that are easily accessible to the solvent and not involved in hydrogen bonding exchange at a much faster rate.

The rate of backbone amide exchange depends on four factors: pH, temperature, solvent accessibility and intramolecular hydrogen bonding (rate constant $k_2$ in Equation 1). The kinetics of an HDX experiment can be represented by the reaction scheme presented in Equation 1,

$$\textbf{(1)} \qquad F_H \underset{k_{-1}}{\overset{k_1}{\rightleftharpoons}} U_H \xrightarrow[D_2O]{k_2} U_D \underset{k_{-1}'}{\overset{k_1'}{\rightleftharpoons}} F_D$$

where F represents the folded conformation of a protein and U represents an unfolded conformation[15]. The $k_1$ and $k_{-1}$ values represent the rate constants for the unfolding and folding events respectively for a protein. The unfolding reaction has the equilibrium constant $K_{op}$ which has the expression

$$\textbf{(2)}\ K_{op} = \frac{k_1}{k_{-1}}$$

The kinetic isotope effect is observed when the ratio of $k_1/k_1'$ is not equal to 1. The exchange of hydrogen can follow two different kinetic regimes, EX1 or EX2 kinetics. When $k_{-1} >> k_2$, EX2 kinetics are observed. In the case of EX2 kinetics, the protein must reach the short-lived partially unfolded state multiple times in order for exchange reactions to occur[17]. EX2 kinetics is described by the expression

$$\textbf{(3)} \qquad k_{HDX} = \frac{k_1 k_2}{k_{-1}} = K_{op} k_2$$

In the mass spectrum of a protein demonstrating EX2 kinetics, there is a single ion population representing the protein with a gradual increase in average mass as the incubation time within the deuterating agent increases. EX1 kinetics is observed when $k_{-1} << k_2$, which implies that exchange reactions can occur during a single unfolding event[18]. Under physiological conditions, EX1 kinetics is rarely observed for proteins since the majority of the population has a folded conformation. Typically, EX1 kinetics is only observed under denaturing conditions such as low pH or exposure to denaturants which cause protein unfolding. EX1 kinetics is described by the following expression

$$\textbf{(4)} \qquad k_{HDX} = k_1$$

Proteins demonstrating EX1 kinetics have multiple populations in the mass spectrum.

In general, there exists two strategies to conduct HDX studies on proteins, the *continuous labeling* strategy and *pulsed HDX*[17]. The *continuous labeling* strategy involves the incubation of a protein in its native state in $D_2O$ and deuteration levels are monitored as a function of time. After the incubation period, the exchange reaction is quenched by acidifying the solution to pH

2.5[16]. This is followed by cleavage of the protein with an acid-stable protease such as pepsin. Reverse-phase HPLC is used to separate the resulting peptides and they are subsequently analyzed by ESI-MS. *Pulsed HDX* can be used to study protein folding intermediates at well-defined time points during a folding event. This is accomplished using continuous-flow mixing devices which can expose the protein to a short-lived HDX pulse (on the order of milliseconds). By varying the time interval at which the measurements are taken, it is possible to probe the short-lived folding intermediates that occur between the folded and unfolded states[17]. HDX reactions can also be done in the gas phase using gaseous $ND_3$[19].

The dual-spray HDX method takes advantage of the established Waters source design which implements a secondary ESI emitter and is user friendly in that the ion source doesn't need to be opened or modified in any way. The main benefit of dual-spray HDX reactions is that the acid quenching step of the continuous labelling and pulsed HDX methods can be surpassed. As noted by Konermann and co-workers, the process of desolvation in ESI acts as a quenching mechanism[20]. By dual-spray HDX, labelling of proteins occurs on microsecond to millisecond time scale, thus it is less time consuming than the continuous labelling method. The peptides of interest were oxytocin and Phe-Leu-Glu-Glu-Leu, which were used in proof of concept experiments. Ubiquitin, lysozyme, and cytochrome *c* are model proteins which were used to access the effectiveness of dual-spray HDX reactions for probing gas phase conformations of these species (Figure 1.2).

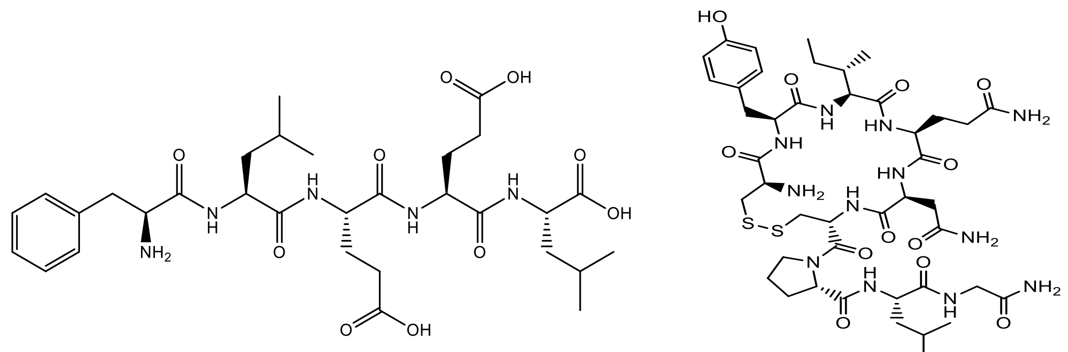

Phe-Leu-Glu-Glu-Leu
Exact Mass: 649.33

Oxytocin
Exact Mass: 1006.43

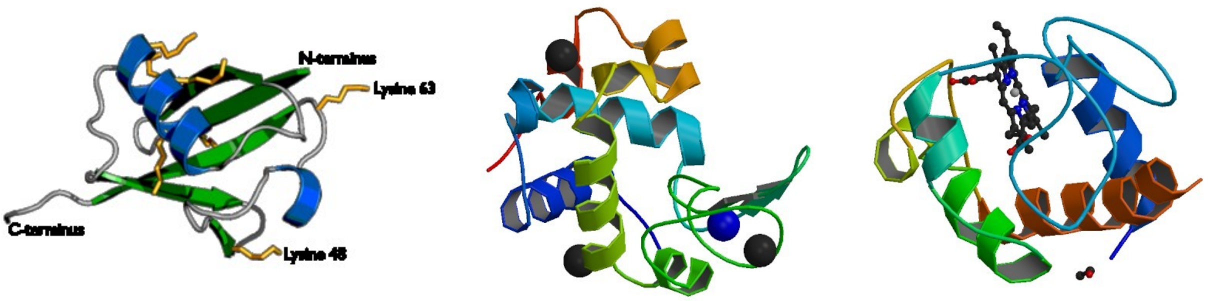

Ubiquitin (bovine)
Molecular Weight: 8564

Lysozyme (hen egg-white)
Molecular Weight: 14307

Cytochrome C (equine heart)
Molecular Weight: 12384

**Figure 1.2.** Peptides and protein molecules studied via the dual-spray HDX reactions. [21, 22]

## 1.4 Synthesis of transition metal-pyridyl complexes

The second reaction type explored was the dual-spray synthesis of transition metal-pyridyl complexes including $[Ru(bpy)_3]^{2+}$, $[Ru(phen)_3]^{2+}$, $[Fe(bpy)_3]^{2+}$, and $[Fe(phen)_3]^{2+}$ (bpy = 2,2'-bipyridine; phen = 1,10-phenanthroline) (Figure 1.3). Mixed ligand complexes of iron were also explored. Both bpy and phen are bidentate ligands which chelate to transition metals with higher affinity compared to single dentate ligands, which is explained by the chelate effect. The nitrogen atoms present on bpy and phen act as σ-donors by donating six pairs of electrons to the *d* orbitals of the transition metal. The transition metal accounts for the extra electron density by donating π-electron density to the ligand, which is known as π back-bonding[23]. This bonding generates an octahedral geometry for all the complexes shown in Figure 1.3. Metal-ligand charge transfer (MLCT) is responsible for the intense colour of these complexes. The $[Ru(bpy)_3]^{2+}$ complex is well known for its photocatalytic properties due to its ability to absorb light in the UV and visible spectrum[24]. Ferroin, which corresponds to the $[Fe(phen)_3]^{2+}$ complex, is widely used as a redox indicator[25].

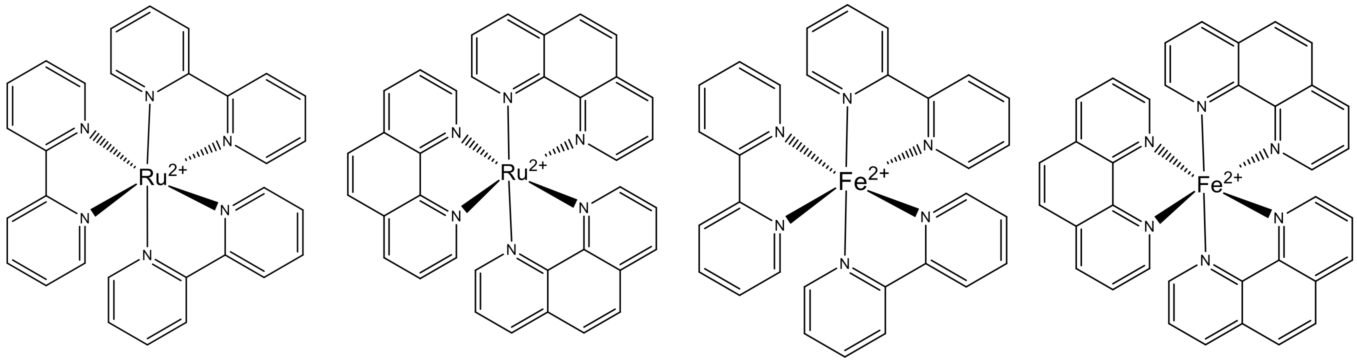

**Figure 1.3**. Transition metal-pyridyl complexes studied with dual-spray reactions.

The synthesis of metal-pyridyl complexes is particularly trivial, in most cases it involves mixing the pyridyl ligand in an aqueous solution of the transition metal. For example, $[Fe(phen)_3]^{2+}$ is generated by adding 1,10-phenanthroline to a solution of $FeSO_4$[25]. The simplicity of these reactions was taken into account when selecting a candidate for a dual-spray reaction. It provides an ideal opportunity to compare solution phase equilibrium to reactions within electrospray droplets. Also, the generation of unique gas phase species is possible using the dual-spray method. Comparing mass spectra, ion mobility arrival time distributions, and the CID fragmentation to reference standards allowed for characterization of complexes formed by each reaction.

# Chapter 2. Experimental Techniques

## 2.1 Electrospray Ionization MS

Electrospray ionization was first reported as an ionization technique for mass spectrometry by John B. Fenn in 1989[26], for which he was awarded the 2002 Nobel Prize in Chemistry. The discovery of ESI allowed for the analysis of fragile biological molecules such as proteins due its soft ionizing nature. Mass spectrometry analysis of biopolymers was not possible prior to the discovery of ESI because the ionization sources caused significant fragmentation during the formation of gas phase ions. ESI sources are atmospheric pressure ionization sources and they generate multiply charged ions, thus molecules which are several kDa in size such as proteins and nucleic acids can be analyzed[27]. Nanospray ionization is a variation of ESI which uses very low flow rates (20-50 nL/min) and a borosilicate glass capillary with a smaller internal diameter, which allows for lower sample consumption[28].

The analyte which is dissolved in a polar solvent enters the electrospray source through a stainless steel capillary which is surrounded by the nebulizing gas (typically nitrogen) which pneumatically assists the formation of a fine aerosol. A high potential (1.5-3.0 kV) is applied to the tip of the capillary compared to an adjacent counter-electrode which is the inlet of the mass spectrometer. Liquid emitted from the capillary forms a conical shape known as a Taylor cone[28]. Charged droplets are formed in the fine aerosol and the combination of desolvation gas and applied heat assists solvent evaporation from the droplets. In the formation of charged droplets, there are electrochemical reactions which can change the oxidation state of the analyte and/or the solvent; usually oxidations occur in positive mode and reductions occur in negative ion mode[29]. Following solvent evaporation, there exists a competition between the surface tension of the droplet and charge repulsion. Typically, if the charge repulsion is greater than the surface tension of the droplet, a coulombic fission event occurs at the droplet's Rayleigh limit[30]. Smaller highly charged droplets are ejected from the original charged droplet during this event. Figure 2.1 illustrates the process of ESI.

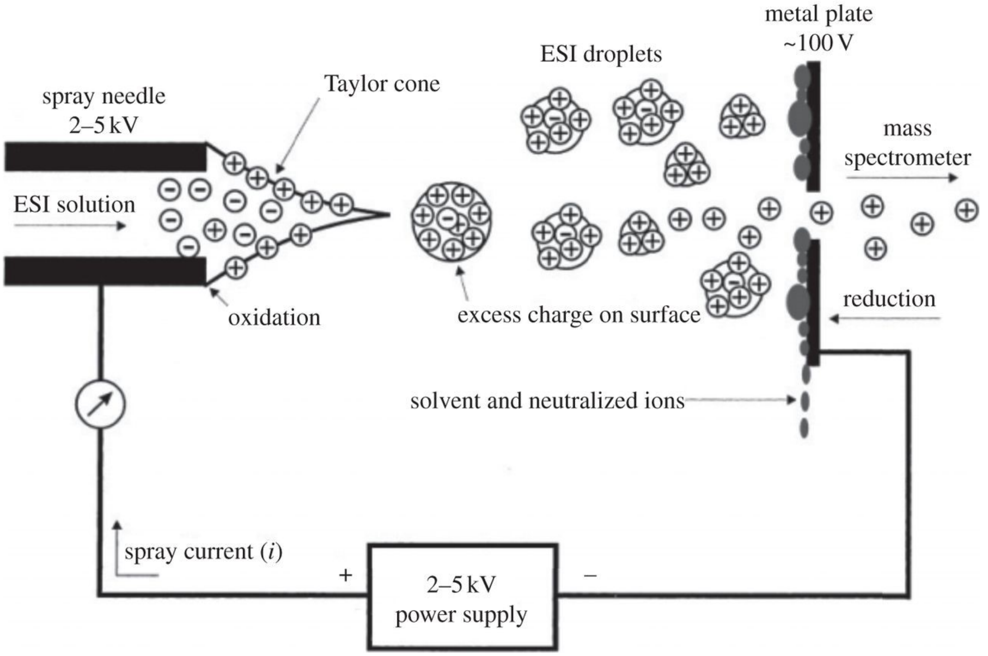

**Figure 2.1**. Overall process of analyte ion formation by ESI.[31] (Re-printed from Cech, N.B., Enke, C.G.: Mass Spectrometry Reviews. 20, 362-387 (2001) with the permission of John Wiley & Sons).

There exists several proposed mechanisms for analyte ion release from charged droplets. For small pre-charged analytes such as sodium ions, the ion evaporation model (IEM) is a proposed mechanism for ion release. This model suggests that the strong electric field generated by the droplet causes the ion to eject or evaporate from the charged droplet[32]. Molecular dynamics simulations of IEM indicate that the ion first causes surface protrusions from the charged droplets and this leads to ion ejection[33]. The charge residue model (CRM) explains gas phase ion formation for large globular analytes like natively folded proteins. CRM suggests that ion ejection from charged droplets for large globular analytes is unlikely. Instead, solvent evaporation to near dryness generates a charged droplet containing a single analyte molecule and this causes the remaining charges of the charged droplet to transfer to the analyte[34]. For disordered polymers, another mechanism known as the charge ejection model (CEM) is used to explain the ionization mechanism of these analytes. The CEM model explains that disordered polymers such as denatured proteins extend out of charged droplets as large protrusions and charges are transferred from the charged droplet to the analyte[35]. Currently, the proposed ionization mechanisms of ESI are the subject of considerable debate and actual analyte charging may be an intermediate regime between the proposed mechanisms. A visual representation of the IEM, CRM, and CEM are illustrated in Figure 2.2.

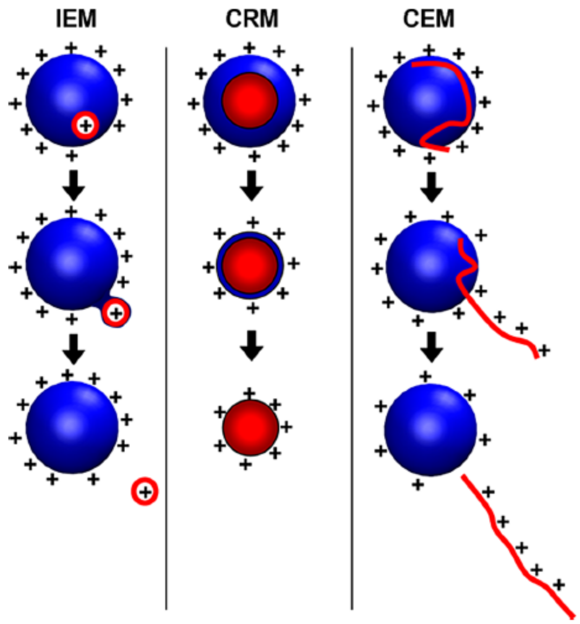

**Figure 2.2**. Visual representation of the IEM, CRM, CEM mechanisms of analyte charging.[36] (Re-printed with permission from Konermann, L., Ahadi, E., Rodriguez, A.D., Vahidi, S.:Analytical Chemistry. 85, 2-9. Copyright 2012 American Chemical Society.)

## 2.2 Mass Analyzers

After gas phase ions are generated by the ESI source, there are several electromagnetic ion guides (skimmer, focusing lenses, hexapoles) which channel the ions into the mass analyzer. All regions beyond the ESI source are differentially pumped to achieve vacuum ($10^{-3}$-$10^{-7}$ mbar). Extremely low pressures must be reached because gas phase ions readily react with air. The most widely used mass analyzers on ESI instruments include quadrupoles, ion traps, and time of flight (TOF) mass analyzers. A schematic diagram of the Synapt G1 used in this research is shown in Figure 2.3. A quadrupole and TOF mass analyzer are equipped on the Synapt G1. Another feature of the Synapt G1 is a travelling wave ion mobility drift tube which will be further discussed in the next section.

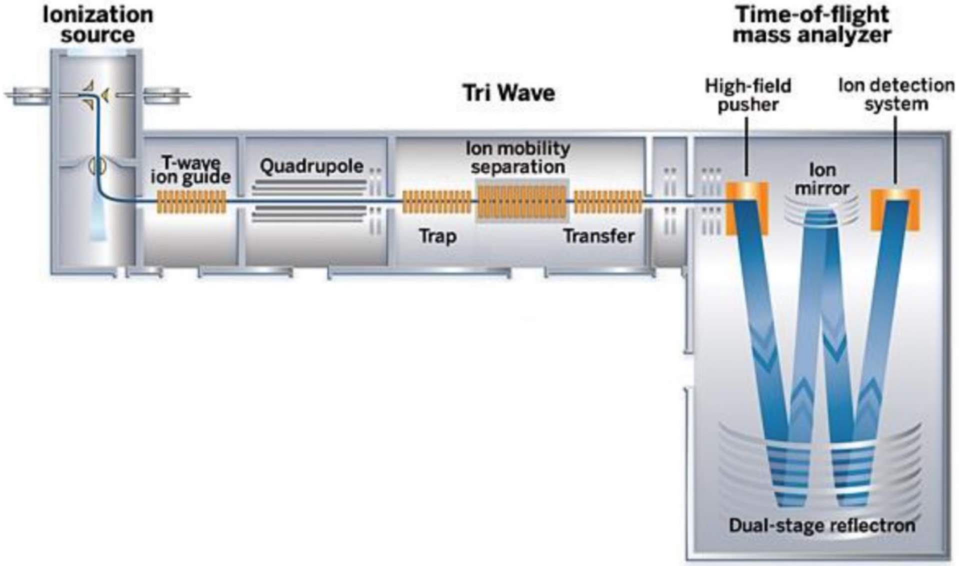

**Figure 2.3.** Schematic diagram of the Synapt G1 HDMS instrument.[37] (Reprinted from Jacoby, M.: Doubling up on Mass Analysis. Chemical and Engineering news. 88, 35-37 (2010)

The quadrupole in the Synapt G1 is used to mass select ions of interest to conduct collision induced dissociation (CID) experiments (trap or transfer cell) or to obtain ion mobility data for mass selected ions. Quadrupole mass filters consist of four parallel rods that have an applied DC and radio-frequency (RF) voltages[38]. Ions are accelerated into the quadrupole and a positively charged ion will be pulled towards a negatively charged rod but if the rod switches polarity (becomes positively charged) the ion will switch direction. Ions of a certain m/z will have a stable trajectory through the rods, while ions of different m/z will have an unstable trajectory and strike the rods. The stable trajectory will allow the transmission of mass selected ions.

Ions entering the TOF mass analyzer are accelerated by an electric field such that all ions (of the same charge $z$) have equivalent kinetic energy. This allows ions to be separated by their mass $m$ since the velocity of the ions $v$ is inversely proportional to the square root of the mass (KE= $\frac{1}{2}mv^2$). Since all the ions travel the same distance to the detector, the lighter ions will reach the detector before heavier ions[39]. The kinetic energy imposed by the electric field is described by the following equation:

$$\textbf{(5)} \quad \mathrm{KE} = zeV$$

Where $z$ is the charge of the ion, $e$ is the charge of an electron, and $V$ is the strength of the electric field. Thus a doubly charged ion will have double the amount of kinetic energy than a singly charged species. Ions are separated by their m/z ratio and this allows a mass spectrum to be generated. The Synapt G1 instrument utilizes a reflectron type TOF analyzer. The reflectron is an ion optic device which reflects the path of ions to account for differences in kinetic energy for ions of similar m/z[40]. Typically, reflectron type TOF analyzers have greater mass resolution than linear TOF analyzers however their sensitivity is lower. Mass resolution $R$ is defined by equation 6

$$\textbf{(6)} \quad R = \frac{m}{\Delta m}$$

where m is the mass of the peak in the mass spectrum and Δm is the peak width at a certain height, typically at 50% peak height[41]. The Synapt G1 can be used in “V” mode which uses a single reflectron or “W” mode which uses two reflectrons. The “V” mode has greater sensitivity but less resolution than “W” mode. A multichannel plate detector is equipped on the Synapt G1 for the detection of the ions and this detector consists of an array of electron multipliers which initiate a cascade of electrons when it is struck with an ion.

## 2.3 Travelling Wave Ion mobility

Ion mobility spectrometry (IMS) is an analytical method to separate gas phase ions based on their mobility through a buffer gas in the presence of an electric field[42]. IMS is often coupled to mass spectrometry and this technique is known as ion mobility-mass spectrometry (IM-MS). The separation of gas phase ions relies on the fact that larger ions experience more collisions with the neutral buffer gas than smaller ions thus the larger ions will take longer travel across the IMS cell[43]. Ions are thus separated by their collision cross sections (Ω). Also, ions of higher charge states will traverse the drift tube at a higher rate due to greater separation field strength. Ions exiting the IMS cell are sampled by the mass analyzer to generate mass spectra of the separated ions. Collision cross-sections can be calculated using the equation 7:

$$\textbf{(7)} \qquad \Omega = \frac{(18\pi)^{1/2}}{16} \frac{ze}{(k_b T)^{1/2}} \left[\frac{1}{m_I} + \frac{1}{m_N}\right]^{1/2} \frac{t_D E}{L} \frac{760}{P} \frac{T}{273.2} \frac{1}{N}$$

where z is the charge of the ion, e is the elementary charge in Coulombs, $k_b$ is the Boltzmann constant, T is the temperature in Kelvin, $m_I$ is the mass of the ion, $m_N$ is the mass of the neutral gas, $t_D$ is the drift time in seconds, E is the electric field strength, L is the length of the drift tube, and N is the neutral gas number density ($m^{-3}$)[44].

The Synapt G1 instrument uses a variation of IMS known as travelling wave ion mobility spectrometry (TWIMS) which applies a non-uniform electric field. The ion mobility cell in a TWIMS instrument has an arrangement of ring electrodes which are supported by circuit boards which provide RF and DC voltages. A high electric field (DC voltage) is applied to a section of the IMS cell and is sequentially applied to the ring electrodes in the direction of drifting ions[43]. This consecutive application of DC voltage creates a travelling wave which propels the ions through the IMS cell. A visual representation of TWIMS is shown in Figure 2.4.

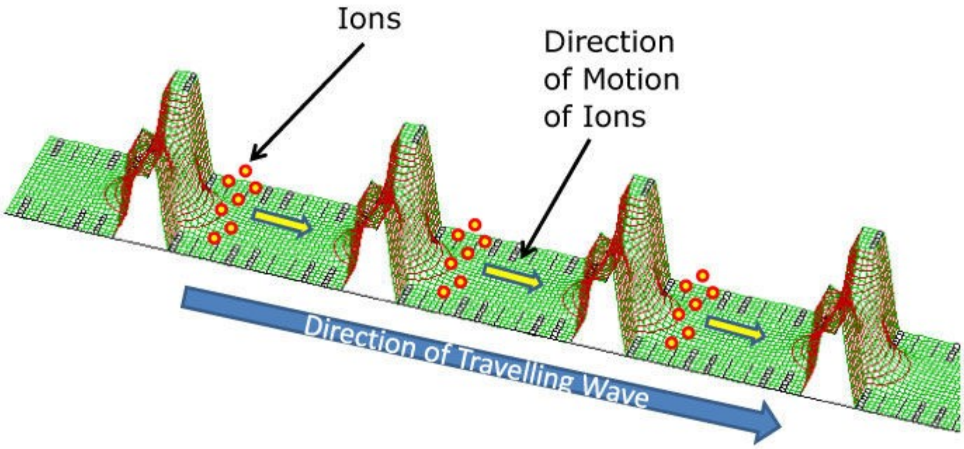

**Figure 2.4**. Visual representation of travelling-wave ion mobility (TWIMS).[45] (Reprinted from Waters: Travelling wave (T-wave).

For travelling wave ion mobility, the collision cross section cannot be calculated directly because of the non-uniform time dependent electric fields[46]. Instead, accurate cross section determinations are done using calibrants with known collision cross sections. For this research, ion mobility was used as a tool to compare drift time distributions and as a method to separate isobaric species, thus collision cross section calculations were not required.

## 2.4 Collision Induced dissociation (CID)

Tandem mass spectrometry (MS/MS) is a technique in mass spectrometry which involves two or more stages of mass analysis and is routinely used as a tool for structural elucidation[47]. Examples of tandem mass spectrometry include collision induced dissociation (CID)[48], photon-induced dissociation[49], and electron capture dissociation (ECD)[50]. By analyzing the products of these fragmentation reactions, structural elucidation is possible. In the case of the Synapt instrument, after gas phase ions are generated by the ESI source, they can be mass selected using the quadrupole mass filter and subsequently collided with an inert collision gas ($N_2$, He, Ar) within the trap or transfer collision cell. For this research, all CID experiments were done in the transfer cell (Figure 2.3). In-source CID can be done on the Synapt by increasing the cone voltage parameter which is a voltage setting between the sampling cone and skimmer cone. An increase in cone voltage accelerates the ions and causes collisional activation by collision with the desolvation gas or residual solvent molecules[51].

For CID, the collision of the mass selected ion and the neutral target gas causes the kinetic energy of the precursor ion to be converted into internal energy and this energy is redistributed within the vibrational degrees of freedom of the ion. The vibrationally excited ion can then undergo unimolecular fragmentation reactions, producing fragment ions that are later detected by the mass analyzer[48]. The fraction of kinetic energy that is converted into internal energy is indicated by the centre of mass collision energy ($E_{com}$) which is described by the following equation:

$$\textbf{(7)}\quad E_{com} = \frac{m}{m+M} E_K$$

where m is the mass of the collision gas, M is the mass of the precursor ion, and $E_k$ is the kinetic energy of the precursor ion[48]. There are two different collision regimes used in CID, low energy CID ($E_{com}$ 1-100 eV) and high energy CID ($E_{com} > 100$ eV)[52]. CID data is often presented as a "breakdown curve" which plots the precursor and fragment ion relative intensities as a function of $E_{com}$.

The different unimolecular dissociations pathways that a molecule can experience are known as ***dissociation channels***[51]. The rate constant for unimolecular dissociation *k* is dependent on the internal energy content *E* of the molecule. As *E* increases, the rate constant *k* for the dissociation increases which is observed from *k(E)* curves presented in Figure 2.5. The relationship between *k* and *E* is modelled by the Rice–Ramsperger–Kassel–Marcus (RRKM) theory[53, 54]. The RRKM equation which relates the energy *E* to the rate constant *k* is

$$\textbf{(8)}\quad k(E) = \frac{\sigma\, N^{\ddagger}(E-E_0)}{h\, \rho(E)}$$

where $N^{\ddagger}(E-E_0)$ is the transition state sum of states, σ is the reaction degeneracy, h is Planck's constant, and ρ(E) is the density of states of the parent ion. The dissociation channels of a molecule can be competing reactions and generate different *k(E)* curves (Figure 2.5).

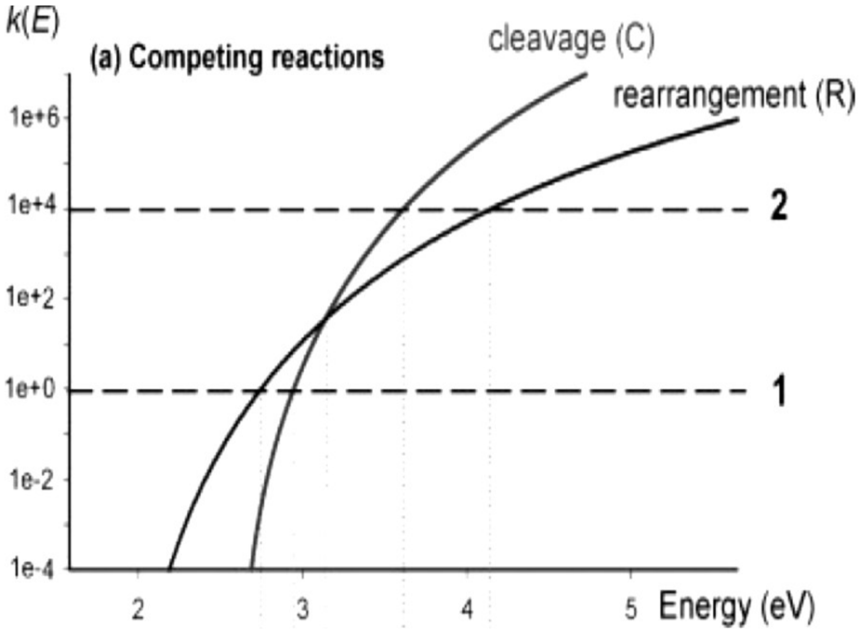

**Figure 2.5**. *k*(E) curves for two competing unimolecular reactions, rearrangement and cleavage. [51] (Reprinted from Gabelica, V., Pauw, E.D.: Mass Spectrometry Reviews. 24, 566-587 (2005) with the permission of John Wiley & Sons)

## 2.5 Mass spectrometry of peptides and proteins

Analysis of peptides and proteins by mass spectrometry requires a soft ionization source such as ESI or MALDI (Matrix Assisted Laser Desorption Ionization) in order for intact molecular ions to be observed in the mass spectrum. Formation of multiply charged species, especially by ESI, allows proteins which are several kDa to MDa in mass to fall in the m/z range of typical mass analyzers[26]. Pairing of chromatographic methods like HPLC to ESI-MS has allowed the analysis of complex biological samples such as protein mixtures[55]. In addition to providing molecular weight information of a protein, ESI-MS is also used as a tool to investigate a protein's structure[56], its amino acid sequence[57], post-translational modifications[58], and non-covalent interactions[59],[60].

When an intact protein sample is electrosprayed, many peaks are observed in the mass spectrum which correspond to the charge state distribution (CSD) of the protein. In positive mode, multiple basic amino acid residues accept protons from solvent molecules to become positively charged. Proton abstraction from acidic residues is responsible for charging in negative mode. Factors affecting the CSD of a protein include presence of denaturants, solution pH, the number of acidic/basic residues in the protein, protein surface area, and the presence of non-volatile salts[61]. Typically, the ESI mass spectra of proteins under native conditions show a narrow CSD which centers around the number of surface exposed acidic/basic residues. Native proteins transferred to the gas phase by ESI retain their tightly folded tertiary structure thus only the acidic/basic residues exposed to the solvent on the surface of the protein will become charged[62]. The crystal structure of the protein often indicates the number of acidic/basic residues present on the outer surface. Denaturing proteins using pH extremes or chemical denaturants causes unfolding of the native protein structure which increases the surface area of the protein and exposes more acidic/basic residues to the solvent. This allows more protons to be retrieved/abstracted and thus the CSD shifts to higher charge states. Figure 2.6 shows the shift in charge state distribution for β2-microglobulin when it is exposed to denaturing conditions (low pH). It has been widely accepted that the charge state distribution in positive mode. ESI probes the tertiary structure of proteins[63]. However, the ESI process may change the conformation of proteins dramatically from their original structure found in the bulk solution[64]. Thus the CSD in the mass spectrum reflects the three-dimensional structure of the protein within the charged droplet and not in the bulk solution.

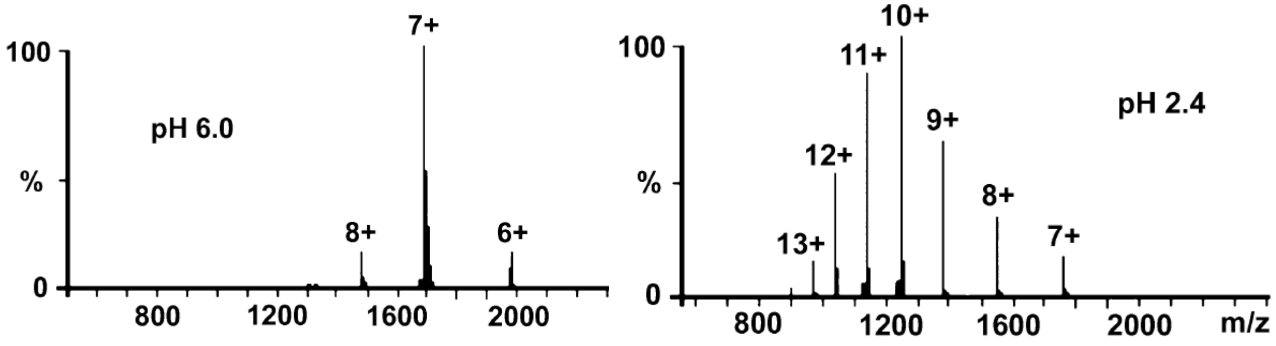

**Figure 2.6.** ESI-MS spectra of β2-microglobulin under native conditions (pH 6.0) and denaturing conditions (pH 2.4) which shows a shift in the charge state distribution.[65] (Reprinted from Ashcroft, A.E.: Natural Product Reports. 22, 452-464 (2005) with the permission of Royal Society of Chemistry)

Protein sequencing is very important when investigating protein structure and function in proteomics research. Sequencing within an ESI-MS instrument is usually accomplished using collision induced dissociation (CID) or electron capture dissociation (ECD). During the CID process, the protons involved in charging of the peptide can migrate to amide nitrogen atoms, a process described by the mobile proton model[66]. This migration is thought to eliminate the resonance stabilization of the amide bond, thus making the backbone amide bonds weaker. For peptides, low energy CID causes fragmentation of backbone amides, which generates “direct sequence ions” useful for sequencing purposes. N-terminal fragment ions include $a_n$, $b_n$, and $c_n$ ions while the C-terminal fragment ions include $x_n$, $y_n$, and $z_n$ ions (where n = # of amino acid residues)[67]. There exists two distinct approaches for sequencing a protein, which include “top-down” and “bottom-up” proteomics. “Top-down” proteomics involves electrospraying an intact protein then CID is used for sequencing[68] whereas for the “bottom-up” proteomics approach, proteolytic enzymes are used to digest the protein and the resulting peptides are sequenced by

CID[69]. The subsequent use of databases allows for identification of unknown proteins within a sample.

## 2.6 ESI-MS of organometallic complexes

Electrospray ionization (ESI) is among the most versatile techniques for the characterization of organometallic complexes. Theoretically, any ionic complex or neutral complex which is chemically derived to a related ion may be studied using ESI-MS. Ionic complexes in solution are easily detected due to the soft ionizing nature of ESI. Among the first complexes to be studied by ESI-MS were the dications $[Ru(bipy)_3]^{2+}$ and $[Ru(phen)_3]^{2+}$ (bipy = 2,2'-bipyridine ; phen = 1,10-phenanthroline), which are observed intact at relatively low values of cone voltage[70]. ESI-MS is often used for the detection of intermediates in organometallic reactions[71],[72]. However, it is important to note that the electrochemical reactions which occur during the electrospray process may change the oxidation states of organometallic species. Non-covalent interactions between biological macromolecules and metal ions have been studied extensively by electrospray ionization MS[59],[60].

## 2.7 Computational Chemistry

Computational chemistry methods are often used to calculate molecular geometries, spectra, and properties of molecules. This is often the case when trying to understand the electronic structure of a stationary point such as a transition state or an energy minima of a reaction. One of the most important assumptions in computational chemistry is the Born-

Oppenheimer approximation, which states that the nuclei in a molecule are essentially stationary relative to electrons[73]. This assumption is essential because it allows molecular geometry to be understood. For this dissertation, computational methods such as density functional theory are used to identify possible structures of a novel coordination complex which is formed by dual-spray reactions.

The potential energy surface (PES) is an important concept in computational chemistry. The PES is a graphical representation of a molecules' energy as a function of its geometry. Stationary points such as energy minima and transition states (saddle points) are the most important features of the PES and correspond to points where $dE/dq = 0$, where E is energy and q is a geometric parameter[73]. Figure 2.7 illustrates a three dimensional PES. The process for geometry optimization starts with an initial geometry guess then the geometry of the molecule is altered to find the stationary point. A vibrational frequency calculation is needed to determine the nature of the stationary point. All vibrations for minima are real while transition states have one imaginary vibration which corresponds to the reaction coordinate. The vibrational frequency calculations also predict the IR spectrum for the molecule and calculates the zero-point energy[73].

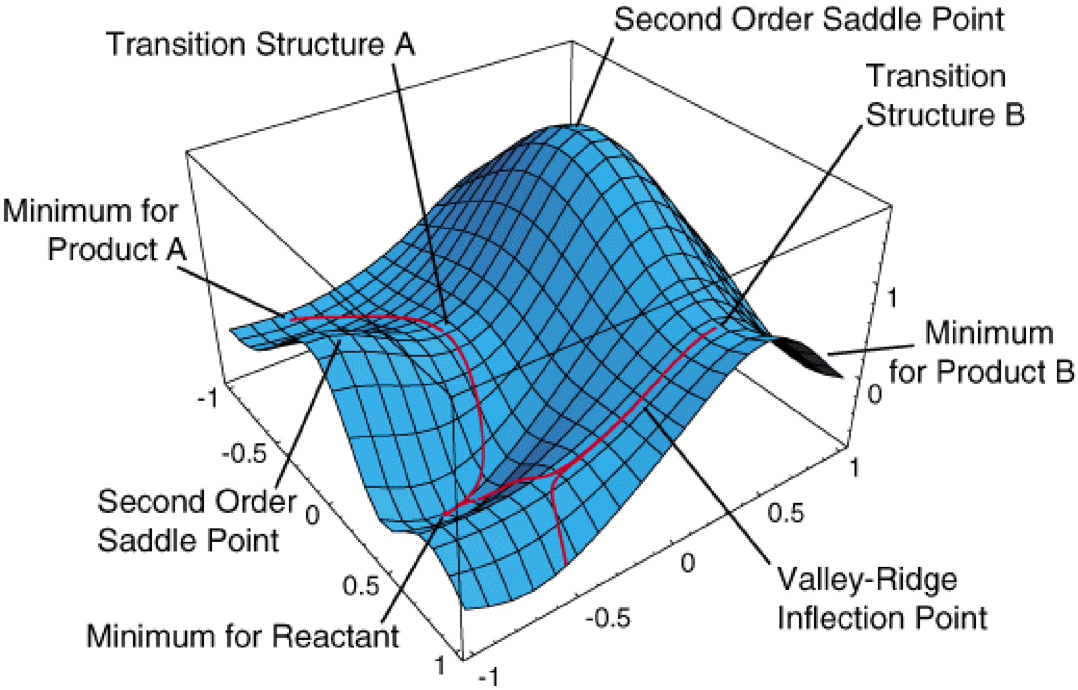

**Figure 2.7.** Three dimensional potential energy surface (PES). Important features of the PES are labelled. [74]

Density functional theory (DFT) is a quantum mechanical method which calculates the electronic structure and properties of molecules. The fundamental theory of DFT describes that the energy of a system is related to the electron density instead of the many-electron wavefunction. DFT is based on the Hohenberg-Kohn theorems[75] and it became more practical when the Kohn-Sham equations were formulated which accounted for exchange and correlation interactions[76]. The ground state energy when using the many-electron wavefunction is dependent on 3N (N = # of electrons) while for DFT, the ground state electron density is dependent on three spatial coordinates. DFT methods are therefore faster than traditional wavefunction based methods and more practical for large molecules since it is less computationally expensive[73]. There also exists hybrid functionals such as B3LYP (Becke, 3-

parameter) which approximate the exchange correlation functional using Hartree-Fock theory. The popular computational chemistry software package, Gaussian, is used for computational chemistry calculations. A DFT calculation for a geometry optimization follows an iterative process, which is shown in Figure 2.8. The process involves an initial guess of the electron density $\rho(\mathbf{r})$. The effective potential $v_{eff}(\mathbf{r})$ is calculated for this electron density followed by solving the Kohn-Sham equations using the eigenvalue $\varepsilon_i$ and the Kohn-Sham orbital $\psi_i$. The electron density $\rho(\mathbf{r})$ and total energy is then re-evaluated using the Kohn-Sham orbital $\psi_{i.}$ The next step involves checking various convergence criterion. If the convergence criteria is not met, the calculation restarts with a new electron density and this follows and iterative process until the convergence criteria is met.

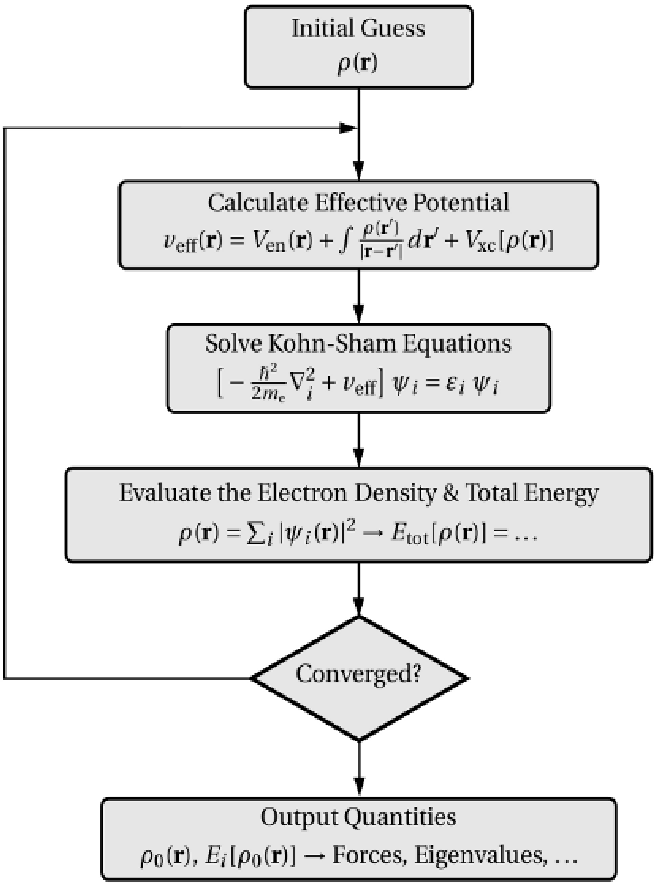

**Figure 2.8**. Iterative scheme for Density Functional Theory (DFT). [76]

# Chapter 3. Procedures

## 3.1 Dual-spray HDX Reactions

Oxytocin, Phe-Leu-Glu-Glu-Leu, ubiquitin, lysozyme, and cytochrome *c* were purchased from Sigma Aldrich. Oxytocin and Phe-Leu-Glu-Glu-Leu were dissolved in 50:50 methanol, water (HPLC grade purchased from Fisher Scientific) at millimolar concentrations. Native ubiquitin and lysozyme solutions were made by dissolving the lyophilized powder in 95:5 water, acetic acid. The solvent used for denatured ubiquitin was 50:45:5 $H_2O$, MeOH, $CH_3COOH$. Denatured lysozyme samples were prepared by first reducing its disulfide bonds with dithiothreitol (DTT) using the procedure described previously[78] then diluting the resulting mixture to millimolar concentration with 95:5 water, acetic acid. Native cytochrome *c* solution was made using 3% MeOH in $H_2O$ with 1 mM of ammonium formate. Unfolded cytochrome *c* was generated by acidifying the solution with formic acid to pH 3.0.

All experiments were carried out on Waters Synapt G1 ion mobility mass spectrometer. Solutions of peptides and proteins were electrosprayed in positive mode at flow rates of 10-15 μL/min and ESI parameters such as capillary voltage (2.5-3.5 kV) and cone voltages (20-30 V) were adjusted to maximize ion counts. The source gas flow was set to 22 mL/min for all samples. For dual-spray HDX reactions not requiring ion mobility separation, three minute signal acquisitions were obtained. At the one minute mark of electrospraying the peptide or protein solution, the secondary syringe pump containing $D_2O$ was turned on at a flow rate of 20 μL/min and allowed to electrospray for two minutes. For species requiring ion mobility separation (oxytocin), the resolving quadrupole was set to the appropriate mass and the HM and LM resolution was lowered to increase the window of masses that are observed. Separate data was acquired with the $D_2O$ emitter turned on and the $D_2O$ emitter turned off for oxytocin. Data analysis for short peptides was done through spreadsheets containing deconvolution functions, allowing the yield calculation of the various dual-spray HDX products while taking into account the natural isotope distribution of the species. For ubiquitin, lysozyme, and cytochrome *c*, the average number of exchanges was calculated by taking the difference in mass before and after $D_2O$ is introduced into the ion source via the secondary ESI emitter.

## 3.2 HPLC coupled to dual-spray HDX reactions

HPLC separation of proteins and subsequent dual-spray reaction was achieved using the Waters 2690 Alliance HPLC System coupled to a Waters Q-TOF Ultima global mass spectrometer, which has two independent ESI emitters. The Hypersil GOLD C8 column was used for separating an equimolar mixture of unfolded cytochrome *c* and native lysozyme. The mobile phases included 0.1% TFA in $H_2O$ (mobile phase A) and 0.1% TFA in 75:25 $CH_3CN$, $H_2O$ (mobile phase B). The gradient used was 10%-100% B in 40 min and the flow rate was set to 0.1 mL/min. For the dual-spray reaction, the same conditions were used while having the second ESI emitter electrospraying $D_2O$ at a flow rate of 10 μL/min.

## 3.3 Probing the mechanism of dual-spray HDX reactions

To better understand the mechanism of dual-spray HDX reactions, the relative geometry of the ESI emitters were adjusted. A single ESI probe was raised using various sizes of washers which increased the distance between the interacting microdroplets. The average number of exchanges were then calculated to determine any difference in deuterium uptake.

## 3.4 Dual-spray synthesis of transition-metal pyridyl complexes

Dual-spray synthesis of transition metal complexes was achieved using a Synapt G1 mass spectrometer which is equipped with a dual electrospray ionization (ESI) source. Formation of metal-pyridyl complexes was accomplished by spraying solutions of a metal salt through one ESI emitter and a ligand solution through the secondary emitter. $[Ru(bpy)_3]^{2+}$ and $[Ru(phen)_3]^{2+}$ reference standards (purchased from Sigma Aldrich) were first analyzed and parameters were optimized to maximize ion counts for the unfragmented complexes; for the $[Ru(phen)_3]^{2+}$ complex this required a capillary voltage of 3.2 kV and a cone voltage of -52 V. The mass spectra, ion mobility arrival time distributions, and CID fragmentation at various $E_{com}$ values (for generation of breakdown curves) were acquired. The dual-spray reaction was run with similar parameters while electrospraying $RuCl_3$ in MeOH ($10^{-3}$ M) and a ligand solution of bpy or phen in MeOH ($10^{-4}$ M). Since ruthenium has a total of seven stable isotopes, the mass spectrum becomes extremely complex. Therefore, the resolving quadrupole of the instrument is used to mass select the $[Ru(bpy)_3]^{2+}$ and $[Ru(phen)_3]^{2+}$ complexes and filter the other ions generated by electrospray. Comparing the spectral features of the dual-spray products to the reference standards allowed for characterization of complexes formed by the reaction. Similar methods were used for the dual-spray formation of iron-pyridyl complexes and mixed ligand iron (II) complexes. Breakdown curves were generated by normalizing ion intensities for all collision energies.

## 3.5 Computations

Density functional theory (DFT) calculations were used to optimize the geometry and calculate vibrational frequencies of $[FePhen_3]^{2+}$, the dual-spray product $[FePhen_3 + 2H]^{2+}$, and the fragment ions which are generated by CID. Initially, the semi-empirical method PM6 was used to get the preliminary guess of the geometry. These preliminary geometries were then used as input structures for DFT calculations. For all DFT calculations, Becke's three-parameter hybrid functional with Lee, Yang, and Parr's correlation functional (B3LYP) was used. The basis set used for was the Los Alamos effective core potential plus double-ζ basis set (LANL2DZ) and all calculations were completed using the Gaussian 09 program.

# Chapter 4. Dual-spray HDX Reactions

## 4.1 Dual-spray HDX of short peptides

Due to the novelty of the dual-spray process, we first performed proof-of-concept experiments on short peptides. The first dual-spray HDX reaction was attempted on the relatively small peptide Phe-Leu-Glu-Glu-Leu. When this peptide is electrosprayed, the dominant ion is the singly charged protonated species $[M + H]^+$. The isotopic distribution for the $[M + H]^+$ species changes dramatically when $D_2O$ is introduced into the ion source through the secondary ESI emitter. The distribution of peaks shifts to higher m/z ratio indicating deuterium exchanging with hydrogen within the ion source. The signal (total ion counts) observed in the total ion chromatogram decreases by 30% when $D_2O$ is allowed through the secondary ESI emitter. The drop in signal is likely due to lower sampling efficiency when the ESI droplets from the adjacent emitters interact. The mass spectrum comparing the $[M + H]^+$ after introduction of $D_2O$ and percentages of the products are indicated in Figure 4.1. The peptide Phe-Leu-Glu-Glu-Leu, has a total of nine exchangeable hydrogens. The two major products of the reaction correspond to two

(D2) and three (D3) deuterium exchanges and represent 32% and 25% of the products respectively.

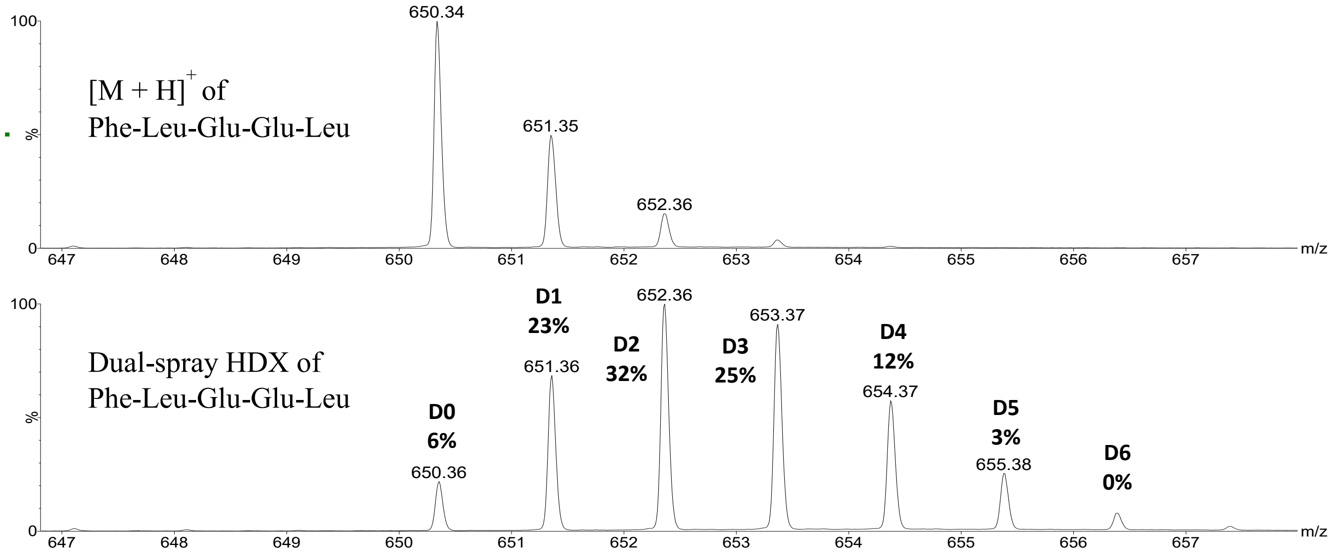

**Figure 4.1.** ESI mass spectrum of the protonated $[M + H]^+$ species of the Phe-Leu-Glu-Glu-Leu peptide (top panel) and dual-spray HDX reaction with $D_2O$ (bottom panel). Also shown is the percentages of products formed in the reaction.

Deuteration sites cannot be confirmed using the Synapt G1 since it does not support electron capture dissociation (ECD) reactions and traditional CID experiments produce unwanted scrambling[79]. The most likely sites of deuteration are on the glutamic acid residues and the C and N termini. The initial $[M + H]^+$ represents 6% of the product distribution which indicates that the HDX reaction does not fully convert $[M + H]^+$ to deuterated products. Back-exchange may also occur, however the time-scale of dual-spray HDX reactions are on the order of milliseconds and it is essentially too short for this to be a major factor. Desolvation temperature and pH of the peptide solution were altered to determine if these factors had an effect on the product distribution. Very minor deviations in the product distribution were observed when these variables were adjusted. The products resulting from two and three deuterium exchanges remained the major products of the HDX reaction. One reason for the consistent product distribution is the fact that the Phe-Leu-Glu-Glu-Leu peptide lacks secondary and tertiary structure and is essentially always in an unfolded state regardless of pH and desolvation temperature.

The second peptide that was reacted via dual-spray HDX was oxytocin. The ESI mass spectrum indicates that the most dominant ions are $[M + H]^+$ and $[M + Na]^+$. For the purposes of the dual-spray HDX reaction, we were interested in the $[M + H]^+$ ion. In addition to the $[M + H]^+$ ion, an isobaric species overlaps in the same region of the mass spectrum. This isobaric species corresponds to the doubly charged oxytocin dimer, $[2M + 2H]^{2+}$. By ion mobility, it is possible to separate these species and carry out the HDX reaction simultaneously on both species. With optimized ion mobility parameters, the oxytocin monomer has a drift time of 3.53 ms while the oxytocin dimer has drift time of 2.51 ms (Figure S1, Appendix). Since the dimer is doubly charged, its mobility is greater through the IMS cell than the singly charged monomer because of a greater separation field strength. The ESI mass spectra following dual-spray HDX reaction for the oxytocin monomer and dimer are shown in Figure 4.2 and 4.3 respectively. The major products of the oxytocin monomer HDX are the initial $[M + H]^+$ ion and the singly deuterated species (D1) which account for 48% and 28% of the products. There are 16 exchangeable hydrogens for the oxytocin monomer. Since the structure of oxytocin contains a disulfide bond which forms a ring, the amide hydrogens may not be easily accessible to the solvent $D_2O$ for exchange reactions. Also, oxytocin does not contain any acidic amino acid residues which have more labile hydrogens and are most likely to exchange with deuterium. The most probable sites of H/D exchange are the hydroxyl group of the tyrosine residue and the terminal amide residues.

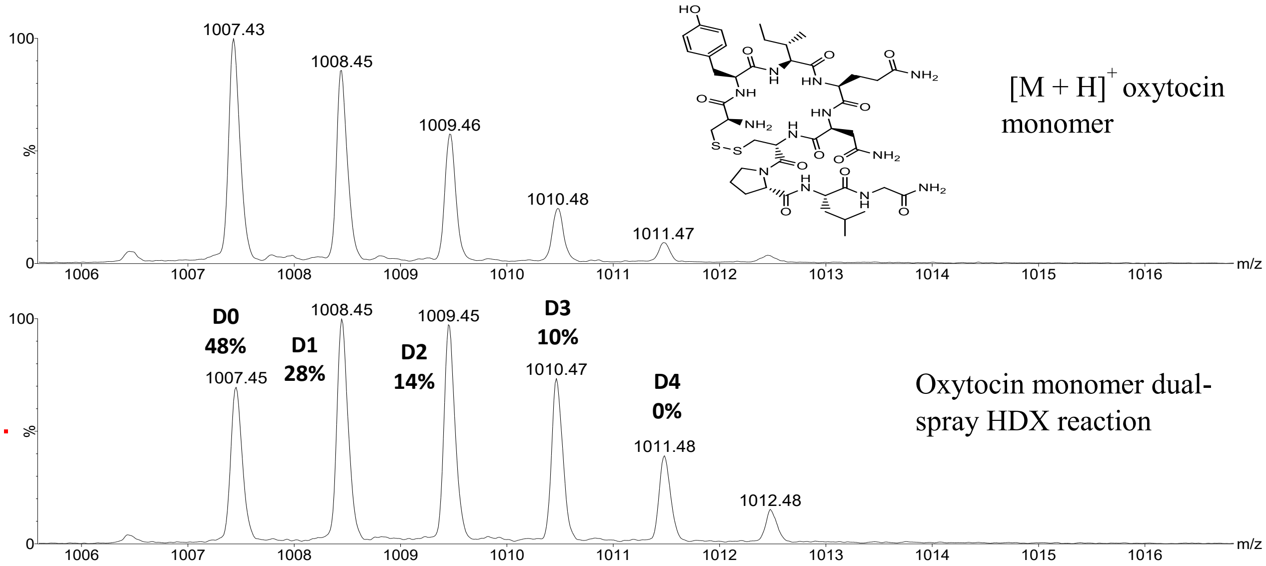

**Figure 4.2.** ESI mass spectrum of dual-spray HDX reaction of the oxytocin monomer and $D_2O$. The top panel indicates the isotopic distribution of oxytocin $[M + H]^+$ species and the oxytocin structure. The bottom panel is the mass spectrum following the dual-spray HDX reaction. The product percentages are also shown.

As expected, the oxytocin dimer experiences more deuterium exchanges which is indicated by the lower percentage of the initial $[2M + 2H]^{2+}$ ion relative to the oxytocin monomer $[M + H]^{+}$ (Figure 4.2). The dimer has up to five deuterium exchanges while the monomer has a maximum of three exchanges. Since the oxytocin dimer has double the number of exchangeable hydrogens, it is reasonable to expect greater deuterium uptake on the dimer.

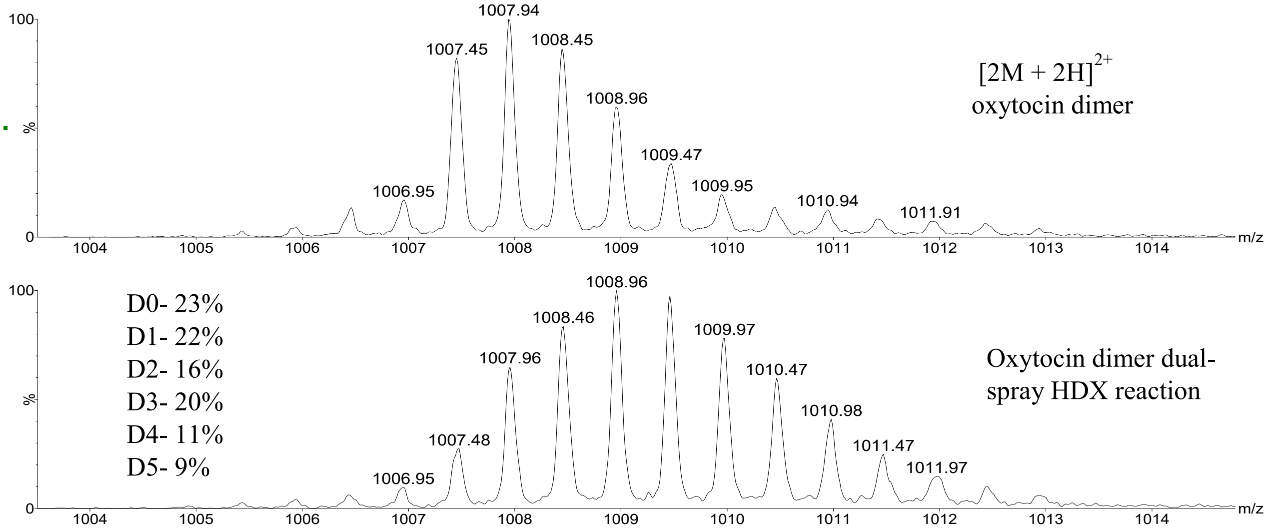

**Figure 4.3.** ESI mass spectrum of the oxytocin dimer $[2M + 2H]^{2+}$ (top panel) and the mass spectrum following the dual-spray HDX reaction (bottom panel). The product percentages are also shown.

This is also observed when the percentages of non-deuterated products are compared (monomer = 48%, dimer = 23%). These results also indicate that it is possible to conduct HDX reactions on two distinct species simultaneously within the same dual-spray HDX experiment.

## 4.2 Dual-spray HDX of Proteins

Ubiquitin was the third candidate for the dual-spray HDX reaction. This protein is present in many charge states, as seen in the ESI mass spectrum. Depending on which solvents are used, some charge states are favoured over others[80]. Figure 4.4 shows the ESI mass spectrum of ubiquitin in 95:5 $H_2O$, $CH_3COOH$ solvent and the dual-spray HDX reaction. The charge state distribution observed is consistent with the crystal structure of ubiquitin which has 6 to 8 basic amino acid residues that are exposed to the solvent[80]. It has been widely accepted that the charge state distribution in positive mode ESI probes the tertiary structure of proteins [63]. When methanol is absent from the solution (95:5 $H_2O$, $CH_3COOH$) the charge states of 7+, 8+, and 6+ are favoured since the protein has a tightly folded conformation (known as the "N" or native state). The N state consists of a tightly hydrogen-bonded structure which consists of α-helices, a $3_{10}$ helix, a mixed β-sheet containing five strands, and seven reverse turns [81]. A bimodal distribution with higher charge states can be observed in native conditions if the concentration of ubiquitin is high, however the 7+, 8+, and 6+ ions remain the dominant ions of the population.

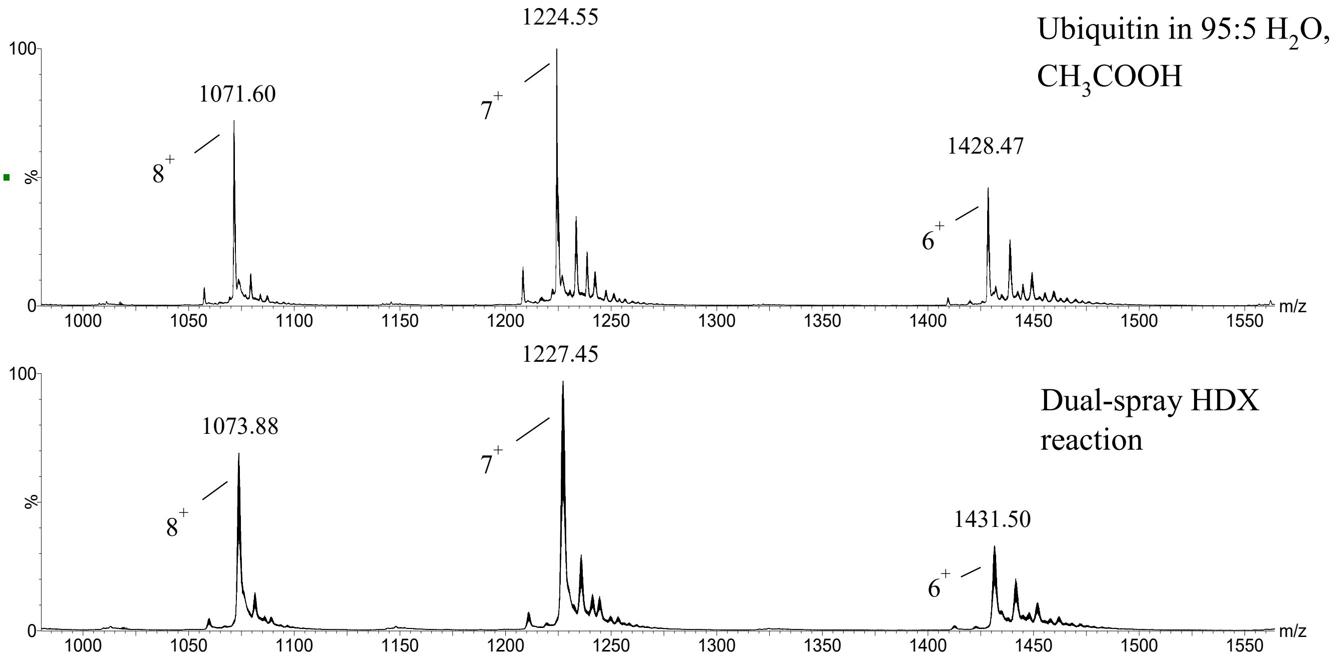

**Figure 4.4**. ESI mass spectra of ubiquitin in 95:5 $H_2O$, $CH_3COOH$ (top panel) and with dual-spray HDX (bottom panel) showing the shift in isotopic distributions. The charge states of the ions are also shown.

There is a clear shift of the entire isotope pattern for all of the charged states of native ubiquitin when the secondary ESI emitter charged with $D_2O$ is turned on (Figure 4.4). The average number of exchanges is between 18 and 20 exchanges for all the charge states of native ubiquitin. These exchange values are very similar and indicate that the species of these charge states have very similar conformations. When compared to solution phase HDX results published by Katta and co-workers[80], the number of exchanges is much less for the dual-spray HDX reaction (89 exchanges vs 19 exchanges). The time scale for the dual-spray is on the order of milliseconds while the solution phase reactions were done for 20 min, thus it is reasonable to observe much greater exchange for the solution phase HDX reactions.

Higher charge states such as 9+, 10+, 11+, 12+, and 13+ are favoured when methanol is added in the ubiquitin solution (50:45:5 $H_2O$, MeOH, $CH_3COOH$). Methanol is a denaturing agent which induces protein unfolding and ubiquitin is stabilized in the partially unfolded "A" state[82]. Based on NMR experiments, it was found that the C-terminal half, which in the N state is rich in β-strand character, experiences a methanol-induced transition to an elongated structure with more α-helical character[83]. Since ubiquitin is in a partially unfolded "A" state, a greater number of basic sites are available for protonation. With the solvent 50:45:5 $H_2O$, MeOH, $CH_3COOH$ the charge state distribution becomes much broader compared to the "N" state and the most abundant charge state is 10+ (Figure S2, Appendix). After $D_2O$ is introduced, the entire isotope distribution for all of the charge states shifts to higher mass to charge ratio. By dual-spray HDX, it was found that that the average number of exchanges for denatured ubiquitin is similar to native ubiquitin (between 18 and 20 average exchanges). However, the 12+ and 13+ charge states, which are more abundant in solutions containing methanol, have lower average exchanges (15.12 ± 0.5 and 12.09 ± 0.5 average exchanges respectively). This was also observed by Kostyukevich and co-workers with their in-source HDX reactions with ubiquitin and based on the ECD reactions that they performed, the charge states of 12+ and 13+ contain segments that restrict the access of the deuteration agent[5]. It is evident that both ambient vapors and ESI droplets formed from a secondary ESI emitter behave similarly; they penetrate into ESI droplets and change the solvent composition. The exchange data for native and denatured ubiquitin is presented in Table S1 in the Appendix.

For the range of desolvation temperature tested (100-300˚C) it was found that the desolvation temperature has no effect on the average number of exchanges. This observation is contrary to the findings of Kostyukevich and co-workers; they observed that the desolvation temperature is directly proportional to the number of exchanges[5]. The ESI source used by Kostyukevich and co-workers contains a desolvation capillary while the Synapt G1 used in our study does not contain a desolvation capillary. The overall dynamics for desolvation is different between the two instruments and this in turn affects the average deuterium uptake observed at various temperatures. The desolvation temperature also did not affect the product distribution for the HDX reaction of Phe-Leu-Glu-Glu-Leu; thus in the case of the Synapt G1 this instrumental parameter does not affect the products formed in dual-spray HDX reactions. In-source unfolding of ubiquitin was attempted by electrospraying the native ubiquitin solution (95:5 $H_2O$, $CH_3COOH$) through the primary emitter and methanol through the secondary emitter. The charge state distribution did not shift dramatically to higher charge states as expected; the greatest increase was for the 11+ charge state which changed by 1.7%.

The structure of lysozyme consists of a β sheet and several α-helices which are stabilized by four intramolecular disulfide bonds[84]. The positive ESI mass spectrum of native lysozyme shows several charge states, the most abundant being the 9+, 8+, and 10+ charge states (Figure S3, Appendix). Ion mobility measurements indicate that these charge states are dominated by highly folded and partially unfolded conformations in the gas phase[85]. Cleaving the disulfide bonds of lysozyme via DTT reduction causes the protein to unfold which is clearly indicated by the shift of the charge state distribution to higher charge states, 15+ being the most abundant (Figure 4.5). As with ubiquitin, more basic sites become available to protonation when the protein is denatured. By dual-spray HDX, native lysozyme and denatured lysozyme have a proportional increase in the average number exchanges as the charge state increases (Figure 4.6).

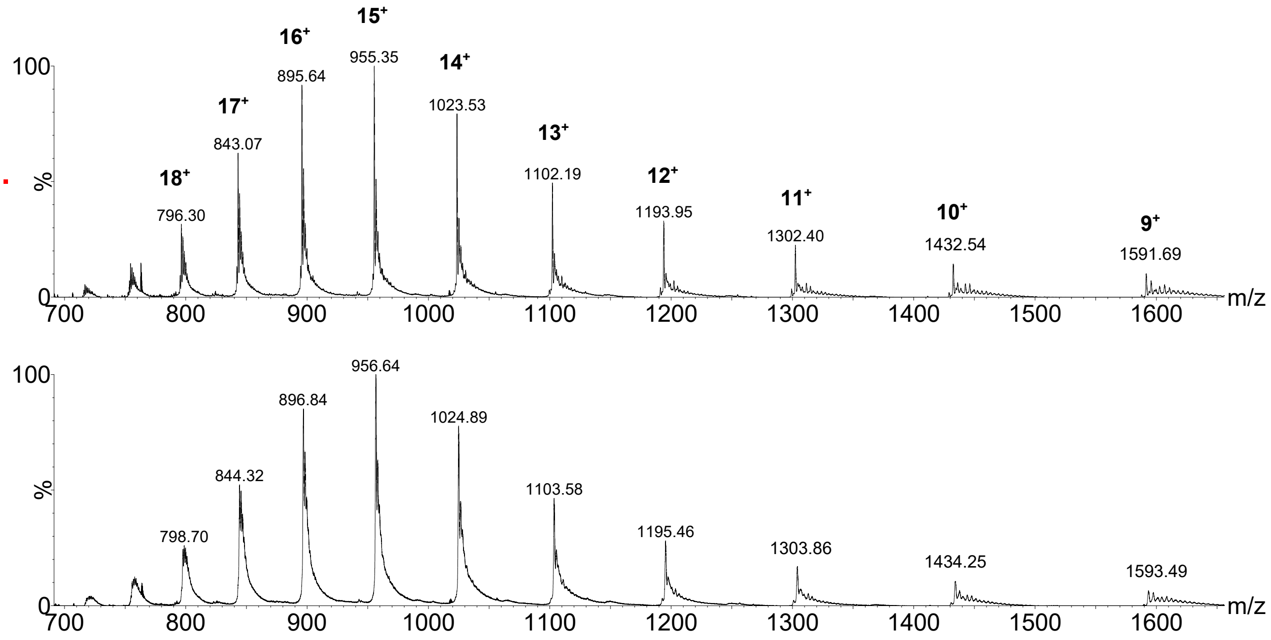

**Figure 4.5**. ESI mass spectrum of DTT reduced lysozyme (top panel) and the corresponding dual-spray HDX reaction (bottom panel).

Lysozyme becomes increasingly unfolded as the charge state increases which makes the exchangeable hydrogens of lysozyme more accessible to the deuterating agent $D_2O$. Thus it is reasonable to expect a direct correlation between the charge state and the average number of exchanges. The increased level of H/D exchange may also be caused by a greater number of protons on the higher charge states. The 18+ and 19+ charge states have a large increase in deuterium uptake (23.2 ± 0.5) relative to the 17+ charge state, likely due to loss of secondary structure at these charge states. Exchange data for both forms of lysozyme is available in Table S2 in the Appendix.

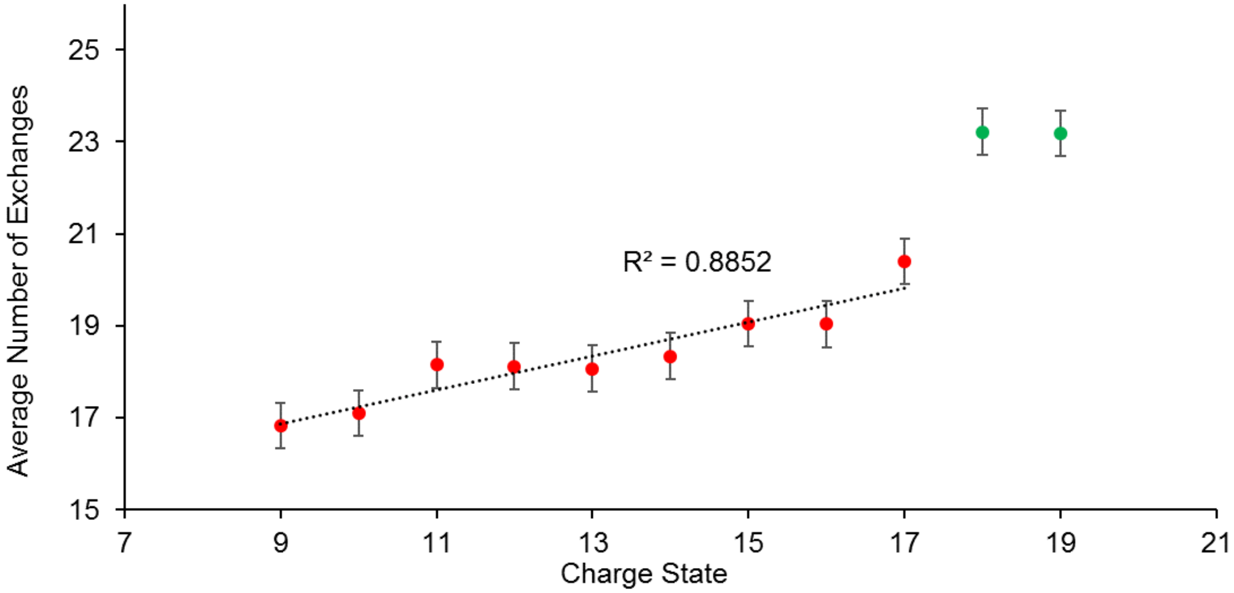

**Figure 4.6.** Average number of hydrogen/deuterium exchanges for the observed charge states of DTT reduced lysozyme. The 18+ and 19+ are not included in trend line due to likely loss of secondary structure.

The ESI mass spectrum of a native cytochrome *c* solution (pH = 5.5) indicates a narrow distribution of charge states centered around the 7+ charge state (Figure 4.7). Cytochrome *c* is composed of several α-helices and β-Turns which are folded into a globular shape[86]. The structure also contains a heme group which has a centrally coordinated iron atom and is responsible for electron transfer between complexes of the electron transport chain[87]. For the native cytochrome c solution, there is 34.2 ± 0.5 average exchanges for the charge states 6+, 7+, and 8+ by dual-spray HDX. Similar degree of deuterium uptake for these charge states indicate analogous gas phase confirmations. When the solution is acidified (pH= 3.0) the charge state distribution shifts to higher charge states, indicating that the cytochrome *c* structure is sensitive to low pH conditions and causes unfolding of the native structure of cytochrome *c*. The ESI mass spectrum of denatured cytochrome *c* is shown in Figure S4 in the Appendix along with the corresponding dual-spray HDX reaction. At pH 3.0, the charge state distribution shifts to higher charge states, however the 6+, 7+, and 8+ charge states are still present in the mass spectrum (bimodal distribution) at lower intensity and have less exchanges (29.8 ± 0.5 exchanges) compared to the native cytochrome *c* solution, indicating that lower pH decreases the rate of deuterium exchange as in solution phase[17]. For denatured cytochrome *c* the CSD centers around the 14+ charge state which is the most abundant in the mass spectrum. Similarly to the dual-

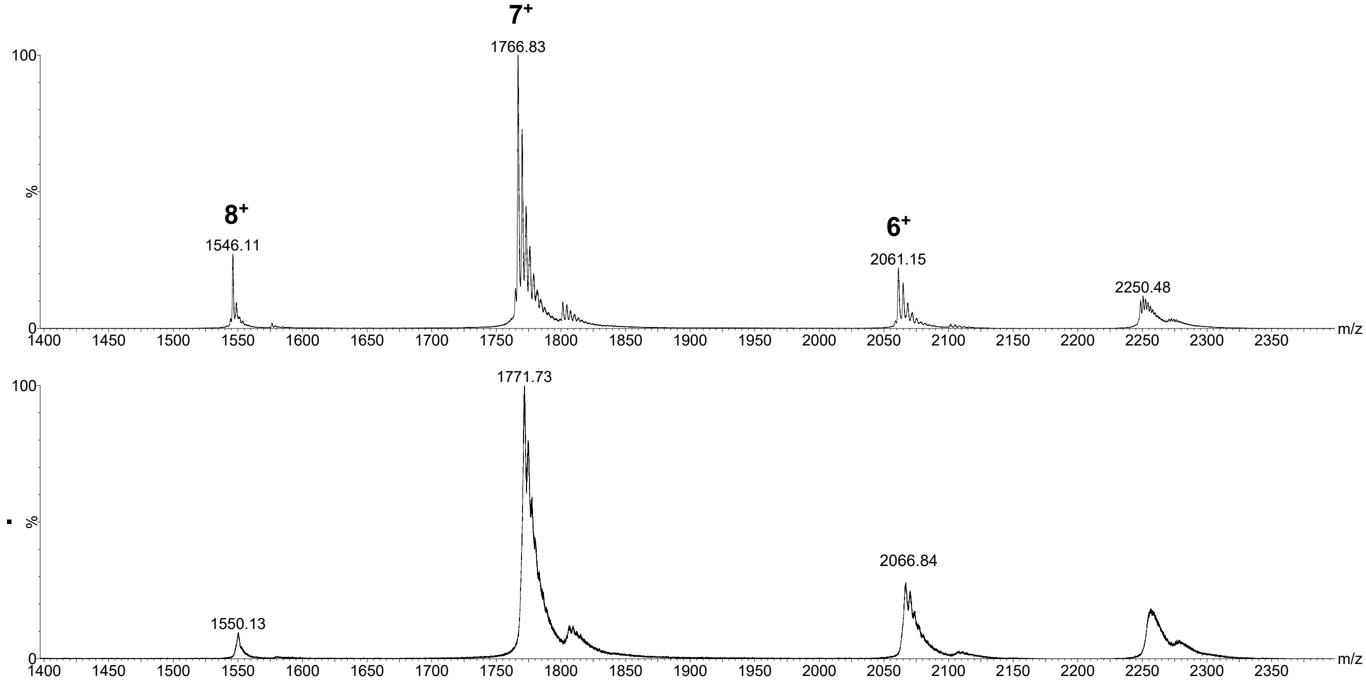

**Figure 4.7.** ESI charge state distribution of native cytochrome *c* in 3% MeOH in $H_2O$, 1 mM ammonium formate (top panel). Dual-spray HDX reaction of native cytochrome *c* showing shift in mass for all charge states (bottom panel).

spray HDX reaction with lysozyme, the average number of exchanges increases as the charge state increases for the 9+ to 15+ charge states. The cytochrome *c* structure becomes increasingly unfolded as the charge state increases, and acidifying a solution containing 3% methanol has been shown to lead to the loss of secondary structure [63]. However, the average number of exchanges decreases for charge states greater than 15+ (Figure 4.8). This result demonstrates that the gas phase conformation of cytochrome *c* may have segments of the structure which restricts access for the deuterating agent at charge states higher than 15+. Similar results were obtained by gas-phase HDX studies, which demonstrated that the gas phase conformations of the 16+ and 17+ charge states have lower deuterium uptake compared to the 15+ charge state of cytochrome *c*[88], and it is suggested that these charge states of cytochrome *c* form a more compact "A state" similar to low pH conditions in solution phase[89]. Figure 4.8 indicates the average number of

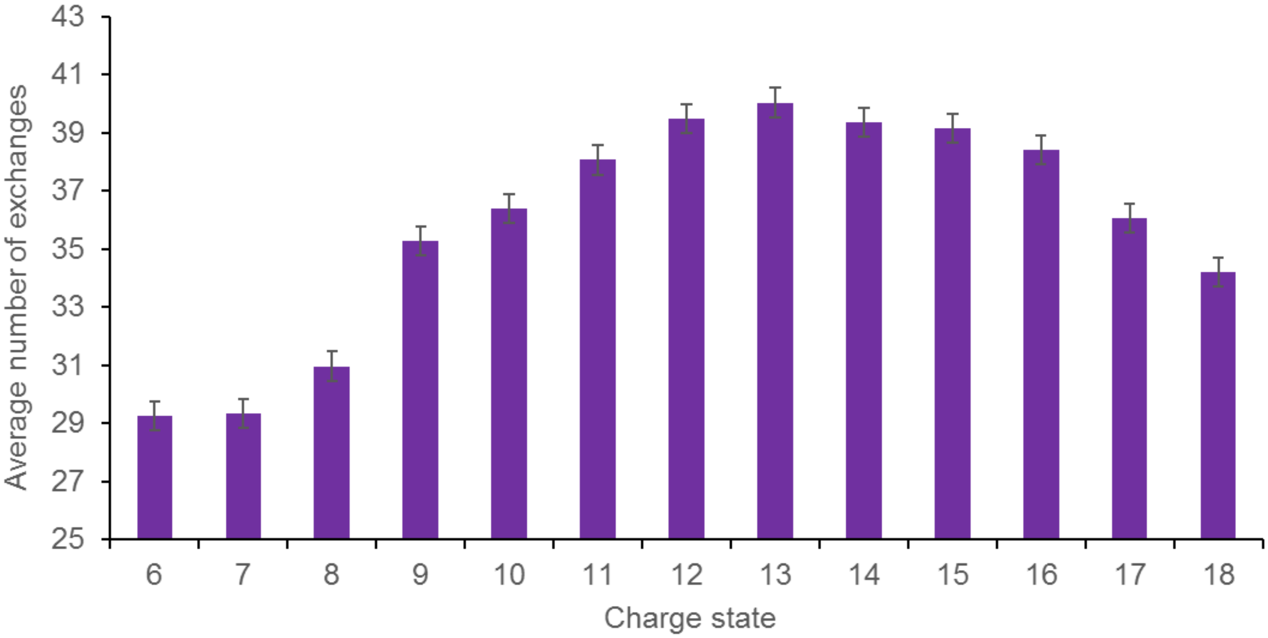

**Figure 4.8.** Average deuterium exchanges for the various charge states of cytochrome *c* in its denatured form (pH 3.0).

exchanges observed for the charge states of denatured cytochrome *c*.

To further demonstrate the applicability of the dual-spray HDX method, we wanted to pair the method with on-line reverse phase HPLC to analyze mixtures of proteins. The mixture of denatured cytochrome *c* and native lysozyme was used for this purpose. Using the conditions mentioned earlier, the chromatogram in Figure 4.9 was obtained. The peak at retention time 33.38 min corresponds to cytochrome *c* while the peaks at the retention time of 35.35 min and 35.93 min both correspond to lysozyme, which was confirmed by examining the mass spectra. The mass spectrum of lysozyme shows lower charge states (5+, 6+, and 7+) compared to the direct injection of native lysozyme and these charge states show extensive signal suppression due to formation of gas-phase ion pairs with TFA[90]. Signal suppression by TFA can be resolved by using post-column addition of propionic acid and 2-propanol (75:25, v/v) which has been shown to displace TFA[91]. A similar chromatogram was obtained while simultaneously electrospraying

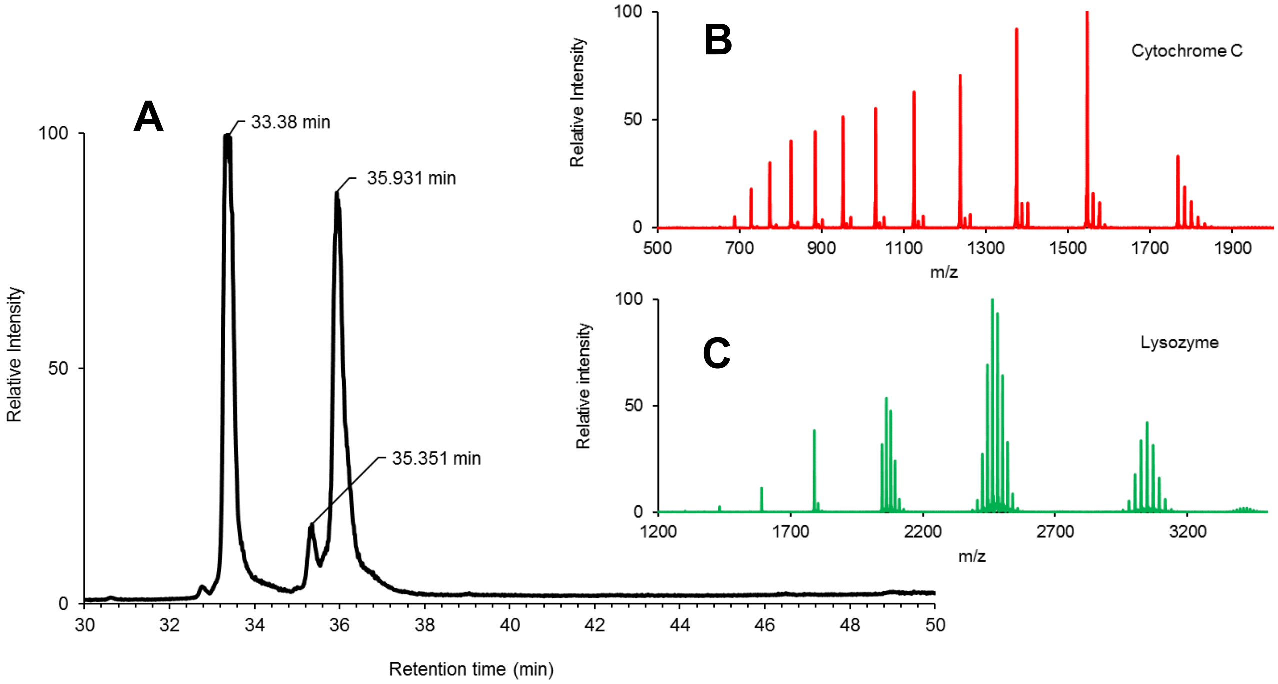

**Figure 4.9.** (**A**) HPLC-MS chromatogram of equimolar native lysozyme + denatured cytochrome c solution. (**B**) Mass spectrum obtained for retention time 33.38 min, which corresponds to denatured cytochrome *c*. (**C**) Mass spectrum obtained for retention time 35.35 min and 35.93 min, corresponding to native lysozyme.

$D_2O$ through the secondary ESI emitter, thereby showing the coupling of the two methods. The mass spectra of cytochrome *c* and lysozyme shows all charge states shifted to higher m/z ratios, indicating hydrogen/deuterium exchange within the ion source.

The average number of exchanges for cytochrome c and lysozyme by using the paired HPLC method follow similar trends to directly injecting the solutions via syringe pump. The gas phase conformations of two different proteins within a mixture can therefore be investigated using this paired method. The values for average deuterium exchanges is dramatically lower when using the HPLC-MS paired method. For example, the 8+ charge state of cytochrome *c* has 30.9 ± 0.5 average deuterium exchanges by directly injecting the solution by syringe pump while there is 7.04 ± 0.5 average exchanges by the HPLC paired HDX method (Figure 4.10). The flow rate of solution is 10 fold greater for the HPLC method (100 µL/min) than the direct injection method (10 µL/min) and this likely decreases the residence time of the proteins in the ion source. Also the concentration of the protein is lower with HPLC due to dilution by the mobile phase, which may ultimately reduce the deuterium uptake.

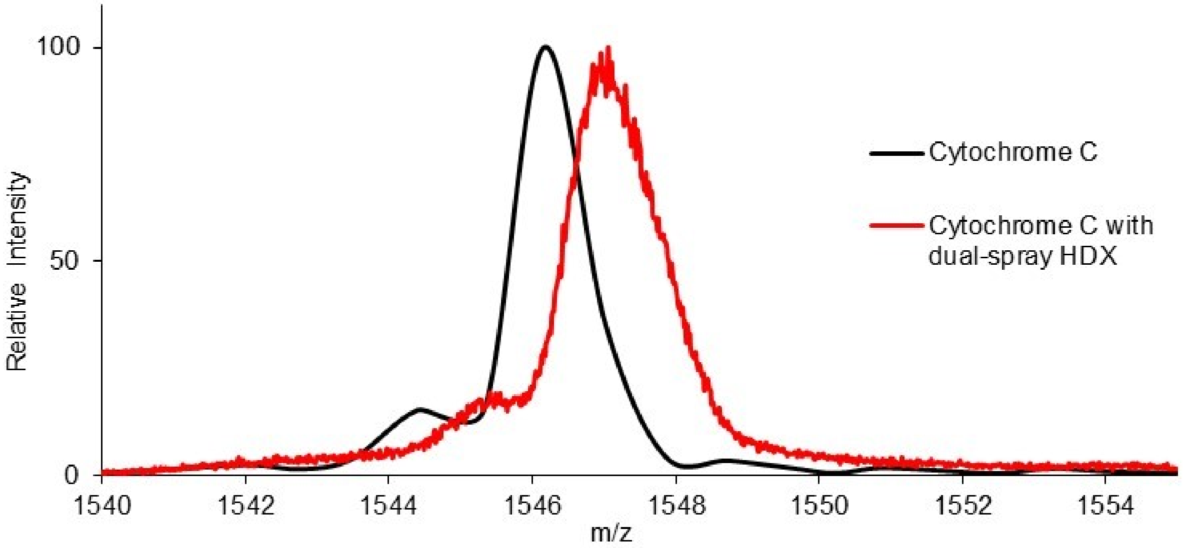

**Figure 4.10.** Observed shift in mass of the 8+ charge state of cytochrome *c* after HPLC-MS and subsequent dual-spray HDX. The data shown in black indicates the isotopic envelope of the 8+ charge state of cytochrome *c* after HPLC-MS while the red data shows the HPLC-MS of the 8+ charge state when paired to dual-spray HDX. The shift in the peak corresponds to 7.04 ± 0.5 average deuterium exchanges.

From our experiments it was unclear if the reactions occurred in solution after the fusing of microdroplets or in the gas phase involving desolvated peptide ions and $D_2O$ vapors. However, the study done by Kostyukevich and co-workers on gas-phase HDX showed a temperature dependence for the deuterium uptake by ubiquitin gas-phase ions[5], while the current dual-spray reactions did not show a temperature dependence. This suggests a gas phase process for the dual-spray reactions. However, the synthesis of organometallic species within the ESI source using the dual-spray reaction verifies that solution-phase reactions can occur in the dual-spray experiment. Since both ESI emitters have a positive polarity, Coulombic repulsion may cause repulsion of the charged droplets. However, the kinetic energy of the droplets is likely sufficient to cause mixing of microdroplets. Gas phase HDX reactions of fully desolvated analyte ions and deuteration agents may be occurring simultaneously as reactions within fusing microdroplets, thus the actual mechanism may be an intermediate regime between the two processes.

A more in-depth study was needed to determine the mechanistic details of deuterium exchange via the dual-spray reaction. Changing the relative position of the ESI emitters allows the mechanism to be understood since the extent of desolvation of the droplet is greater if the distance between the two emitters is increased. The protein analyte is more likely to be in the gas phase if the distance between the emitter and MS inlet is increased, thus a gas phase HDX reaction can be probed. A denatured cytochrome *c* solution (pH 3.0) was sprayed at increased distances from the MS inlet while the emitter for the deuteration agent $D_2O$ remained fixed. It was found that the deuterium uptake by denatured cytochrome c was consistent regardless of the distance of the ESI emitter. The initial position of the ESI emitter is the optimal distance from the MS inlet and an increase in distance showed a lower signal intensity in the mass spectra generated, likely due to lower sampling efficiency in the ESI source. The consistent deuterium uptake of cytochrome c at increased distances provides evidence that hydrogen/deuterium exchange reactions can occur in the gas phase within the ESI source (Figure 4.11). Exchange via fusing microdroplets and gas phase HDX reactions are perhaps occurring concurrently on a millisecond time scale.

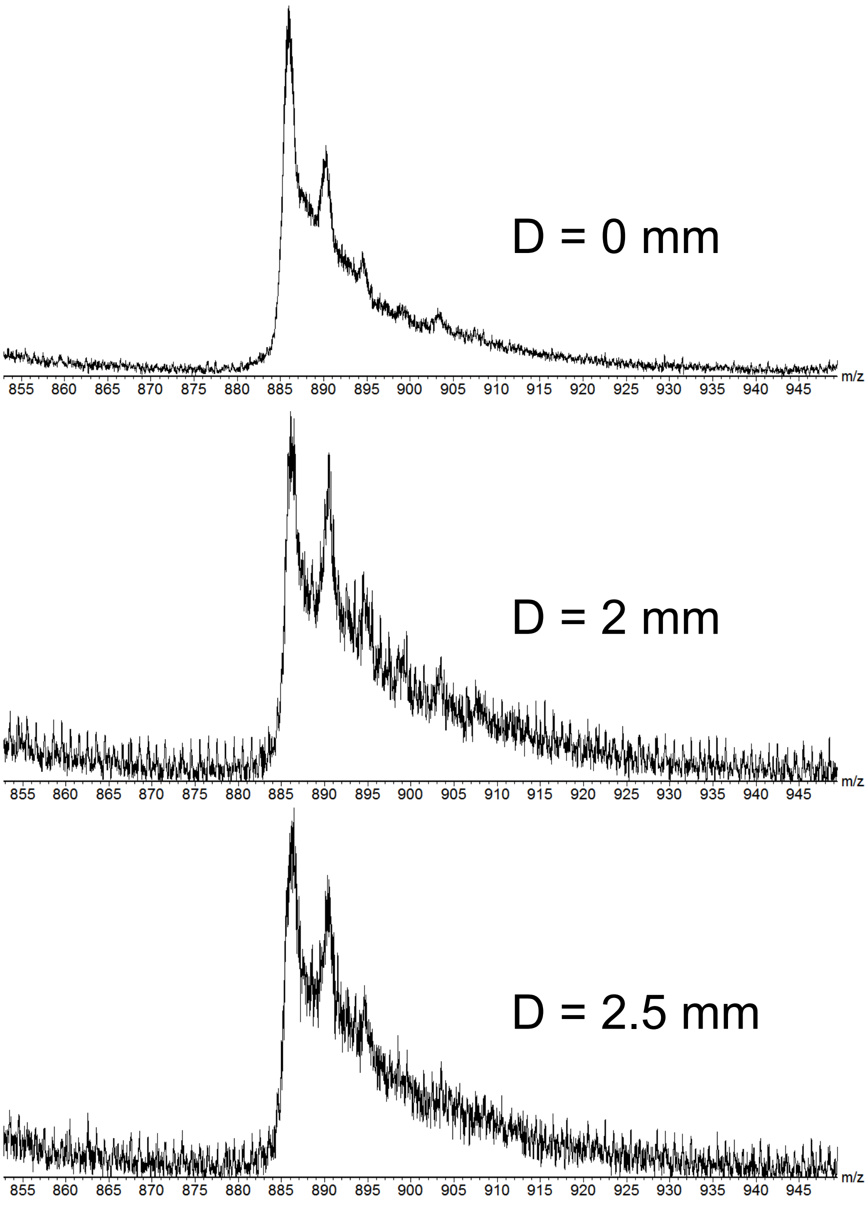

**Figure 4.11**. Dual-spray HDX reactions of the 14+ charge state of cytochrome c at various distances (D) from the secondary ESI emitter.

# Chapter 5. Dual-spray synthesis of organometallics

## 5.1 Dual-spray formation of transition metal-pyridyl complexes

The first complexes that were chosen for dual-spray synthesis reactions were the $[Ru(bpy)_3]^{2+}$ and $[Ru(phen)_3]^{2+}$ (bpy = 2,2'-bipyridine; phen = 1,10-phenanthroline) complexes. Analysis of reference standards of these complexes allowed for optimization of ESI parameters. These optimal parameters benefit the formation of complexes by the dual-spray reaction. The most important parameter is the cone voltage which can cause unwanted fragmentation of the complex at high voltages. Comparing ion mobility drift time, mass spectra, and CID fragmentation of reference standards to dual-spray products confirms the formation of $[Ru(bpy)_3]^{2+}$ and $[Ru(phen)_3]^{2+}$. The optimized parameters for all complexes are listed in Table S4 in the Appendix. By electrospraying a ligand solution containing bpy or phen through one emitter and a solution of $RuCl_3$ through the secondary ESI emitter, complexes of the type $[RuL_3]^{2+}$ and $[RuL_2]^{2+}$ are formed. Figure 5.1 shows the comparison of mass spectra of the $[Ru(bpy)_3]^{2+}$ reference standard and dual-spray product. The mass spectrum for the dual-spray reaction contains the major peaks of the isotopic distribution centered on m/z 285, which is the most abundant ion of the isotopic distribution. The resolving quadrupole is likely filtering out the remaining peaks of the isotopic distribution. The ion mobility chromatograms of the $[Ru(bpy)_3]^{2+}$ standard and the dual-spray product indicate a similar arrival time distribution (Figure 5.1), thus the dual-spray product has a similar structure to the octahedral complex $[Ru(bpy)_3]^{2+}$. These results indicate that $[Ru(bpy)_3]^{2+}$ was indeed formed by the dual-spray reaction. Similar spectral results were obtained for the $[Ru(phen)_3]^{2+}$ complex indicating the dual-spray formation of this complex (Figure S5, Appendix).

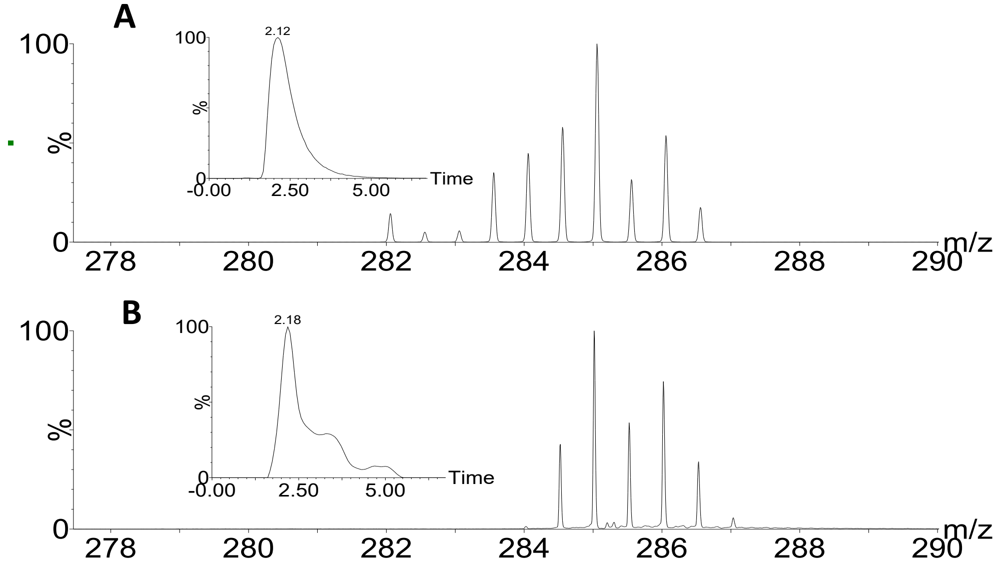

**Figure 5.1.** (**A**) Mass spectrum of $[Ru(bpy)_3]^{2+}$ reference standard indicating the isotopic distribution for the complex, the inset shows the ion mobility drift time distribution for the $[Ru(bpy)_3]^{2+}$ reference standard. (**B**) Mass spectrum and ion mobility drift time distribution of the dual-spray product while electrospraying solutions of 2,2'-bipyridine and $RuCl_3$ and setting the resolving quadrupole to m/z 285.

The fragmentation of $[RuL_3]^{2+}$ complexes involve an initial neutral ligand loss to form $[RuL_2]^{2+}$ (channel A) then subsequent charge separation forming the $[L+H]^+$ and $[RuL - H]^+$ ions (channel B). Charge separation by formation of $L^{\cdot +}$ and $[RuL]^+$ is another possible dissociation channel, however it is difficult to confirm this due to H• loss from bpy and phen ligands. Katta and co-workers also demonstrated identical fragmentation of the $[Ru(bpy)_3]^{2+}$ and $[Ru(phen)_3]^{2+}$ complexes[92]. A neutral loss of HCN from the $[RuL - H]^+$ ion produces another singly charged fragment ion. The CID spectrum of the complex is shown in Figure 5.2 and the breakdown curve for the fragmentation of $[Ru(bpy)_3]^{2+}$ is shown in Figure 5.3. Similar fragment ions are generated when the dual-spray product is fragmented and its breakdown curve overlaps with the breakdown curve for the standard (Figure 5.4). The $[Ru(phen)_3]^+$ complex generates similar fragment ion types by CID compared with $[Ru(bpy)_3]^{2+}$, however the parent ion decay breakdown curve is shifted to the right (requires more energy to fragment) relative to the parent ion decay of $[Ru(bpy)_3]^{2+}$. This shift is due to the 1,10-phananthroline ligand containing more carbon atoms than the 2,2'-bipyridine ligand and thus the post-collisional redistribution of internal energy has more degrees of freedom for 1,10-phenanthroline.

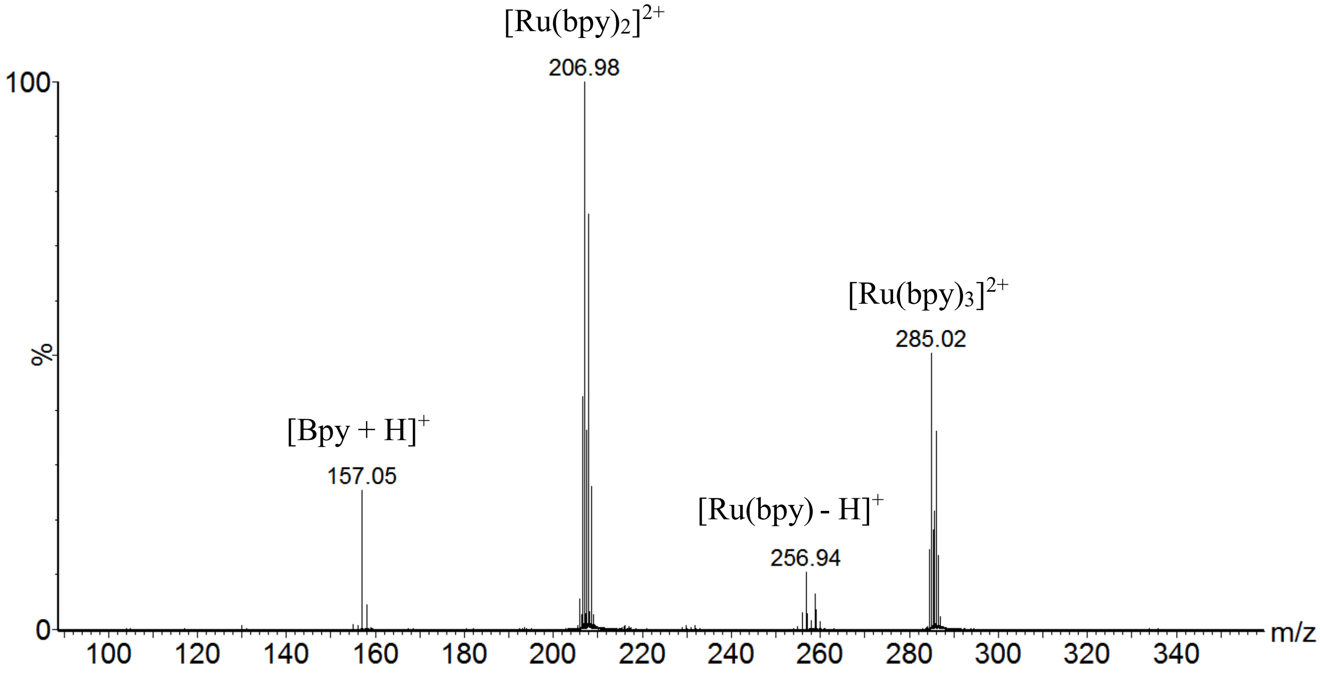

**Figure 5.2.** CID of $[Ru(bpy)_3]^{2+}$ complex at $E_{com} = 4.58$ eV. Parent ion $[Ru(bpy)_3]^{2+}$ and fragment ions are labelled.

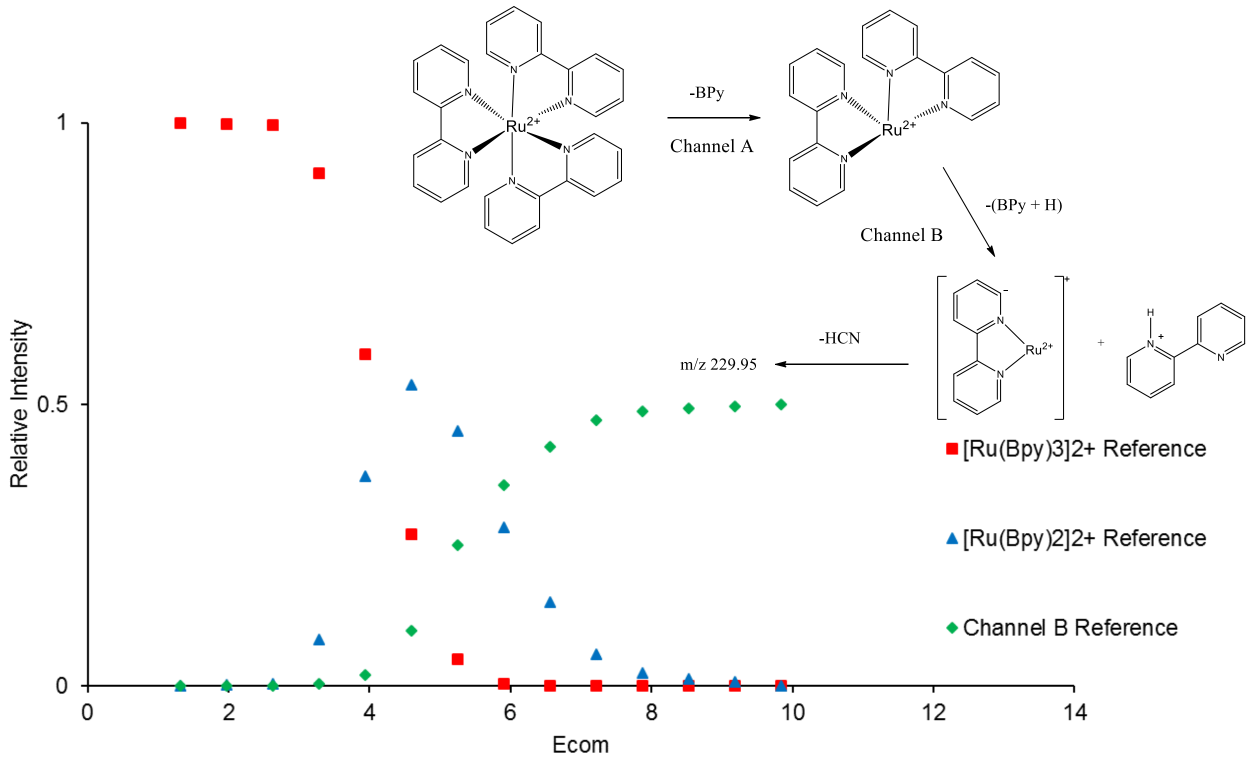

**Figure 5.3.** Breakdown curve of the $[Ru(bpy)_3]^{2+}$ reference complex and its dissociation mechanism. Channel A represents the average of $[Bpy+H]^+$, $[RuBpy - H]^+$ and $[RuBpy - H - HCN]^+$.

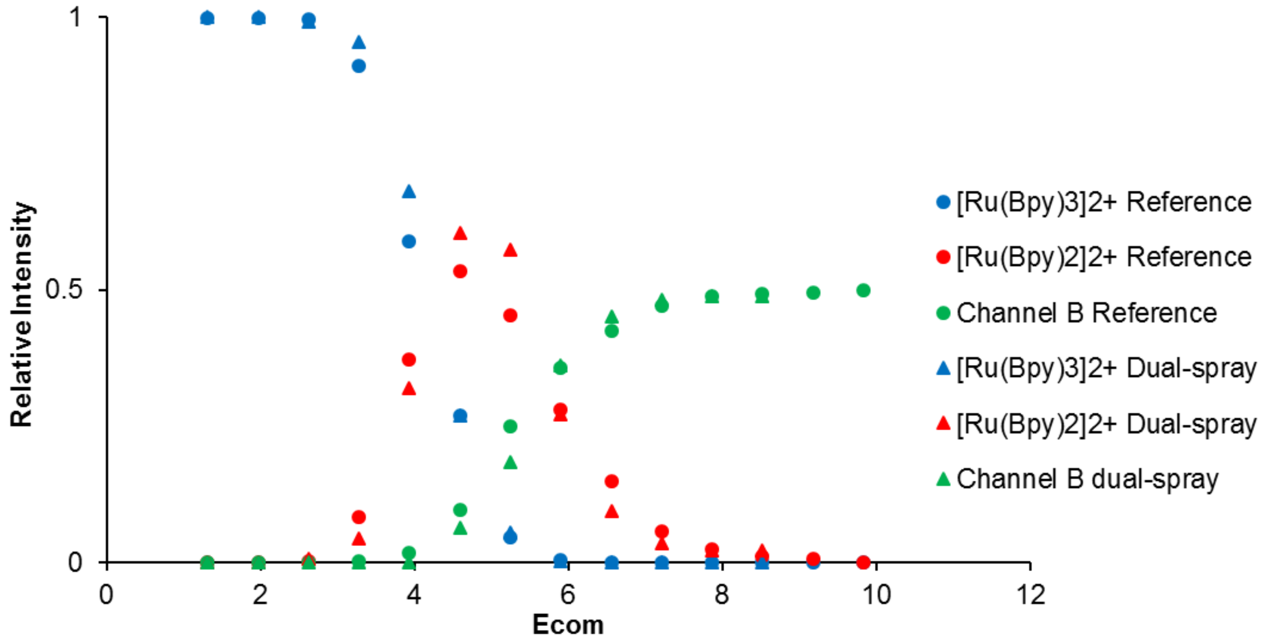

**Figure 5.4.** Overlapping breakdown curves for the dissociation of $[Ru(bpy)_3]^{2+}$ reference standard and product formed by the dual-spray reaction of $RuCl_3$ and 2,2'-bipyridine solutions.

Iron-pyridyl complexes were the second set of complexes to be synthesized using the dual-spray method. However, when solutions of pyridyl ligands and $FeSO_4$ are electrosprayed simultaneously, the mass spectra indicate the formation of $[FeL_2 + 2H]^{2+}$ and $[FeL_3 + 2H]^{2+}$ complexes, due to shift in the mass by 2 mass units compared to the $[FeL_3]^{2+}$ reference standards. For example, when solutions of 1,10-phenanthroline in MeOH and $FeSO_4$ in MeOH are electrosprayed, the major products are $[Fe(phen)_2 + 2H]^{2+}$ and $[Fe(phen)_3 + 2H]^{2+}$ complexes. The formation of $[Fe(phen)_3 + 2H]^{2+}$ is shown in Figure 5.5. The ion mobility chromatogram for the dual-spray product $[Fe(phen)_3 + 2H]^{2+}$ shows similar drift time to the $[Fe(phen)_3]^{2+}$ reference standard, the resolution of the ion mobility chromatogram using helium as the buffer gas is likely not high enough to resolve collision cross section differences between the $[Fe(phen)_3 + 2H]^{2+}$ and

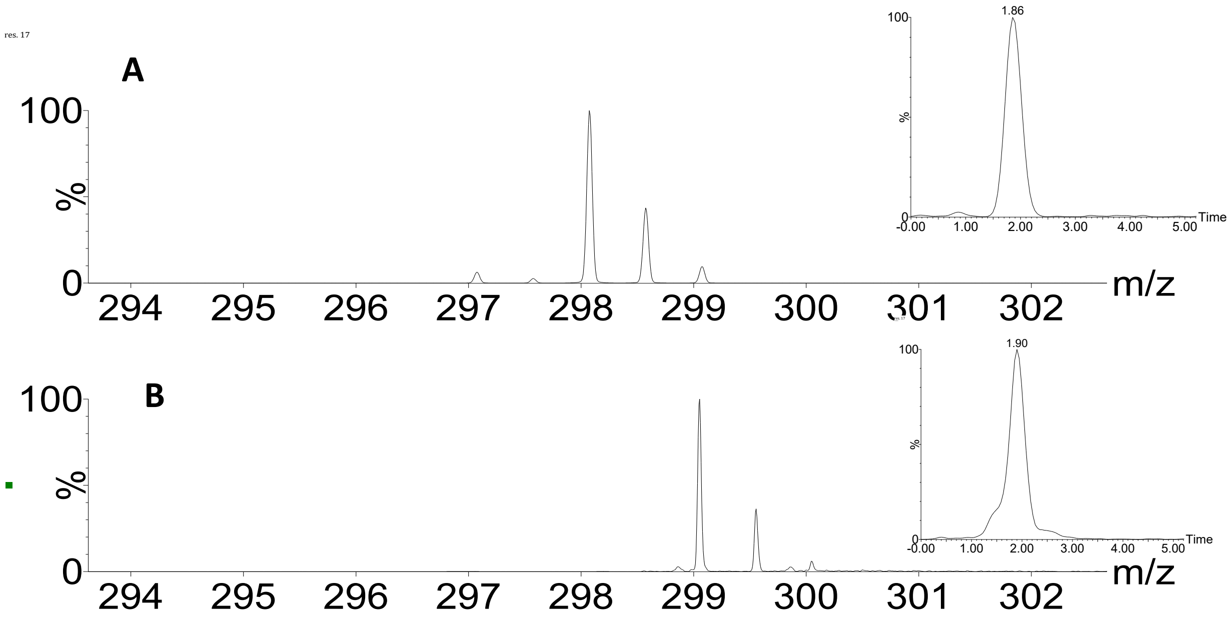

**Figure 5.5.** (**A**) Mass spectrum of $[Fe(phen)_3]^{2+}$ reference standard indicating the isotopic distribution for the complex and the ion mobility chromatogram of the standard. (**B**) Mass spectrum of the dual-spray product while electrospraying solutions of 1,10-phenanthroline and $FeSO_4$ showing the formation of $[Fe(phen)_3 + 2H]^{2+}$. Also shown is ion mobility drift time distribution of the $[Fe(phen)_3 + 2H]^{2+}$ product.

$[Fe(phen)_3]^{2+}$. Based on the similar ion mobility arrival time distributions, the dual-spray product $[Fe(phen)_3 + 2H]^{2+}$ is expected to have a similar structure to the octahedral $[Fe(phen)_3]^{2+}$.

The CID of $[Fe(phen)_3]^{2+}$ standard yields an initial neutral ligand loss which forms $[Fe(phen)_2]^{2+}$ (Figure 5.6). Subsequent fragmentation $[Fe(phen)_2]^{2+}$ results in three different dissociation channels; neutral ligand loss forming $[Fe(phen)]^{2+}$ (m/z 118), and two charge separations by $[phen+H]^{+}$ loss and $phen^{\bullet +}$ loss (Figure 5.7).

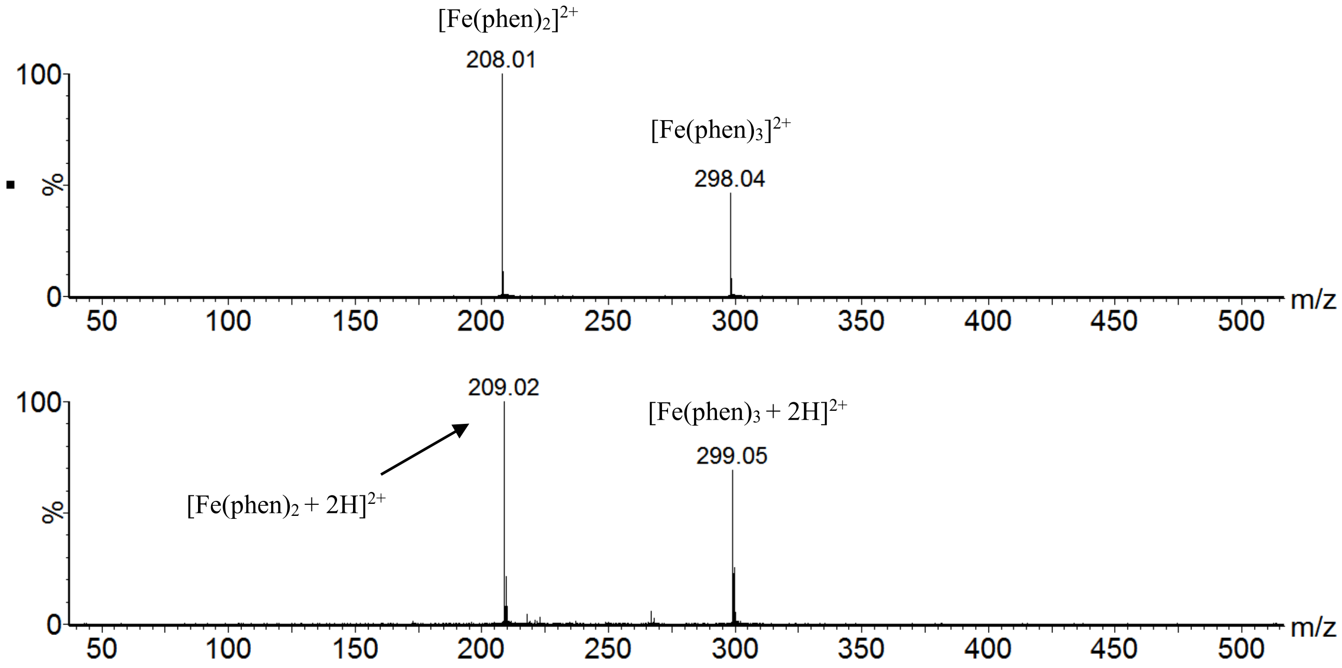

**Figure 5.6.** CID of $[Fe(phen)_3]^{2+}$ (top panel) and dual-spray product $[Fe(phen)_3 + 2H]^{2+}$ (bottom panel) at $E_{com} = 2.58$ eV.

These fragment ions were confirmed using in-source CID to form $[Fe(phen)_2]^{2+}$ and mass selecting this ion for another stage of fragmentation in the transfer collision cell. Similar neutral ligand loss for the dual-spray product $[Fe(phen)_3 + 2H]^{2+}$ is observed, however only the two charge separation channels (Channel B and C, Figure 5.8) are observed for the secondary dissociation, secondary neutral ligand loss is not observed for the $[Fe(phen)_3 + 2H]^{2+}$ complex. At relatively high collision energy ($E_{com}$ = 7.5 eV) the fragment ion $Fe^+$ is observed at m/z 56 for the reference standard, while $FeH_2^+$ (m/z 58) is observed for $[Fe(phen)_3 + 2H]^{2+}$.

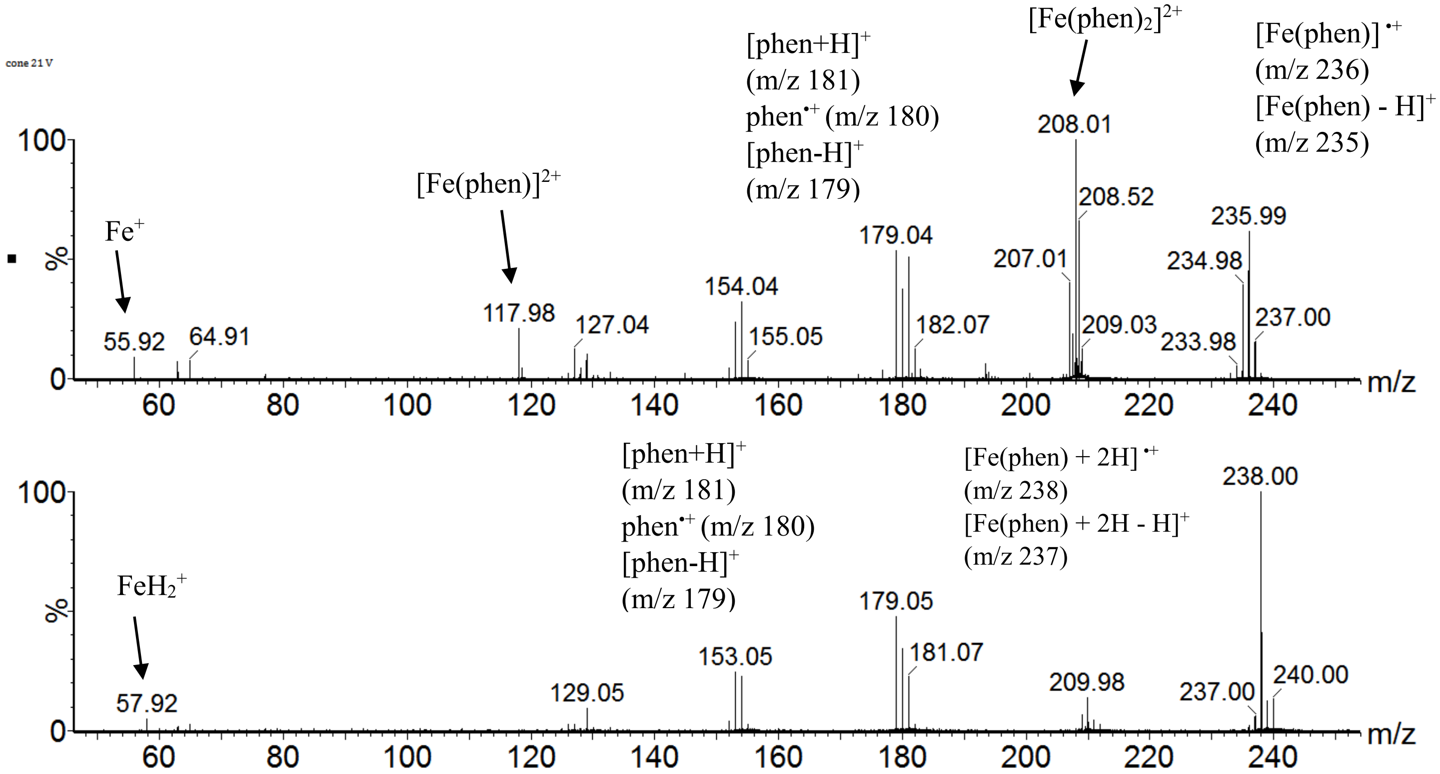

**Figure 5.7.** CID of di-ligated $[Fe(Phen)_2]^{2+}$ (top panel) and dual-spray product $[Fe(Phen)_2 + 2H]^{2+}$ (bottom panel) at $E_{com}$ = 7.54 eV.

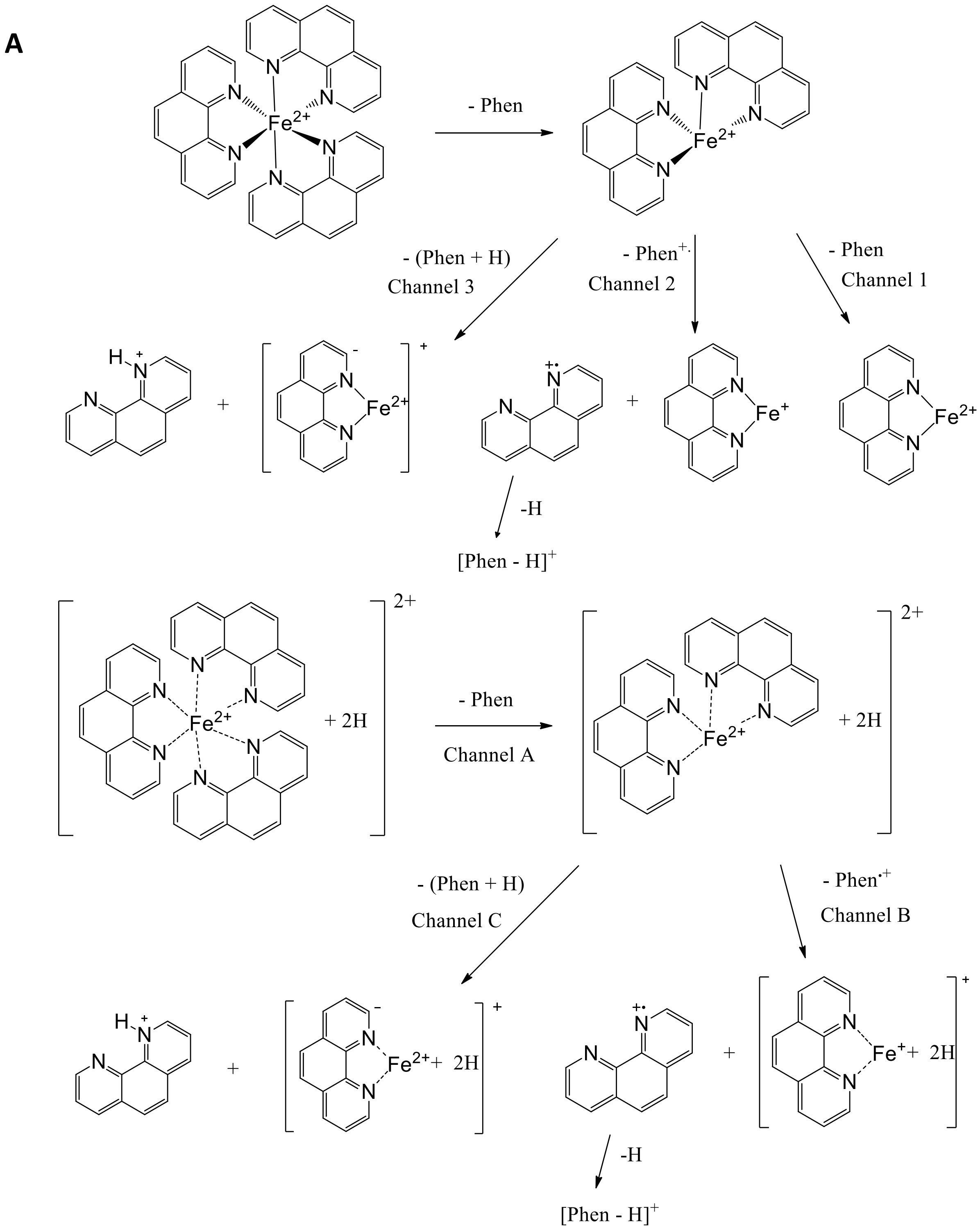

**Figure 5.8.** (**A**) CID fragmentation mechanism of $[Fe(phen)_3]^{2+}$ reference standard. (**B**) CID fragmentation mechanism of $[Fe(phen)_3 + 2H]^{2+}$ dual spray product.

Figure 5.9 indicates the breakdown curve for $[Fe(phen)_3]^{2+}$. The relative intensity of channel 1, 2, and 3 shows the competing nature of the secondary dissociation. Channel 2, which corresponds to the average intensity of $phen^{\bullet+}$, $[Fe(phen)]^{\bullet+}$, and $[phen\text{-}H]^+$ is the dominant channel for the secondary dissociation. Figure 5.10 shows the breakdown curve for the dissociation of the dual-spray product $[Fe(phen)_3 + 2H]^{2+}$. The charge separation channel which corresponds to the fragment ions $phen^{\bullet+}$, $[Fe(phen) + 2H]^{\bullet+}$, and $[phen\text{-}H]^+$ (Channel B) has a greater relative abundance compared to Channel C, which represents the fragment ion pair $[Fe(phen) + 2H - H]^+$ and $[phen + H]^+$. Thus the main difference between the CID fragmentations for the two complexes is the neutral loss of a secondary ligand.

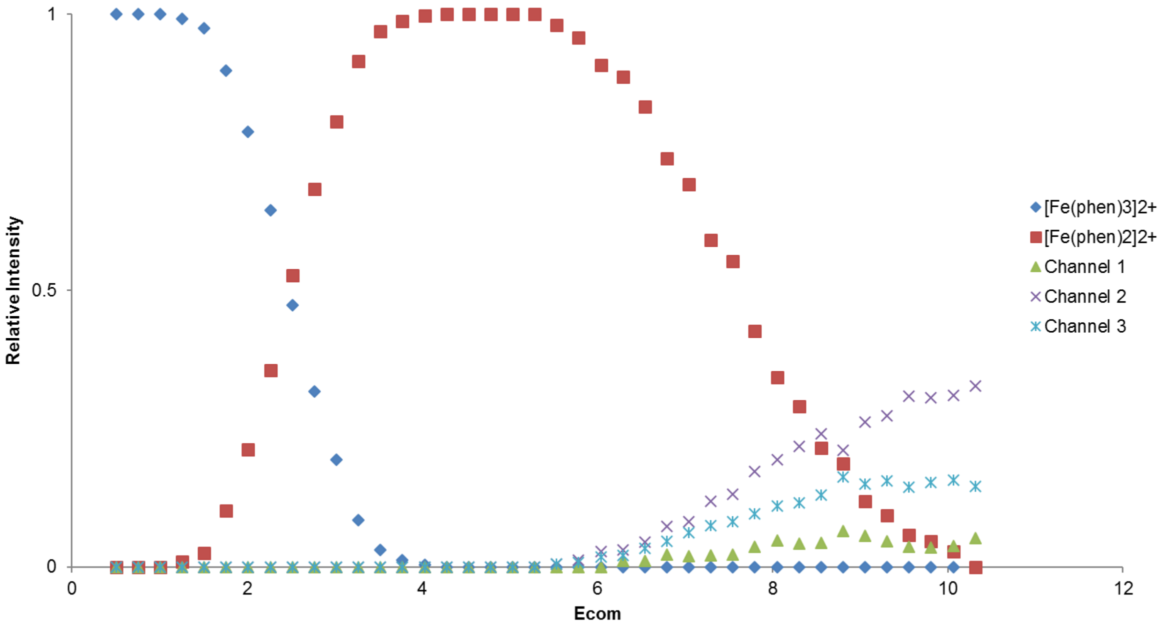

**Figure 5.9.** Breakdown curve of $[Fe(phen)_3]^{2+}$. Channel 1 corresponds to the relative intensity of $[Fe(phen)]^{2+}$. Channel 2 represents the average intensity of $phen^{\bullet+}$, $[Fe(phen)]^{\bullet+}$, and $[phen\text{-}H]^+$. Channel 3 represents the average intensity of $[Fe(phen) - H]^+$ and $[phen + H]^+$.

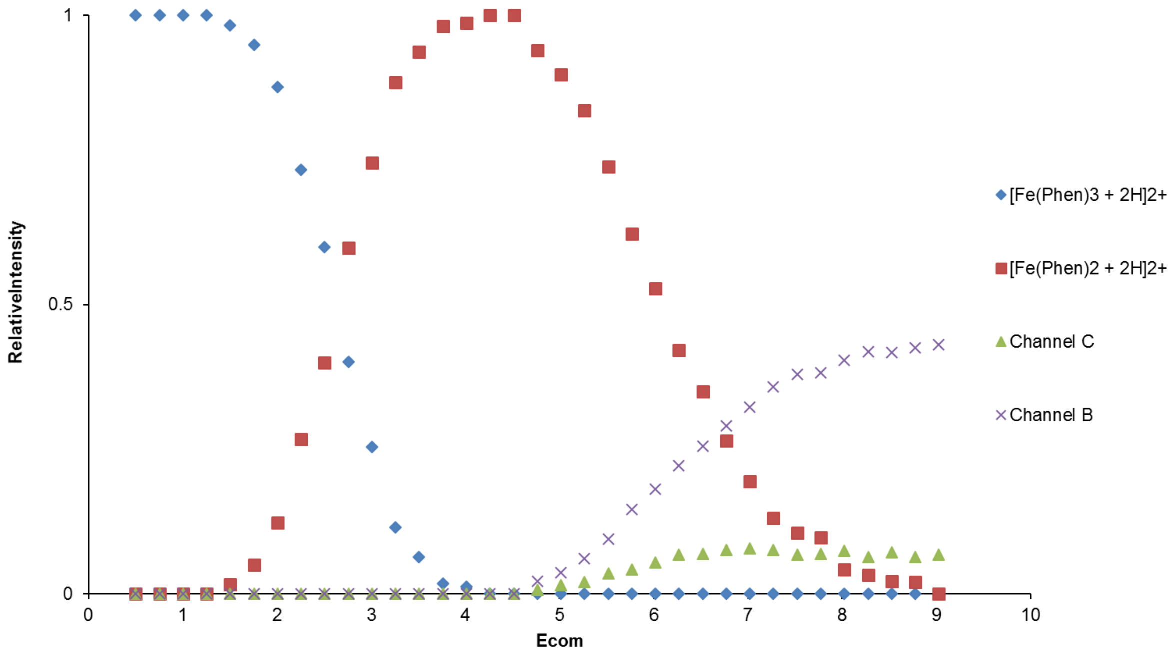

**Figure 5.10.** Breakdown curve of $[Fe(phen)_3 + 2H]^{2+}$. Channel B corresponds to the average intensity of $phen^{\bullet+}$, $[Fe(phen) + 2H]^{\bullet+}$, and $[phen\text{-}H]^+$. Channel C represents the average intensity of $[Fe(phen) + 2H - H]^+$ and $[phen + H]^+$.

Figure 5.11 indicates the overlapping primary and secondary dissociations for $[Fe(phen)_3 + 2H]^{2+}$ and $[Fe(phen)_3]^{2+}$ complexes. As seen in the overlapping breakdown curves, the parent ion decay is energetically equivalent for both complexes but the secondary ion decay is non-equivalent energetically. The non-equivalent secondary dissociation may be due to the two additional hydrogens added to the complex, which likely decreases the binding energy of the other ligands. As seen by these results, unique gas phase complexes can be generated using dual-spray reactions since $[Fe(phen)_3 + 2H]^{2+}$ is not observed in solution. In solution, the rate-limiting step for the formation of $[Fe(phen)_3]^{2+}$ is the complexation of phen to $[Fe(phen)_2]^{2+}$ and decreased reaction rates are observed at low pH due to equilibrium shift to generate $[phen+H]^+$

[25]. Since dual-spray reactions occur on a millisecond time scale and increased collision frequencies are at play, these factors may influence the formation of unique gas phase species.

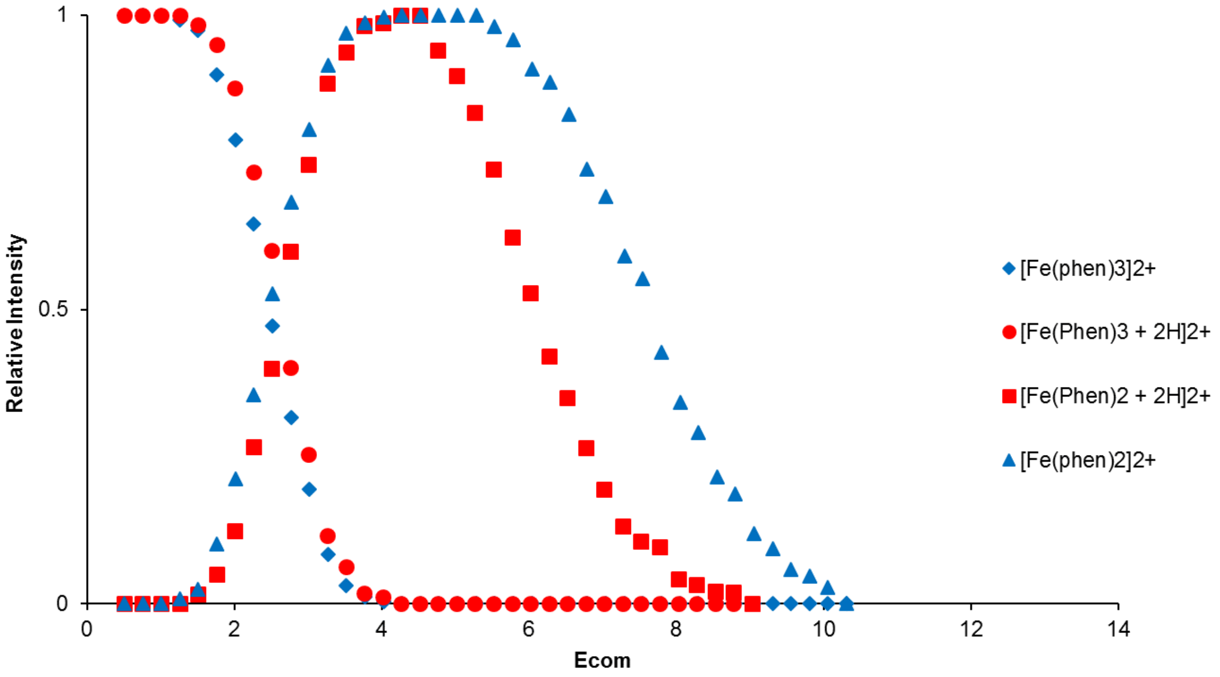

**Figure 5.11.** Overlap of the parent ion decays of $[Fe(phen)_3]^{2+}$, $[Fe(phen)_3 + 2H]^{2+}$ and secondary ions $[Fe(phen)_2]^{2+}$, $[Fe(phen)_2 + 2H]^{2+}$.

The CID fragmentation of $[Fe(bpy)_3]^{2+}$ generates a similar fragmentation mechanism to $[Fe(phen)_3]^{2+}$; initial neutral ligand loss is followed by a neutral ligand loss and two charge separation channels due to loss of $bpy^{\bullet+}$ and $[bpy+H]^+$. However, the energetics of the dissociations are dramatically different. Since bpy has less degrees of freedom than phen, bpy has less vibrational modes for the redistribution of internal energy. Thus the binding energy of the bpy to the central iron atom is less than phen. This is observed in the breakdown curves for $[Fe(bpy)_3]^{2+}$ and $[Fe(phen)_3]^{2+}$, the breakdown curve for $[Fe(bpy)_3]^{2+}$ shifted to lower $E_{com}$ (breakdown curve for $[Fe(bpy)_3]^{2+}$ is shown in Figure S11, Appendix). For the $[Fe(bpy)_3]^{2+}$ complex, similar results were obtained for the dual-spray reaction. The complexes generated by dual-spray include $[Fe(bpy)_3 + 2H]^{2+}$ and $[Fe(bpy)_2 + 2H]^{2+}$. Similarly to $[Fe(phen)_3 + 2H]^{2+}$, the CID mechanism of $[Fe(bpy)_3 + 2H]^{2+}$ involves an initial neutral ligand loss followed by two charge separation channels, secondary neutral ligand loss is not observed. However, the breakdown curves for the dual-spray product $[Fe(bpy)_3 + 2H]^{2+}$ overlap with the $[Fe(bpy)_3]^{2+}$ for the primary and secondary dissociation, thus they are equivalent energetically. The overlapping breakdown curves are shown in Figure S13 in the Appendix.

Mixed ligand complexes of iron were also investigated. When an equimolar solution of bpy and phen is added to a solution of $FeSO_4$ several complexes are formed in solution, which are shown in the ESI mass spectrum of this solution (Figure 5.12). There are a total of seven complexes formed in this solution, three of which are mixed ligand complexes; including $[Fe(phen)(bpy)]^{2+}$, $[Fe(phen)_2(bpy)]^{2+}$ and $[Fe(phen)(bpy)_2]^{2+}$. The ion count intensity of the $[Fe(phen)(bpy)]^{2+}$ complex is roughly two times greater than the tri-ligated mixed ligand complexes which indicates that the binding energy of the third ligand to Fe(II) is dramatically lower. Comparing the breakdown curves of $[Fe(phen)_2(bpy)]^{2+}$ and $[Fe(phen)(bpy)_2]^{2+}$ to the dissociation of $[Fe(phen)(bpy)]^{2+}$ also supports this assessment; full dissociation (parent ion intensity = 0) of the $[Fe(phen)_2(bpy)]^{2+}$ and $[Fe(phen)(bpy)_2]^{2+}$ complexes occurs at an $E_{com}$ of 1.3 eV while it occurs at an $E_{com}$ of 5 eV for $[Fe(phen)(bpy)]^{2+}$. The ion mobility arrival time distributions for all the complexes generated in solution are provided in Figure S14 in the Appendix.

The dual-spray reaction to form mixed ligand complexes of iron was performed with a solution of $FeSO_4$ ($10^{-3}$ M in MeOH) and an equimolar solution of bpy and phen ($10^{-4}$ M in MeOH) generates the mixed ligand complexes $[Fe(phen)(bpy) + 2H]^{2+}$, and $[Fe(phen)(bpy)_2 + 2H]^{2+}$. These complexes have similar ion mobility arrival time distributions compared to their respective reference standards generated in solution. Shown in Figure 5.13 is the dual-spray formation of the $[Fe(phen)(bpy)_2 + 2H]^{2+}$, with the resolving quadrupole set to m/z 275. The dual-spray formation of $[Fe(phen)_2(bpy) + 2H]^{2+}$ was not confirmed because CID was not possible due to very low intensity of this ion in the mass spectrum.

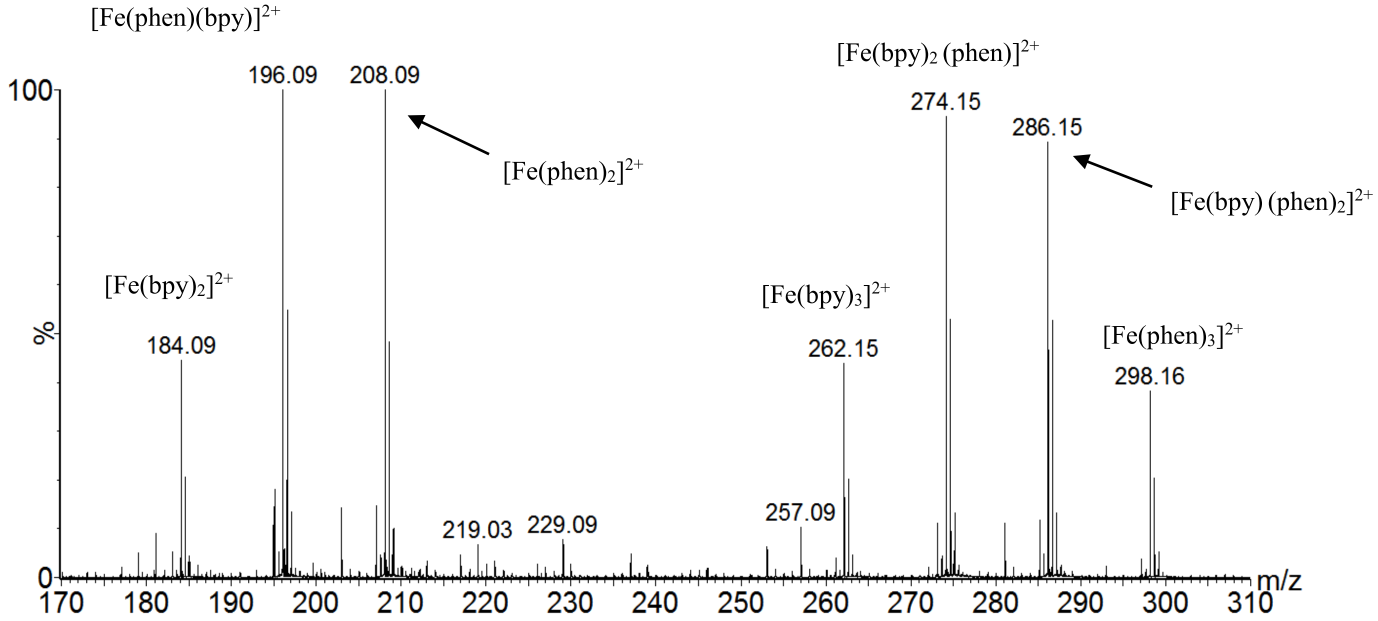

**Figure 5.12.** ESI mass spectrum of methanolic solution containing 20 μM $FeSO_4$, 1 μM 1,10-Phenanthroline, and 1 μM 2,2'-bipydine. The complexes generated in solution are indicated.

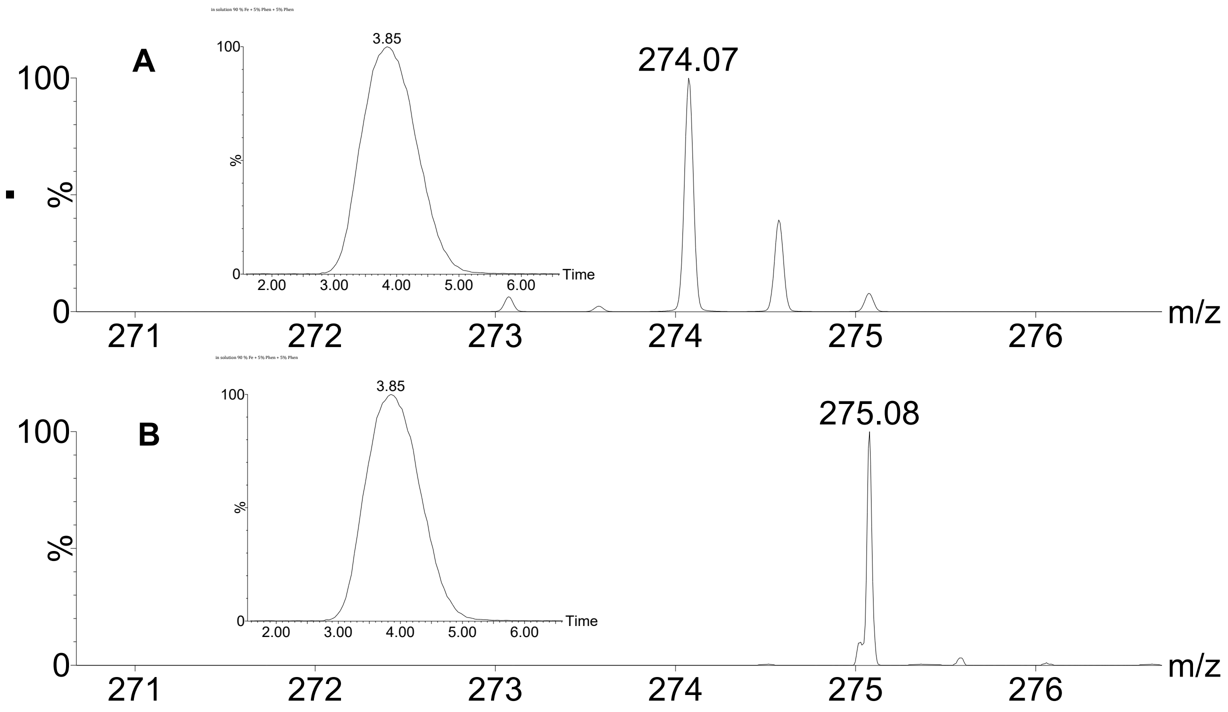

**Figure 5.13. (A)** ESI mass spectrum of [Fe(phen)(bpy)$_2$]$^{2+}$ showing its isotopic distribution and the ion mobility arrival time distribution for the ion. **(B)** ESI mass spectrum while electrospraying a solution of FeSO$_4$ and an equimolar solution of 2,2'-bypridine and 1,10-phenanthroline, which shows the formation of [Fe(phen)(bpy)$_2$ + 2H]$^{2+}$. The drift time distribution is also shown.

The CID fragmentation of the triligated mixed ligand complexes $[Fe(phen)_2(bpy)]^{2+}$ and $[Fe(phen)(bpy)_2]^{2+}$ have two competing dissociations channels for the initial ligand loss. These competing dissociation channels correspond to the loss of phen and the loss of bpy. For both complexes, the major dissociation channel corresponds to the neutral loss of bpy, which generates $[Fe(phen)(bpy)]^{2+}$ (m/z 196). Since the bpy ligand has less vibrational degrees of freedom, it has less binding energy to the central iron atom compared to the phen ligand. This initial dissociation of bpy is also observed for the dual-spray products $[Fe(phen)_2(bpy) + 2H]^{2+}$ and $[Fe(phen)(bpy)_2 + 2H]^{2+}$. Shown in Figure 5.14 is the CID of $[Fe(phen)(bpy)_2]^{2+}$ reference generated in solution and the dual-spray product $[Fe(phen)(bpy)_2 + 2H]^{2+}$ at low $E_{com}$. Further dissociation of $[Fe(phen)(bpy)]^{2+}$ yields a second neutral loss of bpy forming $[Fe(phen)]^{2+}$, in addition to several charge separation channels for the two different ligands (Figure S15,

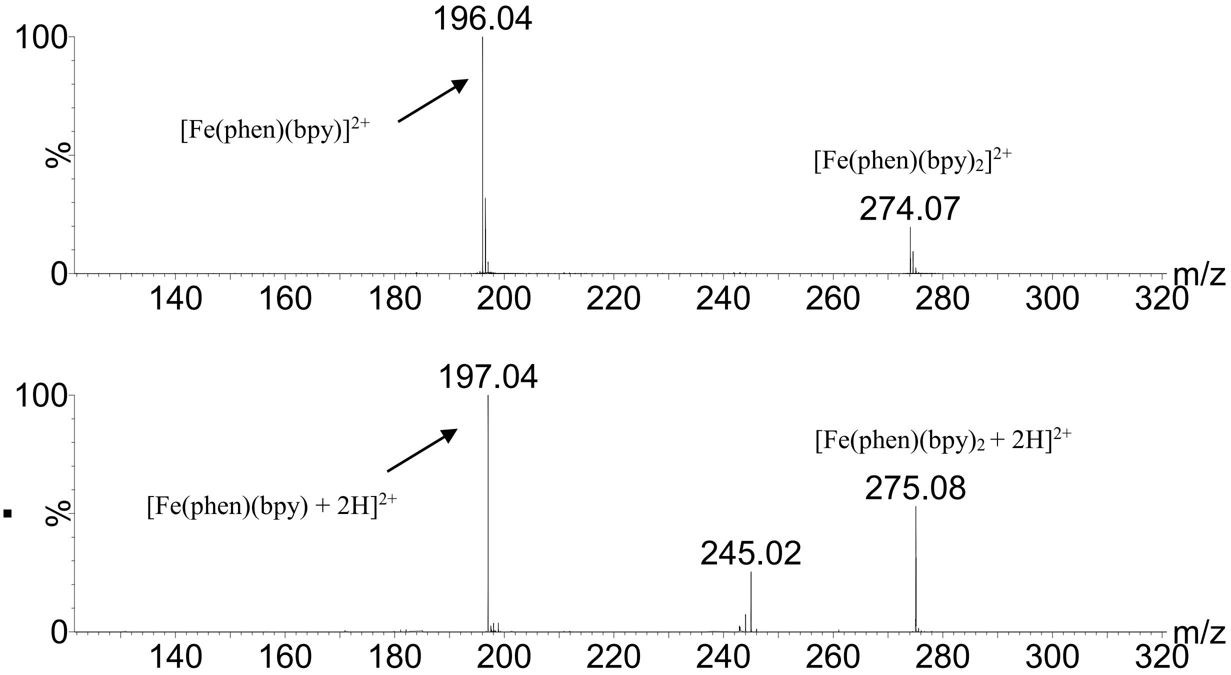

**Figure 5.14. (A)** CID of $[Fe(Phen)(Bpy)_2]^{2+}$ (m/z 274) and **(B)** CID of $[Fe(Phen)(Bpy)_2 + 2H]^{2+}$ (m/z 275) at $E_{com} = 0.54$ eV.

Appendix). The dissociation of the dual-spray product $[Fe(phen)(bpy)_2 + 2H]^{2+}$ is similar to $[Fe(phen)_3 + 2H]^{2+}$, secondary neutral ligand loss is not observed from the di-ligated complexes and the secondary fragmentation is energetically distinct from the reference compounds (Figure 5.15). These results provide further evidence that unique gas phase complexes are generated by in-source dual-spray reactions.

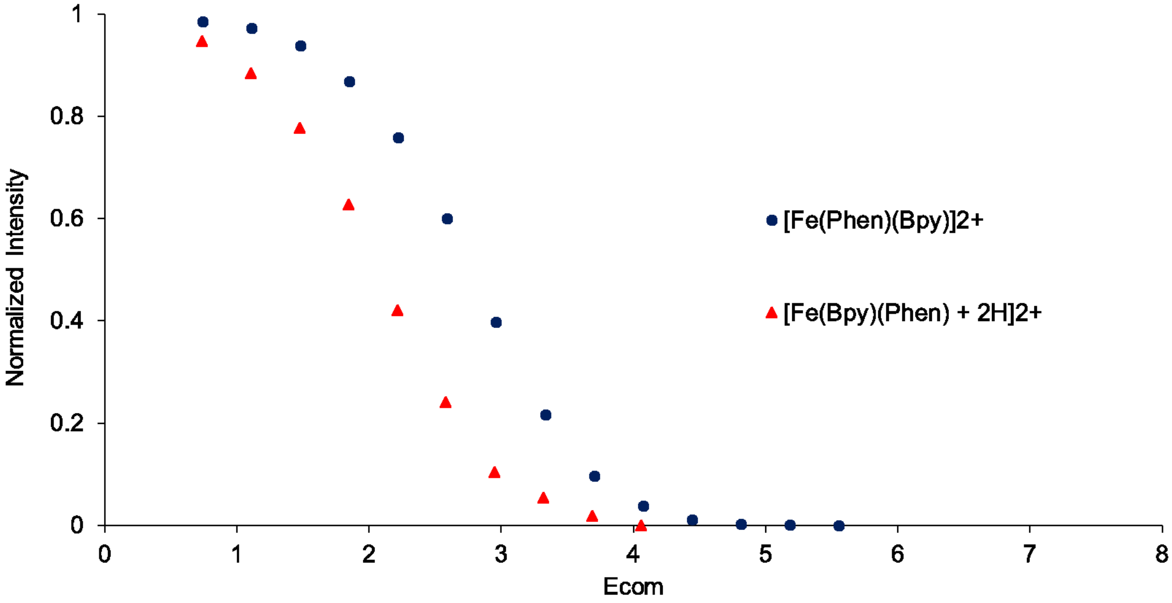

**Figure 5.15.** Breakdown curves of the di-ligated mixed ligand complexes $[Fe(phen)(bpy)]^{2+}$ and $[Fe(phen)(bpy) + 2H]^{2+}$ showing the energetically different dissociations.

## 5.2 Structure of +2H species

The $[Fe(phen)_3 + 2H]^{2+}$ complex is not present in the solution phase, thus it is a unique gas phase complex formed by the dual-spray reaction. By CID, the fragment ions containing iron are two mass units greater than expected which indicates that the additional hydrogens may be present on the iron atom. However, hydrogens are typically labile in CID experiments[66] and thus may be initially on the ligands and transfer to iron during the fragmentation process. To test this theory, molecular simulations were done to compare the energies of the complexes with hydrogens on different locations. Using density functional theory (DFT) calculations, the energies of the complexes can be compared. The B3LYP functional and LanL2DZ basis set were used to optimize geometries after an initial guess of the structure was done using the semi-empirical method PM6. Using the low level PM6 allows for a faster geometry optimization since the molecule is closer to its stationary point. Initially, the additional hydrogens for the $[Fe(phen)_3 + 2H]^{2+}$ complex were placed on the iron atom, however, as the geometry was optimized, the hydrogens had been transferred to the nitrogen atoms of the 1,10-phenanthroline ligands. This is likely due to the fact that $Fe^{2+}$ typically has a coordination number of six and this is already satisfied by the three bidentate ligands of 1,10-phenanthroline.

For the $[Fe(phen)_3 + 2H]^{2+}$ complex, the geometry optimization was done on the singlet spin state, as this is less computationally demanding than an unrestricted B3LYP method. There are three possible structures for $[Fe(phen)_3 + 2H]^{2+}$, the lowest energy geometry is structure **A1** (Figure 5.16). Structure **A1** has the additional hydrogen atoms covalently bonded to the nitrogen atoms of the same phen ligand and all six of the nitrogens are coordinating to the central iron atom. This structure has an octahedral geometry, which is also the known geometry of the $[Fe(phen)_3]^{2+}$ complex and since the ion mobility data provided similar drift time distributions for the $[Fe(phen)_3 + 2H]^{2+}$ and $[Fe(phen)_3]^{2+}$ complexes, it is reasonable to infer that $[Fe(phen)_3 + 2H]^{2+}$ has an octahedral geometry. From the optimized structures of $[Fe(phen)_3 + 2H]^{2+}$, the nitrogen atoms with an additional hydrogen atom covalently bonded may or may not be involved in coordination to the central iron atom. Nitrogen atoms with an additional hydrogen and are involved in coordination are tetrahedral in geometry and are closer in space to the central iron atom (2.04 Å from iron), whereas nitrogen atoms not involved in coordination are planar and further from the central iron atom (3.43 Å from iron) as in structure **A2** and **A3**. In all optimized

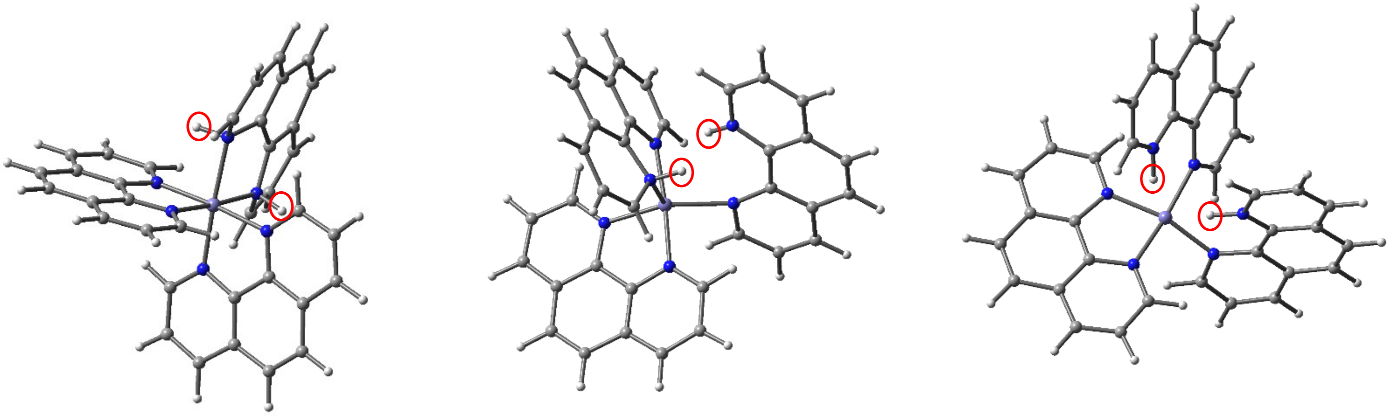

**A1** (0) **A2** (+102.5) **A3** (+1706.6)

**Figure 5.16.** Geometry optimizations using B3LYP functional and the LANL2DZ basis set for the isomers of $[Fe(phen)_3 + 2H]^{2+}$. Relative energies, in kJ mol$^{-1}$, shown in parentheses. Additional hydrogen atoms are indicated by red circles.

structures of $[Fe(phen)_3 + 2H]^{2+}$, a non-coordinating nitrogen atom generates a distorted structure which no longer has an octahedral geometry. Greater distortion of the original octahedral geometry leads to a higher energy structure on the potential energy surface. This is observed in structure **A2** (5 coordinating nitrogen atoms) and structure **A3** (4 coordinating nitrogen atoms).

For geometry optimizations of the fragment ions, optimizations of higher spin states were possible due to lower number of atoms (less computationally demanding). Molecular simulations on the fragment ion $[Fe(phen)_2 + 2H]^{2+}$ indicate that the lowest energy geometry, has the hydrogen atoms bonded to the nitrogens of opposite ligands, presented in Figure 5.17 as structure **B1**. The spin state for this geometry is triplet and three nitrogen atoms are involved in coordination to the central iron atom. Structure **B2**, which has both hydrogens covalently bonded to the nitrogen atoms of the same ligand (all nitrogen atoms coordinating to iron), is +49.5 kJ/mol higher in energy than the lowest energy structure **B1**. The singlet spin states of **B1** and **B2** are higher in energy (+188.5 kJ/mol and +151.4 kJ/mol, respectively). Structure **B3** (singlet) has both hydrogen atoms bonded to the central iron atom and is +76.7 kJ/mol higher in energy than structure **B1**. The triplet spin state of structure **B3** yields one imaginary frequency, which corresponds to a transition state structure along the PES. The geometry of the $Fe(phen)_2$ portion of structure **B3** is an intermediate geometry between octahedral and tetrahedral. Similar geometries have been reported for iron carbonyl hydrides, which also have two coordinating hydrogen atoms[93]. After the initial ligand loss from the parent ion $[Fe(phen)_3 + 2H]^{2+}$, the additional hydrogen atoms likely transfer to the central iron atom. The hydrogen atoms may be shifting to the central iron atom to compensate for the lower coordination number for the iron. This theory is consistent with the observation that all fragment ions of $[Fe(phen)_3 + 2H]^{2+}$ which contain the iron atom are two mass units greater than expected. Additional hydrogens bound to

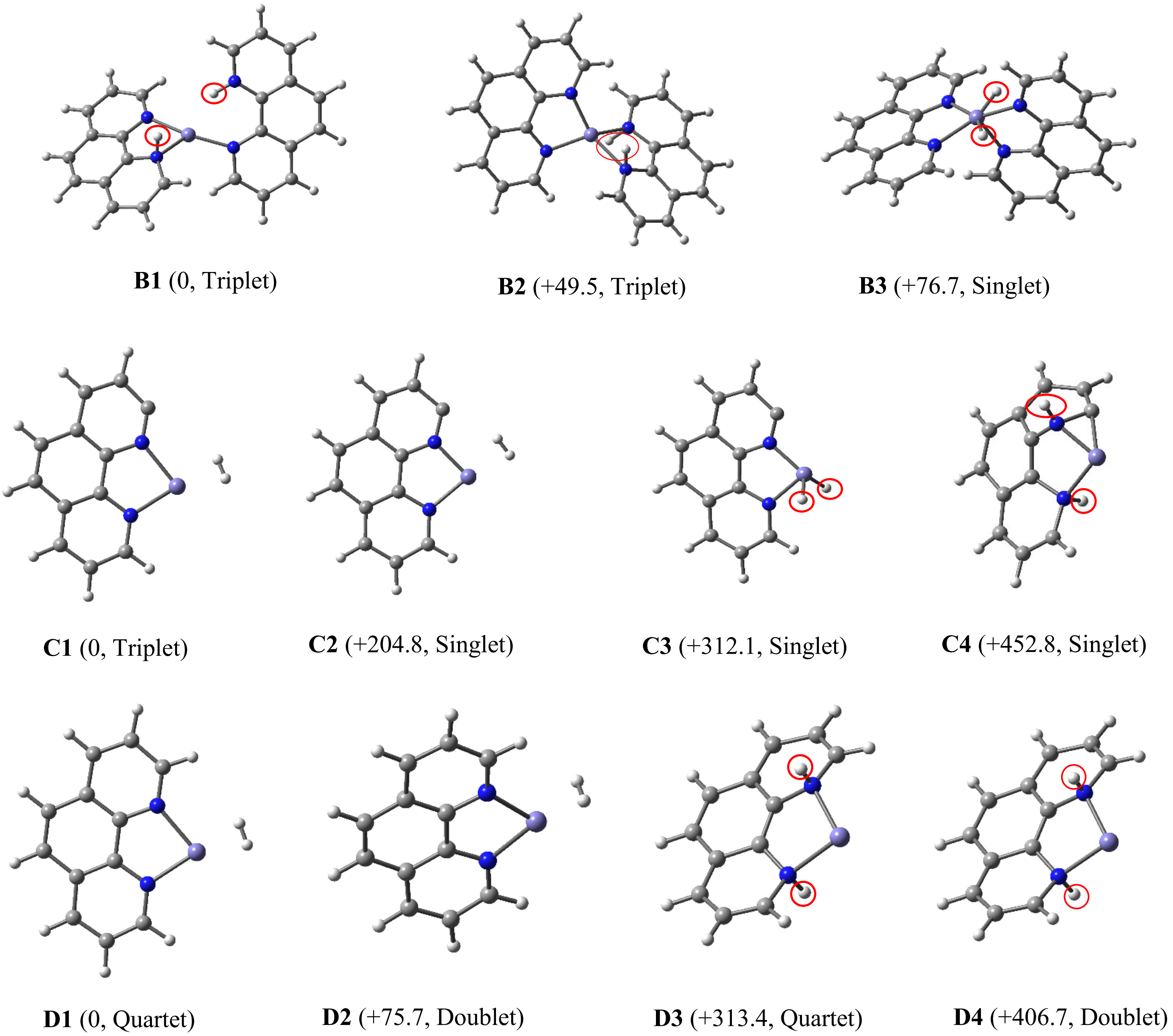

**B1** (0, Triplet) **B2** (+49.5, Triplet) **B3** (+76.7, Singlet)

**C1** (0, Triplet) **C2** (+204.8, Singlet) **C3** (+312.1, Singlet) **C4** (+452.8, Singlet)

**D1** (0, Quartet) **D2** (+75.7, Doublet) **D3** (+313.4, Quartet) **D4** (+406.7, Doublet)

**Figure 5.17.** Geometry optimizations using B3LYP functional and the LANL2DZ basis set for the isomers of $[Fe(phen)_2 + 2H]^{2+}$ (**B1-B3**), $[Fe(phen) + 2H - H]^{+}$ (**C1-C4**), $[Fe(phen) + 2H]^{\bullet+}$ (**D1-D4**). Relative energies, in kJ $mol^{-1}$ and spin states are shown in parentheses. Additional hydrogens indicated by red circles.

iron reduces the binding energy of the second phen ligand compared to $[Fe(phen)_2]^{2+}$, which is observed in the overlapping breakdown curves of the two species (Figure 5.11).

Fragmentation of the $[Fe(phen)_2 + 2H]^{2+}$ ion produces fragment ions pairs of $[Fe(phen) + 2H]^{\bullet +}$ and $phen^{\bullet +}$ in addition to $[Fe(phen) + 2H - H]^{+}$ and $[phen + H]^{+}$. Geometry optimizations indicate that the two additional hydrogen atoms remain on the central iron atom for the fragment ions $[Fe(phen) + 2H]^{\bullet +}$ and $[Fe(phen) + 2H - H]^{+}$ (structure **C1** and **D1** in Figure 5.17). For the $[Fe(phen) + 2H]^{\bullet +}$ and $[Fe(phen) + 2H - H]^{+}$ fragment ions, the lowest energy geometries have the hydrogen atoms in close proximity to each other (0.8 Å), which is the typical bond length of an H-H bond in diatomic hydrogen (structure **C1** and **D1**). Thus from these optimized structures, $H_2$ may be coordinating to the central iron atom of the fragment ions $[Fe(phen) + 2H]^{\bullet +}$ and $[Fe(phen) + 2H - H]^{+}$. Higher energy structures for the deprotonated fragment $[Fe(phen) + 2H - H]^{+}$ include structure **C2** (singlet of **C1**, +204.8 kJ/mol), **C3** (hydrogens directly bonded to central iron atom, +312.1 kJ/mol) and **C4** (hydrogens bonded to coordinating nitrogen atoms, +452.8 kJ/mol). Structure **C3** does not form diatomic hydrogen like structure **C1**; the formation of diatomic hydrogen adds more stability to the complex, explained by the +312.1 kJ/mol difference in energy. For the $[Fe(phen) + 2H]^{\bullet +}$ fragment ion, there is dramatic distortion in the phen ligand in structure **D3** and **D4** which adds +313.4 kJ/mol and +406.7 kJ/mol, respectively, relative to the lowest energy structure **D1**.

A relative energy diagram for the dissociation of $[Fe(phen)_3 + 2H]^{2+}$ is shown in Figure 5.18. The products of the primary dissociation, $[Fe(phen)_2 + 2H]^{2+}$ and phen, are +330 kJ/mol higher in energy compared with the parent ion $[Fe(phen)_3 + 2H]^{2+}$. Dissociation channel A is followed by channel B (+23 kJ/mol) and C (+116 kJ/mol). Channel B represents $phen^{\bullet +}$ loss while channel C corresponds to $[phen + H]^{+}$ loss from $[Fe(phen)_2 + 2H]^{2+}$. Assuming that the relative heights of the transition state barriers are proportional to the relative energies of the two dissociation channels, channel B is the dominant channel. The dominance of channel B is also seen in the breakdown curve of $[Fe(phen)_3 + 2H]^{2+}$ (Figure 5.9) where the relative abundance of channel B is greater than channel C. Therefore, the experimental breakdown curves agrees well will the theoretical calculations. To determine the rate constants *k* of the dissociation channels, calculations of transition state structures and RRKM modeling of the breakdown curves should be done in future studies. This will allow the competing dissociation channels to be better understood.

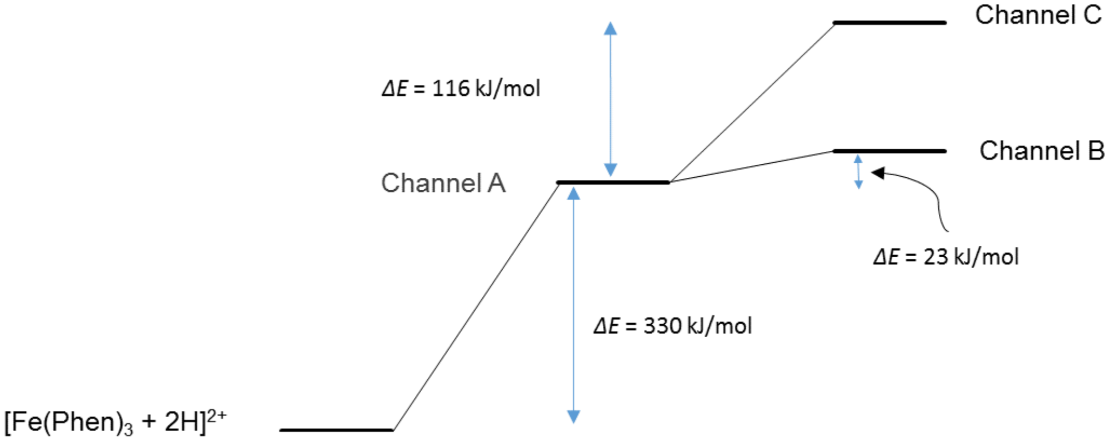

**Figure 5.18.** Relative energy diagram for the dissociation of $[Fe(phen)_3 + 2H]^{2+}$. Channel A represents the initial neutral loss to form the $[Fe(phen)_2 + 2H]^{2+}$ complex. Channel B corresponds to the product channel $[Fe(phen) + 2H]^{\bullet+}$ and $phen^{\bullet+}$. Channel C corresponds to the products $[Fe(phen) + 2H - H]^{+}$ and $[phen + H]^{+}$.

Additional experiments were completed to determine the source of the additional hydrogen atoms on the dual-spray complex $[Fe(phen)_3 + 2H]^{2+}$. Various aprotic solvents such as hexanes, DMSO, and DMF were used in the dual-spray reactions to observe if the solvent is responsible for the additional hydrogens bound to the complex. However, these solvents are not ideal for electrospray ionization mass spectrometry. The solvents typically used for ESI must be polar, have moderate boiling points, and must be easily oxidized/reduced in the source (water, methanol, acetonitrile). The use of hexanes did not solubilize the 1,10-phenanthroline ligand as required and DMF did not produce any meaningful signal for the analyte. DMSO was able to generate signals of the analyte, however when a ligand solution in DMSO and a solution of $FeSO_4$ is dual-sprayed, DMSO acts as a ligand and forms complexes with iron (Appendix). DMSO is known to act as a ligand in coordination chemistry[94] and since it is present in bulk compared to the 1,10-phenanthroline ligand, it readily forms complexes with iron. The source of one of the additional hydrogen atoms may be the iron sulfate solution which generates $FeH^+$ in the ESI mass spectrum of the $FeSO_4$ solution. However, an experiment which involved electrospraying a terpyridine (tpy) solution through a neutral ESI emitter and the iron solution through a positive polarity, showed the formation of $[Fe(tpy)_3]^{2+}$; no additional hydrogens were added to the complex. This result may indicate that the additional the source of the additional hydrogens is the ligand solution.

# Chapter 6. Conclusion

In this dissertation, we demonstrated that conducting HDX reactions within the ion-source is possible using dual electrospray emitters. Short peptides such as Phe-Leu-Glu-Glu-Leu and oxytocin provided a proof of concept that the dual-spray method is an effective way of conducting HDX reactions. Clear shifts in isotope distributions indicated hydrogen-deuterium exchange occurring within the ion source. Also demonstrated was simultaneous HDX reactions on two isobaric species, the oxytocin monomer and dimer, using ion mobility. It was found that the desolvation temperature, which typically affect the observed rate of exchange, does not influence the rate in dual-spray HDX reactions. Larger proteins such as ubiquitin, lysozyme, and cytochrome c provided an opportunity to test dual-spray HDX reactions as a method to probe protein structure. ESI charge state distributions and average number of exchanges from dual-spray HDX reactions of the native and denatured forms of these proteins provided insight into the conformations of the species present in the gas phase. Pairing the dual-spray HDX method to HPLC was shown as an effective method of probing gas-phase conformations of mixtures of multiple proteins. Increasing the distance of the analyte ESI emitter did not affect the deuterium uptake; this observation along with no temperature dependence for deuterium uptake suggests that the mechanism of the dual-spray HDX is a gas phase process. Deuterium labeling can occur on a millisecond time scale in the gas phase and the acid quenching steps involved with solution phase HDX can be surpassed.

The dual-spray reaction was also used for the synthesis of transition-metal pyridyl complexes. Based on similar spectral results and dissociation energetics, the formation of $[Ru(bpy)_3]^{2+}$ and $[Ru(phen)_3]^{2+}$ was confirmed. Similar mass spectra, ion mobility drift time distributions, fragment ions by CID, and overlapping breakdown curves with reference standards confirmed the formation of these species with the ESI source. The attempted dual-spray synthesis of iron pyridyl complexes resulted in the formation of a unique gas phase species which had two additional hydrogen atoms, $[Fe(phen)_3 + 2H]^{2+}$ and $[Fe(bpy)_3 + 2H]^{2+}$. This was also observed for the mixed ligand complexes, $[Fe(phen)(bpy) + 2H]^{2+}$ and $[Fe(phen)(bpy)_2 + 2H]^{2+}$. The CID of these complexes indicated similar initial ligand losses compared to the reference standards, however the secondary channels were distinct (secondary neutral ligand loss was not observed for these unique complexes). As seen in the breakdown curves, the initial ligand loss is also similar energetically to the reference standards but the secondary dissociation is energetically distinct. The additional hydrogen atoms clearly reduce the binding energy of the second ligand, thus less energy is required for its dissociation.

Using DFT calculations, possible geometries for the $[Fe(phen)_3 + 2H]^{2+}$ and its fragment ions were calculated. The lowest energy structure calculated for $[Fe(phen)_3 + 2H]^{2+}$ has an octahedral geometry with the additional hydrogen atoms covalently bound to the coordinating nitrogen atoms of the same ligand. Higher energy structures have non-coordinating nitrogen atoms which generates a distorted structure. The lowest energy structures for the single ligand complexes have diatomic hydrogen bound to the central iron atom. This agrees well with CID data, which shows that all fragment ions containing iron are two mass units greater than expected. The relative energy of the charge separation channels of $[Fe(phen)_2 + 2H]^{2+}$, radical cation ligand loss (channel B) and protonated ligand loss (channel C) were compared on a relative energy diagram for the dissociation reactions. Channel B is +23 kJ/mol relative to $[Fe(phen)_2 + 2H]^{2+}$ while Channel C is +116 kJ/mol. This difference in energy explains the dominance of the radical cation ligand loss relative to protonated ligand loss, which is observed in the breakdown curve for the dissociation.

# Contributions to Original Research

The dual-spray HDX method is a novel method of conducting HDX reactions within the ion source of the mass spectrometer. Deuterium labelling occurs on a millisecond time scale and the acid quenching step associated with traditional continuous labelling can be surpassed. Recently we have published this work in Rapid Communications in Mass Spectrometry:

> Rashid, S., Overton, S., Mazigh, B., Mayer, P.M.: Dual-spray hydrogen/deuterium exchange (HDX) reactions: A new method of probing protein structure. Rapid Communications in Mass Spectrometry. **30**, 1505-1512 (2016)

The dual-spray method of synthesizing organometallic species is innovative in that it allows the study of unique complexes formed in the gas phase. The formation of the unique complexes $[Fe(phen)_3 + 2H]^{2+}$, $[Fe(bpy)_3 + 2H]^{2+}$ and mixed ligand complexes in the gas phase provides an opportunity to study the structure and dissociation kinetics of truly unique species. In the coming months, we plan to publish this study in the International Journal of Mass Spectrometry.

# References

1. Song, H., Chen, D.L., Ismagilov, R.F.: Reactions in droplets in microfluidic channels. Angewandte chemie international edition. **45**, 7336-7356 (2006)
2. Girod, M., Moyano, E., Campbell, D.I., Cooks, R.G.: Accelerated bimolecular reactions in microdroplets studied by desorption electrospray ionization mass spectrometry. Chemical Science. **2**, 501-510 (2011)
3. Bain, R., Pulliam, C., Cooks, G.: Accelerated Hantzsch electrospray synthesis with temporal control of reaction intermediates. Chemical Science. **6**, 397-401 (2015)
4. Spence, T., Burns, T., Posey, L.A.: Controlled Synthesis of Transition-Metal Ion Complex/Solvent Clusters by Electrospray Ionization. Journal of Physical Chemistry. **101**, 139-144 (1997)
5. Kostyukevich, Y., Kononikhin, A., Popov, I., Nikolaev, E.: Conformational changes of ubiquitin during electrospray ionization as determined by in-ESI source H/D exchange combined with high-resolution MS and ECD fragmentation. Journal of Mass Spectrometry. **49**, 989-994 (2014)
6. Meng, C.K., Fenn, J.B.: Formation of charged clusters during electrospray ionization of organic solute species. Organic Mass Spectrometry. **26**, 542-549 (1991)
7. Shen, J., Brodbelt, J.: Formation of doubly charged transition metal–polyether–pyridyl mixed-ligand complexes by electrospray ionization. Journal of Mass Spectrometry. **34**, 137-146 (1999)
8. Williams, D.K., McAlister, G.C., Good, D.M., Coon, J.J., Muddiman, D.C.: Dual electrospray ion source for electron-transfer dissociation on a hybrid linear ion trap-orbitrap mass spectrometer. Analytical chemistry. **79**, 7916-7919 (2007)
9. Xia, Y., Liang, X., McLuckey, S.A.: Pulsed dual electrospray ionization for ion/ion reactions. Journal of the American Society for Mass Spectrometry. **16**, 1750-1756 (2005)
10. Cotham, V.C., Shaw, J.B., Brodbelt, J.S.: High-Throughput Bioconjugation for Enhanced 193 nm Photodissociation via Droplet Phase Initiated Ion/Ion Chemistry Using a Front-End Dual Spray Reactor. Analytical chemistry. **87**, 9396-9402 (2015)
11. Chen, H., Venter, A., Cooks, R.G.: Extractive electrospray ionization for direct analysis of undiluted urine, milk and other complex mixtures without sample preparation. Chemical Communications. 2042-2044 (2006)
12. Chen, H., Wortmann, A., Zhang, W., Zenobi, R.: Rapid In Vivo Fingerprinting of Nonvolatile Compounds in Breath by Extractive Electrospray Ionization Quadrupole Time-of-Flight Mass Spectrometry. Angewandte Chemie. **119**, 586-589 (2007)
13. Rashid, S., Overton, S., Mazigh, B., Mayer, P.M.: Dual-spray hydrogen/deuterium exchange (HDX) reactions: A new method of probing protein structure. Rapid Communications in Mass Spectrometry. **30**, 1505-1512 (2016)
14. Marcsisin, S.R., Engen, J.R.: Hydrogen exchange mass spectrometry: what is it and what can it tell us? Analytical and bioanalytical chemistry. **397**, 967-972 (2010)
15. Percy, A.J., Rey, M., Burns, K.M., Schriemer, D.C.: Probing protein interactions with hydrogen/deuterium exchange and mass spectrometry—a review. Analytica chimica acta. **721**, 7-21 (2012)
16. Wales, T.E., Engen, J.R.: Hydrogen exchange mass spectrometry for the analysis of protein dynamics. Mass spectrometry reviews. **25**, 158-170 (2006)

17. Konermann, L., Pan, J., Liu, Y.-H.: Hydrogen exchange mass spectrometry for studying protein structure and dynamics. Chemical Society Reviews. **40**, 1224-1234 (2011)
18. Krishna, M.M., Hoang, L., Lin, Y., Englander, S.W.: Hydrogen exchange methods to study protein folding. Methods. **34**, 51-64 (2004)
19. Rand, K.D., Pringle, S.D., Murphy III, J.P., Fadgen, K.E., Brown, J., Engen, J.R.: Gas-phase hydrogen/deuterium exchange in a traveling wave ion guide for the examination of protein conformations. Analytical chemistry. **81**, 10019-10028 (2009)
20. Konermann, L., Simmons, D.A.: Protein-folding kinetics and mechanisms studied by pulse-labeling and mass spectrometry. Mass spectrometry reviews. **22**, 1-26 (2003)
21. Bushnell, G.W., Louie, G.V., Brayer, G.D.: High-resolution three-dimensional structure of horse heart cytochrome c. Journal of Molecular Biology. **214**, 585-595 (1990)
22. Vaney, M., Maignan, S., Ries-Kautt, M., Ducruix, A.: High-resolution structure (1.33 Å) of a HEW lysozyme tetragonal crystal grown in the APCF apparatus. Data and structural comparison with a crystal grown under microgravity from SpaceHab-01 mission. Acta Crystallographica Section D: Biological Crystallography. **52**, 505-517 (1996)
23. Cotton, F.A., Wilkinson, G. Wiley New York, (1988)
24. Yoon, T.P., Ischay, M.A., Du, J.: Visible light photocatalysis as a greener approach to photochemical synthesis. Nature Chemistry. **2**, 527-532 (2010)
25. Adhikamsetty, R., Gollapalli, N., Jonnalagadda, S.: Complexation kinetics of Fe2+ with 1, 10-phenanthroline forming ferroin in acidic solutions. International Journal of Chemical Kinetics. **40**, 515-523 (2008)
26. Whitehouse, C.M., Dreyer, R., Yamashita, M., Fenn, J.: Electrospray ionization for mass-spectrometry of large biomolecules. Science. **246**, 64-71 (1989)
27. Smith, R.D., Loo, J.A., Edmonds, C.G., Barinaga, C.J., Udseth, H.R.: New developments in biochemical mass spectrometry: electrospray ionization. Analytical Chemistry. **62**, 882-899 (1990)
28. Wilm, M.S., Mann, M.: Electrospray and Taylor-Cone theory, Dole's beam of macromolecules at last? International Journal of Mass Spectrometry and Ion Processes. **136**, 167-180 (1994)
29. Mora, J.F.d.l., Van Berkel, G.J., Enke, C.G., Cole, R.B., Martinez-Sanchez, M., Fenn, J.B.: Electrochemical processes in electrospray ionization mass spectrometry. Journal of Mass Spectrometry. **35**, 939-952 (2000)
30. Duft, D., Achtzehn, T., Müller, R., Huber, B.A., Leisner, T.: Coulomb fission: Rayleigh jets from levitated microdroplets. Nature. **421**, 128-128 (2003)
31. Cech, N.B., Enke, C.G.: Practical implications of some recent studies in electrospray ionization fundamentals. Mass Spectrometry Reviews. **20**, 362-387 (2001)
32. Iribarne, J., Thomson, B.: On the evaporation of small ions from charged droplets. The Journal of Chemical Physics. **64**, 2287-2294 (1976)
33. Znamenskiy, V., Marginean, I., Vertes, A.: Solvated ion evaporation from charged water nanodroplets. The Journal of Physical Chemistry A. **107**, 7406-7412 (2003)
34. Dole, M., Mack, L., Hines, R., Mobley, R., Ferguson, L., Alice, M.d.: Molecular beams of macroions. The Journal of Chemical Physics. **49**, 2240-2249 (1968)
35. Hogan Jr, C.J., Carroll, J.A., Rohrs, H.W., Biswas, P., Gross, M.L.: Combined charged residue-field emission model of macromolecular electrospray ionization. Analytical chemistry. **81**, 369-377 (2008)

36. Konermann, L., Ahadi, E., Rodriguez, A.D., Vahidi, S.: Unraveling the mechanism of electrospray ionization. Analytical chemistry. **85**, 2-9 (2012)
37. Jacoby, M.: Doubling up on Mass Analysis Chemical and Engineering news. **88**, 35-37 (2010) https://pubs.acs.org/cen/coverstory/88/8813cover3.html
38. Hoffmann, E.d., Stroobant, V. Wiley, (2007)
39. Skoog, D.A., Holler, J.F., Crouch, S.R. Cengage Learning, (2007)
40. Henderson, W., McIndoe, S.J. John Wiley & Sons, Ltd, (2005)
41. Todd, J.F.: Recommendations for nomenclature and symbolism for mass spectroscopy (including an appendix of terms used in vacuum technology).(Recommendations 1991). Pure and applied chemistry. **63**, 1541-1566 (1991)
42. Eiceman, G.A., Karpas, Z., Hill Jr, H.H. CRC press, (2013)
43. Cumeras, R., Figueras, E., Davis, C., Baumbach, J.I., Gracia, I.: Review on ion mobility spectrometry. Part 1: current instrumentation. Analyst. **140**, 1376-1390 (2015)
44. Ruotolo, B.T., Benesch, J.L., Sandercock, A.M., Hyung, S.-J., Robinson, C.V.: Ion mobility–mass spectrometry analysis of large protein complexes. Nature Protocols. **3**, 1139-1152 (2008)
45. Waters: Travelling wave (T-wave): Waters. (2016) https://www.waters.com/waters/en_CA/Travelling-wave-%28T-Wave%E2%84%A2%29-/nav.htm?cid=134663694&locale=en_CA
46. Knapman, T.W., Berryman, J.T., Campuzano, I., Harris, S.A., Ashcroft, A.E.: Considerations in experimental and theoretical collision cross-section measurements of small molecules using travelling wave ion mobility spectrometry-mass spectrometry. International Journal of Mass Spectrometry. **298**, 17-23 (2010)
47. McLafferty, F.W.: Tandem mass spectrometry. Science. **214**, 280-287 (1981)
48. McLuckey, S.A.: Principles of collisional activation in analytical mass spectrometry. Journal of the American Society for Mass Spectrometry. **3**, 599-614 (1992)
49. Little, D.P., Speir, J.P., Senko, M.W., O'Connor, P.B., McLafferty, F.W.: Infrared multiphoton dissociation of large multiply charged ions for biomolecule sequencing. Analytical Chemistry. **66**, 2809-2815 (1994)
50. Zubarev, R.A., Kelleher, N.L., McLafferty, F.W.: Electron capture dissociation of multiply charged protein cations. A nonergodic process. Journal of the American Chemical Society. **120**, 3265-3266 (1998)
51. Gabelica, V., Pauw, E.D.: Internal energy and fragmentation of ions produced in electrospray sources. Mass spectrometry reviews. **24**, 566-587 (2005)
52. Mayer, P.M., Poon, C.: The mechanisms of collisional activation of ions in mass spectrometry. Mass spectrometry reviews. **28**, 608-639 (2009)
53. Rice, O.K., Ramsperger, H.C.: Theories of unimolecular gas reactions at low pressures. Journal of the American Chemical Society. **49**, 1617-1629 (1927)
54. Marcus, R.: Unimolecular dissociations and free radical recombination reactions. The Journal of Chemical Physics. **20**, 359-364 (1952)
55. McCormack, A.L., Schieltz, D.M., Goode, B., Yang, S., Barnes, G., Drubin, D., Yates, J.R.: Direct analysis and identification of proteins in mixtures by LC/MS/MS and database searching at the low-femtomole level. Analytical chemistry. **69**, 767-776 (1997)
56. Zhang, Z., Smith, D.L.: Determination of amide hydrogen exchange by mass spectrometry: a new tool for protein structure elucidation. Protein Science. **2**, 522-531 (1993)

57. Syka, J.E., Coon, J.J., Schroeder, M.J., Shabanowitz, J., Hunt, D.F.: Peptide and protein sequence analysis by electron transfer dissociation mass spectrometry. Proceedings of the National Academy of Sciences of the United States of America. **101**, 9528-9533 (2004)
58. Mann, M., Jensen, O.N.: Proteomic analysis of post-translational modifications. Nature biotechnology. **21**, 255-261 (2003)
59. Bond, A.M., Colton, R., D'Agostino, A., Traeger, J.C., Downard, A.J., Canty, A.J.: An electrospray mass spectrometric and voltammetric study of horse heart cytochrome c in the presence of metal ions. Inorganica chimica acta. **267**, 281-291 (1998)
60. Hu, P., Ye, Q.-Z., Loo, J.A.: Calcium stoichiometry determination for calcium binding proteins by electrospray ionization mass spectrometry. Analytical chemistry. **66**, 4190-4194 (1994)
61. Banerjee, S., Mazumdar, S.: Electrospray ionization mass spectrometry: a technique to access the information beyond the molecular weight of the analyte. International journal of analytical chemistry. **2012**, (2012)
62. Verkerk, U.H., Peschke, M., Kebarle, P.: Effect of buffer cations and of H3O+ on the charge states of native proteins. Significance to determinations of stability constants of protein complexes. Journal of mass spectrometry. **38**, 618-631 (2003)
63. Konermann, L., Douglas, D.: Acid-induced unfolding of cytochrome c at different methanol concentrations: electrospray ionization mass spectrometry specifically monitors changes in the tertiary structure. Biochemistry. **36**, 12296-12302 (1997)
64. Breuker, K., McLafferty, F.W.: Stepwise evolution of protein native structure with electrospray into the gas phase, 10− 12 to 102 s. Proceedings of the National Academy of Sciences. **105**, 18145-18152 (2008)
65. Ashcroft, A.E.: Recent developments in electrospray ionisation mass spectrometry: noncovalently bound protein complexes. Natural product reports. **22**, 452-464 (2005)
66. Dongre, A.R., Jones, J.L., Somogyi, Á., Wysocki, V.H.: Influence of peptide composition, gas-phase basicity, and chemical modification on fragmentation efficiency: Evidence for the mobile proton model. Journal of the American Chemical Society. **118**, 8365-8374 (1996)
67. Roepstorff, P., Fohlman, J.: Letter to the editors. Biological Mass Spectrometry. **11**, 601-601 (1984)
68. Tran, J.C., Zamdborg, L., Ahlf, D.R., Lee, J.E., Catherman, A.D., Durbin, K.R., Tipton, J.D., Vellaichamy, A., Kellie, J.F., Li, M.: Mapping intact protein isoforms in discovery mode using top-down proteomics. Nature. **480**, 254-258 (2011)
69. Kulasingam, V., Diamandis, E.P.: Proteomics Analysis of Conditioned Media from Three Breast Cancer Cell Lines A Mine for Biomarkers and Therapeutic Targets. Molecular & Cellular Proteomics. **6**, 1997-2011 (2007)
70. Katta, V., Chowdhury, S., Chait, B.: Electrospray ionization: a new tool for the analysis of ionic transition-metal complexes. Journal of The American Chemical Society. **112**, 5348–5349 (1990 )
71. Wilson, S.R., Wu, Y.: A Study of Nickel-Catalyzed Coupling Reactions by Electrospray Ionization Mass Spectrometry. Organometallics. **12**, 1478-1480 (1993)
72. Aliprantis, A.O., Canary, J.W.: Observation of Catalytic Intermediates in the Suzuki Reaction by Electrospray Mass Spectrometry Journal of the American Chemical Society. **116**, 6985-6986 (1994)
73. Lewars, E.G. Springer Science & Business Media, (2010)

74. University, W.S.: Potential energy surfaces, Model chemistries, Asking the right questions. http://www.chem.wayne.edu/~hbs/chm6440/PES.html
75. Hohenberg, P., Kohn, W.: Inhomogeneous electron gas. Physical review. **136**, B864 (1964)
76. Kohn, W., Sham, L.J.: Self-consistent equations including exchange and correlation effects. Physical review. **140**, A1133 (1965)
77. Density Functional theory. http://www.iue.tuwien.ac.at/phd/goes/dissse14.html
78. Konermann, L., Douglas, D.: Unfolding of proteins monitored by electrospray ionization mass spectrometry: a comparison of positive and negative ion modes. Journal of the American Society for Mass Spectrometry. **9**, 1248-1254 (1998)
79. Harrison, A.G., Young, A.B., Bleiholder, C., Suhai, S., Paizs, B.: Scrambling of sequence information in collision-induced dissociation of peptides. Journal of the American Chemical Society. **128**, 10364-10365 (2006)
80. Katta, V., Chait, B.T., Carr, S.: Conformational changes in proteins probed by hydrogen? exchange electrospray? ionization mass spectrometry. Rapid Communications in Mass Spectrometry. **5**, 214-217 (1991)
81. Vijay-Kumar, S., Bugg, C.E., Cook, W.J.: Structure of ubiquitin refined at 1.8 Åresolution. Journal of molecular biology. **194**, 531-544 (1987)
82. Shi, H., Pierson, N.A., Valentine, S.J., Clemmer, D.E.: Conformation types of ubiquitin [M+ 8H] 8+ ions from water: methanol solutions: evidence for the N and A states in aqueous solution. The Journal of Physical Chemistry B. **116**, 3344-3352 (2012)
83. Brutscher, B., Brüschweiler, R., Ernst, R.R.: Backbone dynamics and structural characterization of the partially folded A state of ubiquitin by 1H, 13C, and 15N nuclear magnetic resonance spectroscopy. Biochemistry. **36**, 13043-13053 (1997)
84. Blake, C., Koenig, D., Mair, G., North, A., Phillips, D., Sarma, V.: Structure of hen egg-white lysozyme. A three-dimensional Fourier synthesis at 2 Angstrom resolution. Nature. 757-761 (1965)
85. Valentine, S.J., Anderson, J.G., Ellington, A.D., Clemmer, D.E.: Disulfide-intact and-reduced lysozyme in the gas phase: conformations and pathways of folding and unfolding. The Journal of Physical Chemistry B. **101**, 3891-3900 (1997)
86. Bushnell, G.W., Louie, G.V., Brayer, G.D.: High-resolution three-dimensional structure of horse heart cytochrome c. J Mol Biol. **214**, 585-595 (1990)
87. Zhang, Y., Marcillat, O., Giulivi, C., Ernster, L., Davies, K.: The oxidative inactivation of mitochondrial electron transport chain components and ATPase. Journal of Biological Chemistry. **265**, 16330-16336 (1990)
88. Wood, T.D., Chorush, R.A., Wampler, F.M., Little, D.P., O'Connor, P.B., McLafferty, F.W.: Gas-phase folding and unfolding of cytochrome c cations. Proceedings of the National Academy of Sciences. **92**, 2451-2454 (1995)
89. Fink, A.L., Calciano, L.J., Goto, Y., Kurotsu, T., Palleros, D.R.: Classification of acid denaturation of proteins: intermediates and unfolded states. Biochemistry. **33**, 12504-12511 (1994)
90. Shou, W.Z., Naidong, W.: Simple means to alleviate sensitivity loss by trifluoroacetic acid (TFA) mobile phases in the hydrophilic interaction chromatography–electrospray tandem mass spectrometric (HILIC–ESI/MS/MS) bioanalysis of basic compounds. Journal of Chromatography B. **825**, 186-192 (2005)

91. Apffel, A., Fischer, S., Goldberg, G., Goodley, P.C., Kuhlmann, F.E.: Enhanced sensitivity for peptide mapping with electrospray liquid chromatography-mass spectrometry in the presence of signal suppression due to trifluoroacetic acid-containing mobile phases. Journal of chromatography A. **712**, 177-190 (1995)
92. Katta, V., Chowdhury, S.K., Chait, B.T.: Electrospray ionization: a new tool for the analysis of ionic transition-metal complexes. Journal of the American Chemical Society. **112**, 5348-5349 (1990)
93. McNeill, E., Scholer, F.: Molecular structure of the gaseous metal carbonyl hydrides of manganese, iron, and cobalt. Journal of the American Chemical Society. **99**, 6243-6249 (1977)
94. Calligaris, M.: Structure and bonding in metal sulfoxide complexes: an update. Coordination chemistry reviews. **248**, 351-375 (2004)

# Appendix

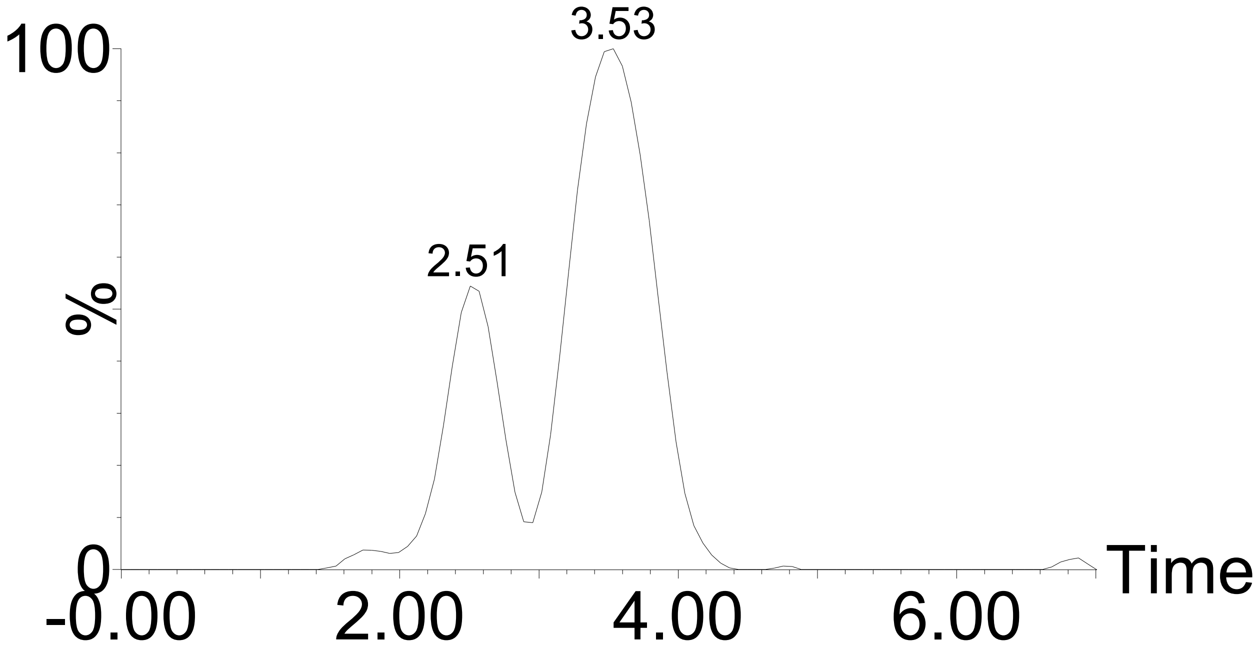

**Figure S1.** Ion mobility chromatogram of oxytocin monomer $[M+H]^+$ (3.53 ms) and the oxytocin dimer $[2M + 2H]^{2+}$ (2.51 ms).

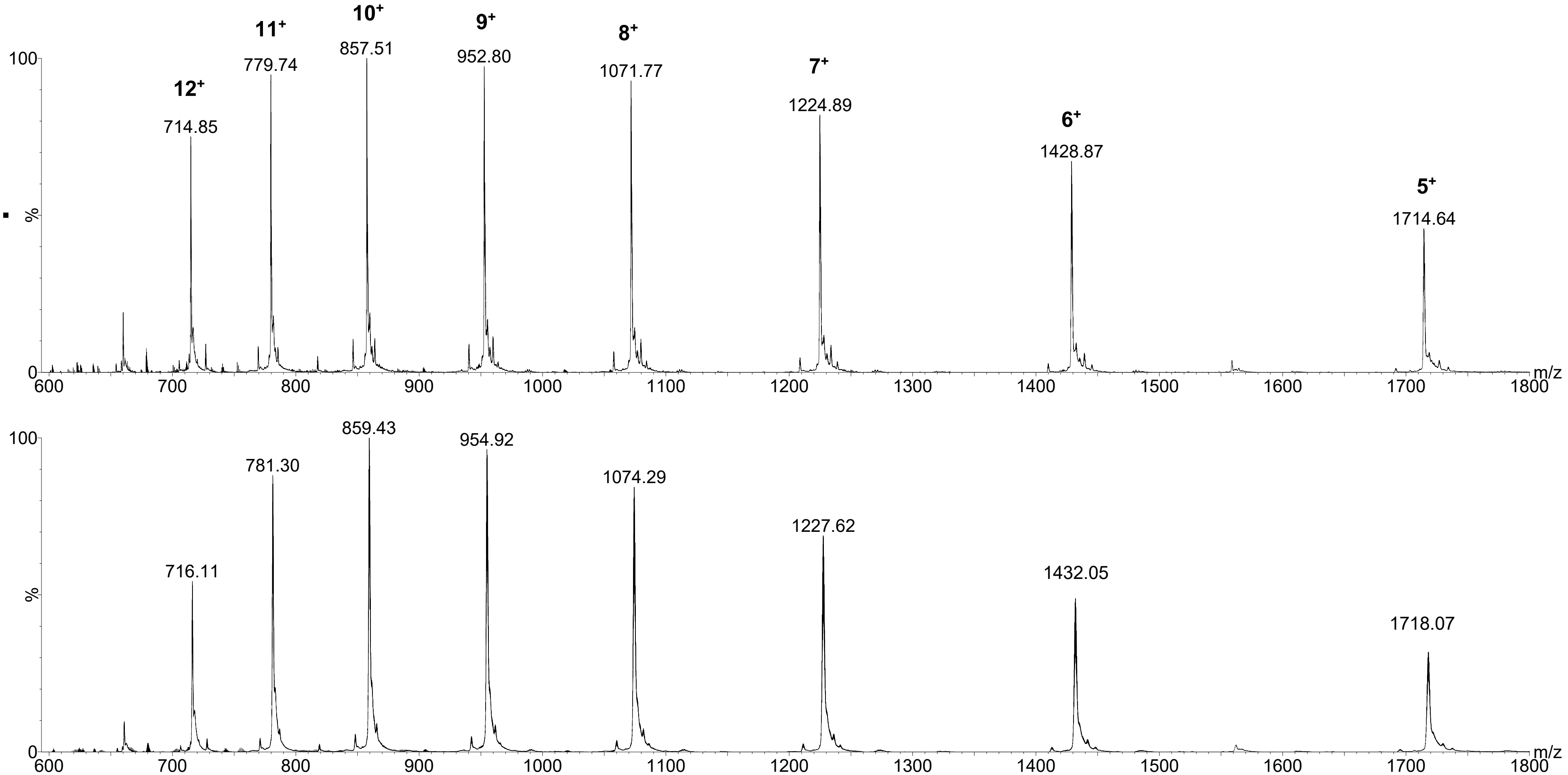

**Figure S2.** ESI charge state distribution of denatured ubiquitin in 50:45:5 $H_2O$, MeOH, $CH_3COOH$ (top panel). Dual-spray HDX reaction of denatured ubiquitin showing shift in mass for all charge states (bottom panel).

**Table S1**. Average deuterium exchanges observed in the dual-spray HDX reaction of native and denatured ubiquitin. Dominant charge states are indicated by asterisks.

| **Native Ubiquitin** | | **Unfolded Ubiquitin** | |
|---|---|---|---|
| Charge state | Average deuterium exchanges (± 0.5) | Charge state | Average deuterium exchanges (± 0.5) |
| 5 | 18.3 | 5 | 18.1 |
| 6* | 18.18 | 6 | 19.08 |
| 7* | 20.3 | 7 | 18.06 |
| 8* | 18.24 | 8 | 20.16 |
| 9 | 19.26 | 9* | 20.07 |
| 10 | 19.2 | 10* | 20.1 |
| 11 | 18.26 | 11* | 17.16 |
| 12 | 14.16 | 12 | 15.12 |
| 13 | 12.09 | 13 | 12.09 |

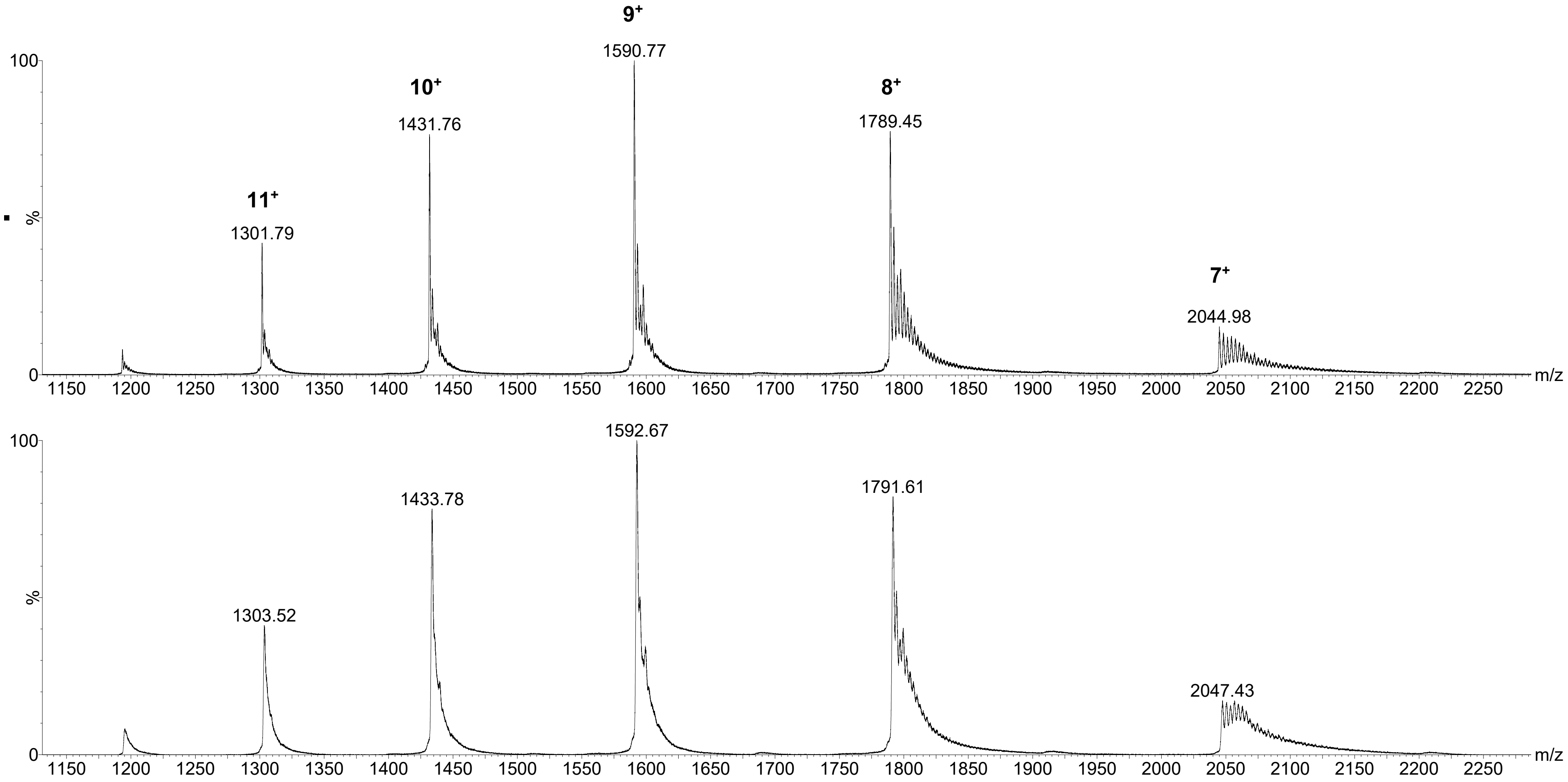

**Figure S3.** ESI charge state distribution of native lysozyme in 95:5 water, $CH_3COOH$ (top panel). Dual-spray HDX reaction of native lysozyme showing shift in mass for all charge states (bottom panel).

**Table S2**. Average deuterium exchanges observed in the dual-spray HDX reaction of native and denatured lysozyme. Dominant charge states are indicated by asterisks.

| **Native Lysozyme** | | **Denatured Lysozyme** | |
|---|---|---|---|
| Charge state | Average deuterium exchanges (± 0.5) | Charge state | Average deuterium exchanges (± 0.5) |
| 7 | 17.15 | 7 | - |
| 8* | 17.04 | 8 | - |
| 9* | 17.1 | 9 | 16.83 |
| 10* | 20.2 | 10 | 17.1 |
| 11 | 19.03 | 11 | 18.15 |
| 12 | 20.16 | 12 | 18.12 |
| 13 | - | 13 | 18.07 |
| 14 | - | 14* | 18.34 |
| 15 | - | 15* | 19.05 |
| 16 | - | 16* | 19.04 |
| 17 | - | 17 | 20.4 |
| 18 | - | 18 | 23.22 |
| 19 | - | 19 | 23.18 |

**Table S3**. Average deuterium exchanges observed in the dual-spray HDX reaction of native and denatured cytochrome *c*. Dominant charge states are indicated by asterisks.

| **Native cytochrome *c*** | | **Denatured cytochrome *c*** | |
|---|---|---|---|
| Charge | Average deuterium exchanges ± 0.5 | Charge | Average deuterium exchanges ± 0.5 |
| 6 | 34.32 | 6 | 29.46 |
| 7* | 34.3 | 7 | 27.23 |
| 8 | 34.08 | 8 | 31.44 |
| 9 | - | 9 | 34.38 |
| 10 | - | 10 | 36 |
| 11 | - | 11 | 37.07 |
| 12 | - | 12 | 38.4 |
| 13 | - | 13* | 38.35 |
| 14 | - | 14* | 39.34 |
| 15 | - | 15* | 39.3 |
| 16 | - | 16 | 38.4 |
| 17 | - | 17 | 36.38 |
| 18 | - | 18 | 33.48 |
| 19 | - | 19 | 32.3 |

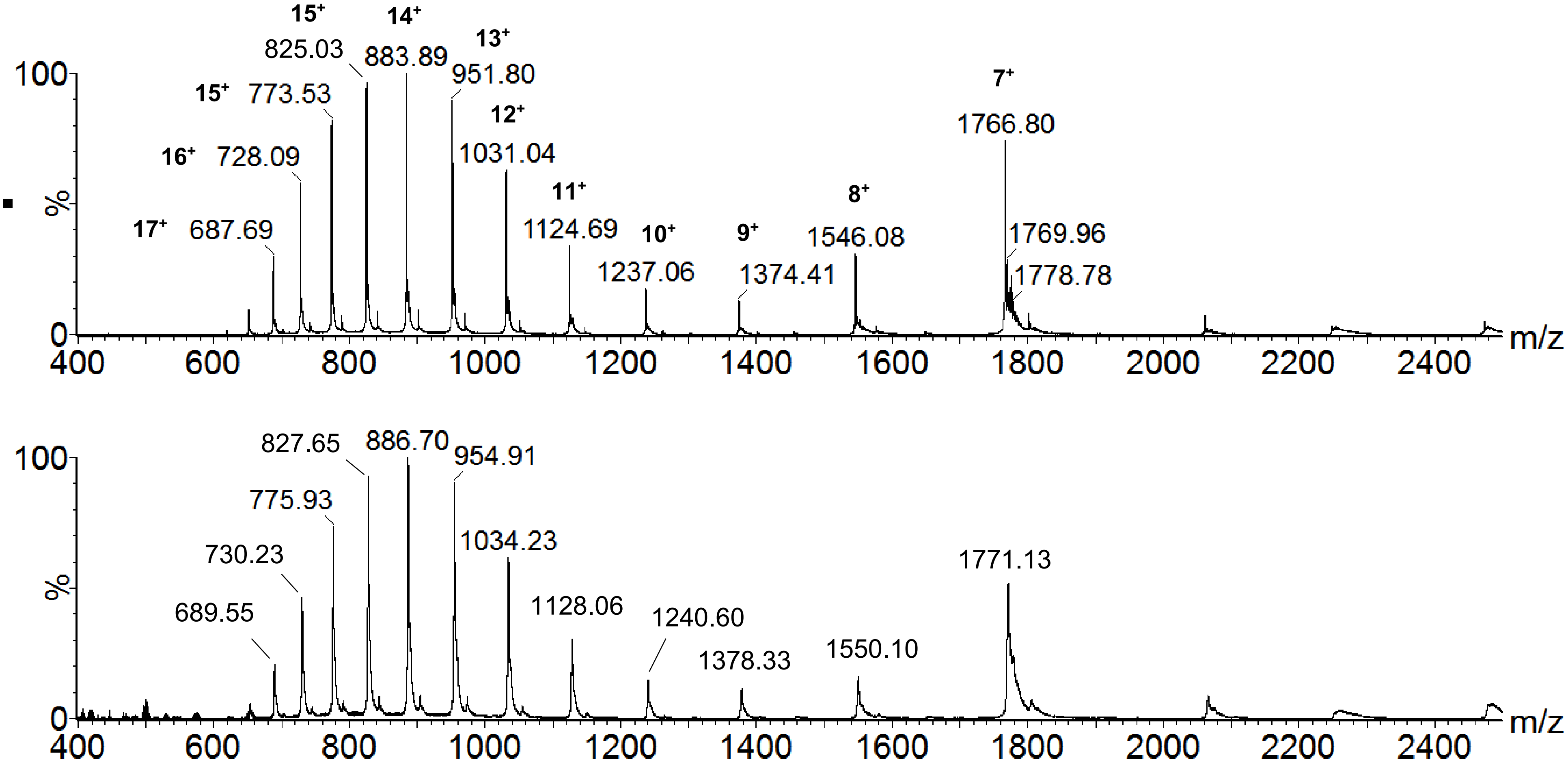

**Figure S4.** ESI charge state distribution of denatured cytochrome *c* in 3% MeOH in $H_2O$, 1 mM ammonium formate, acidified with formic acid to pH 3 (top panel). Dual-spray HDX reaction of denatured cytochrome *c* showing shift in mass for all charge states (bottom panel).

**Table S4**. Optimal ESI parameters for the complexes [Ru(bpy)$_3$]$^{2+}$, [Ru(phen)$_3$]$^{2+}$, [Fe(bpy)$_3$]$^{2+}$, and [Fe(phen)$_3$]$^{2+}$. Also shown are the in-source CID parameters for the di-ligated complexes.

| | **[Ru(bpy)$_3$]$^{2+}$** | **[Ru(phen)$_3$]$^{2+}$** | **[Fe(bpy)$_3$]$^{2+}$** | **[Fe(phen)$_3$]$^{2+}$** |
|---|---|---|---|---|
| Capillary (kV) | 2.5 | 3.2 | 2.8 | 2.9 |
| Sampling cone (V) | -46.0 | -52.0 | -23.0 | -19.0 |
| Extraction cone (V) | 4.0 | 4.0 | 4.0 | 4.0 |
| Desolvation gas flow (L/Hr) | 176.0 | 176.0 | 176.0 | 176.0 |
| Desolvation temperature (ºC) | 180 | 180 | 150 | 150 |
| Source Temperature (ºC) | 85 | 80 | 80 | 85 |
| In-source CID (di-ligated complexes) | | | | |
| | **[Ru(bpy)$_2$]$^{2+}$** | **[Ru(phen)$_2$]$^{2+}$** | **[Fe(bpy)$_2$]$^{2+}$** | **[Fe(phen)$_2$]$^{2+}$** |
| Capillary (kV) | 3.6 | 3.1 | 3.0 | 3.2 |
| Sampling cone (V) | -52.0 | -72.0 | -55.0 | -50.0 |
| Extraction cone (V) | 4.0 | 4.0 | 4.0 | 4.0 |
| Desolvation gas flow (L/Hr) | 176.0 | 176.0 | 176.0 | 176.0 |
| Desolvation temperature (ºC) | 180 | 180 | 150 | 150 |
| Source Temperature (ºC) | 85 | 80 | 80 | 85 |

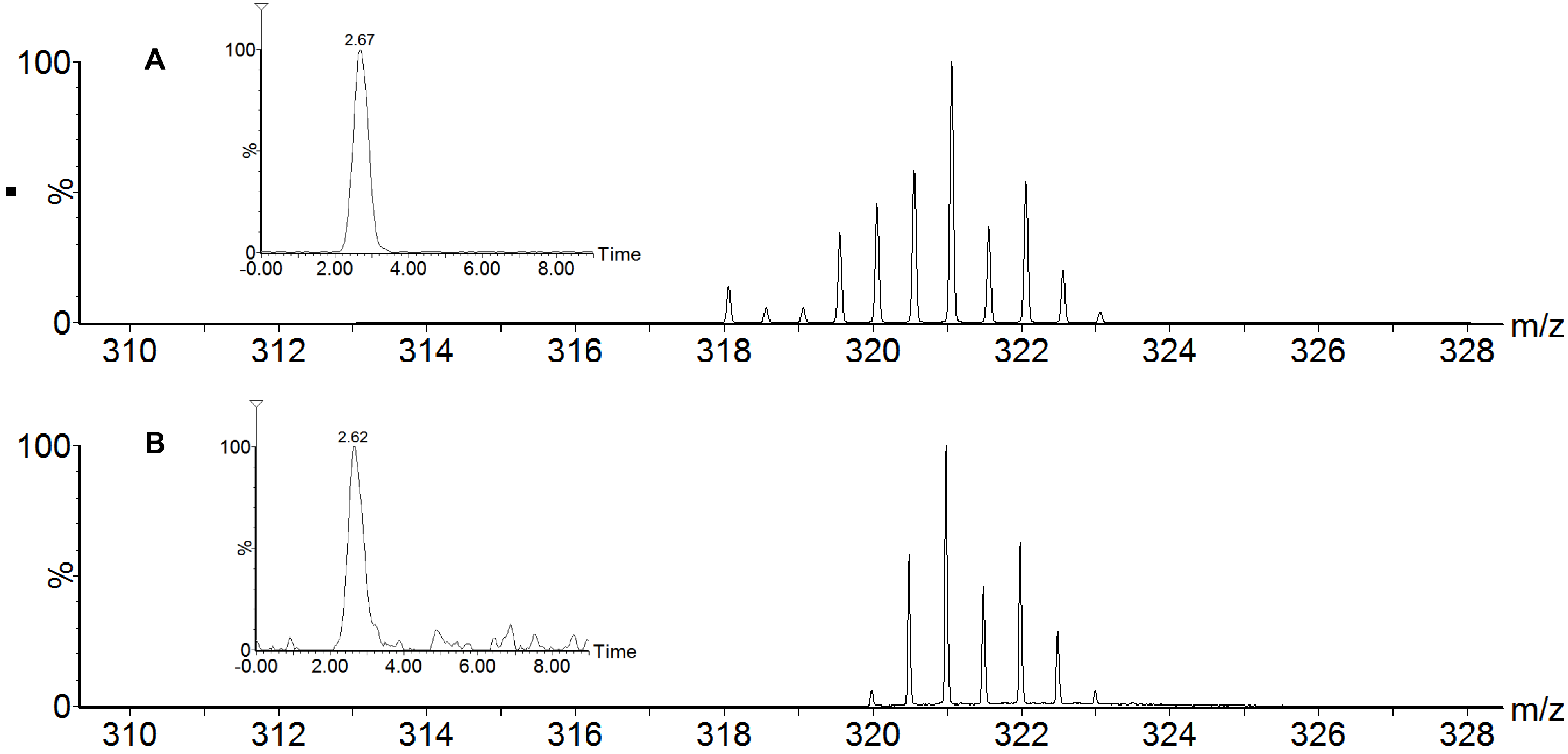

**Figure S5.** (**A**) Mass spectrum of $[Ru(phen)_3]^{2+}$ reference standard indicating the isotopic distribution for the complex, the inset shows the ion mobility drift time distribution for the $[Ru(phen)_3]^{2+}$ reference standard. (**B**) Mass spectrum and ion mobility drift time distribution of the dual-spray product while electrospraying solutions of 1,10-phenantroline and $RuCl_3$ and setting the resolving quadrupole to m/z 321.

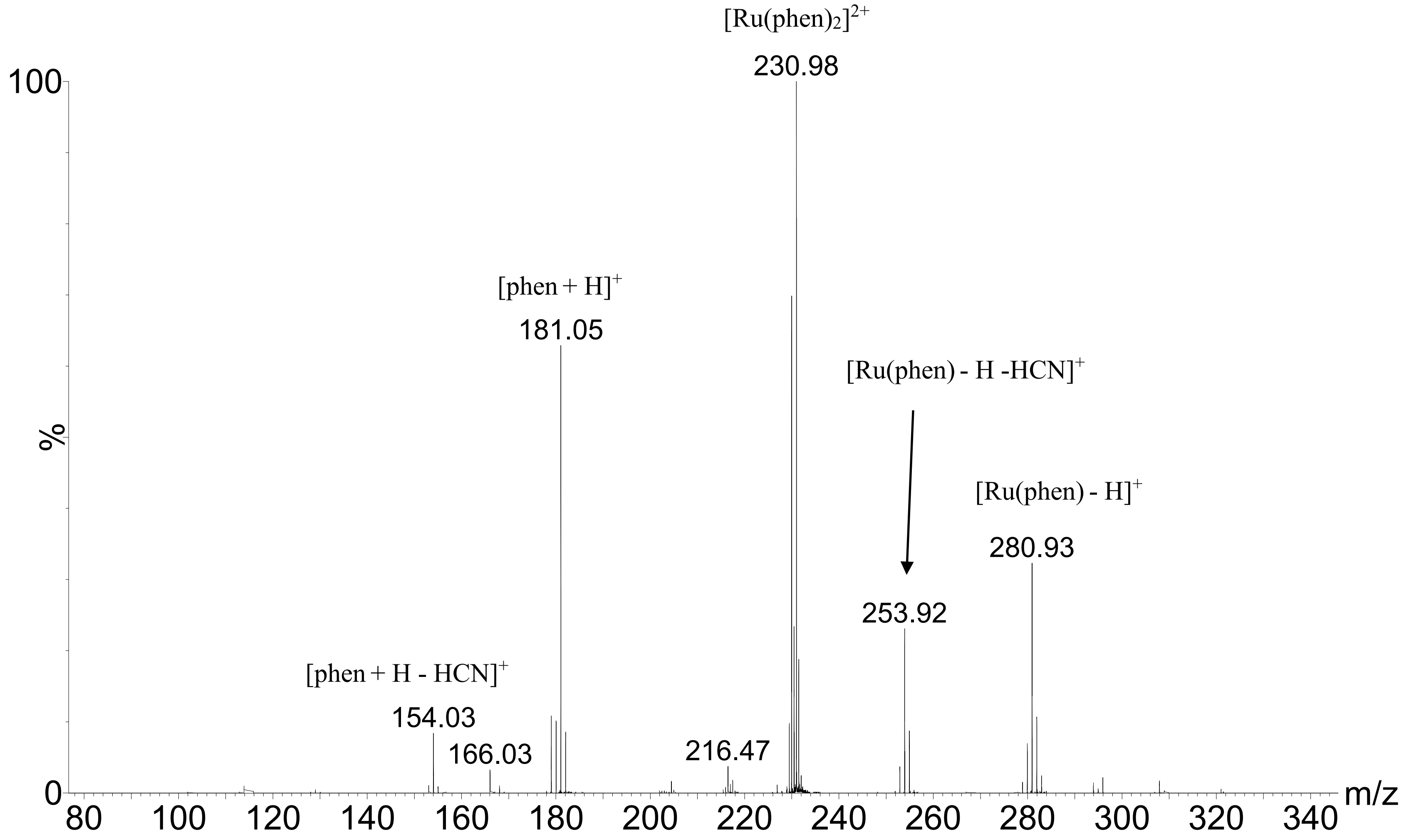

**Figure S6.** CID of $[Ru(phen)_3]^{2+}$ (m/z 321) at $E_{com} = 6.56$ eV. Fragment ions generated are labelled.

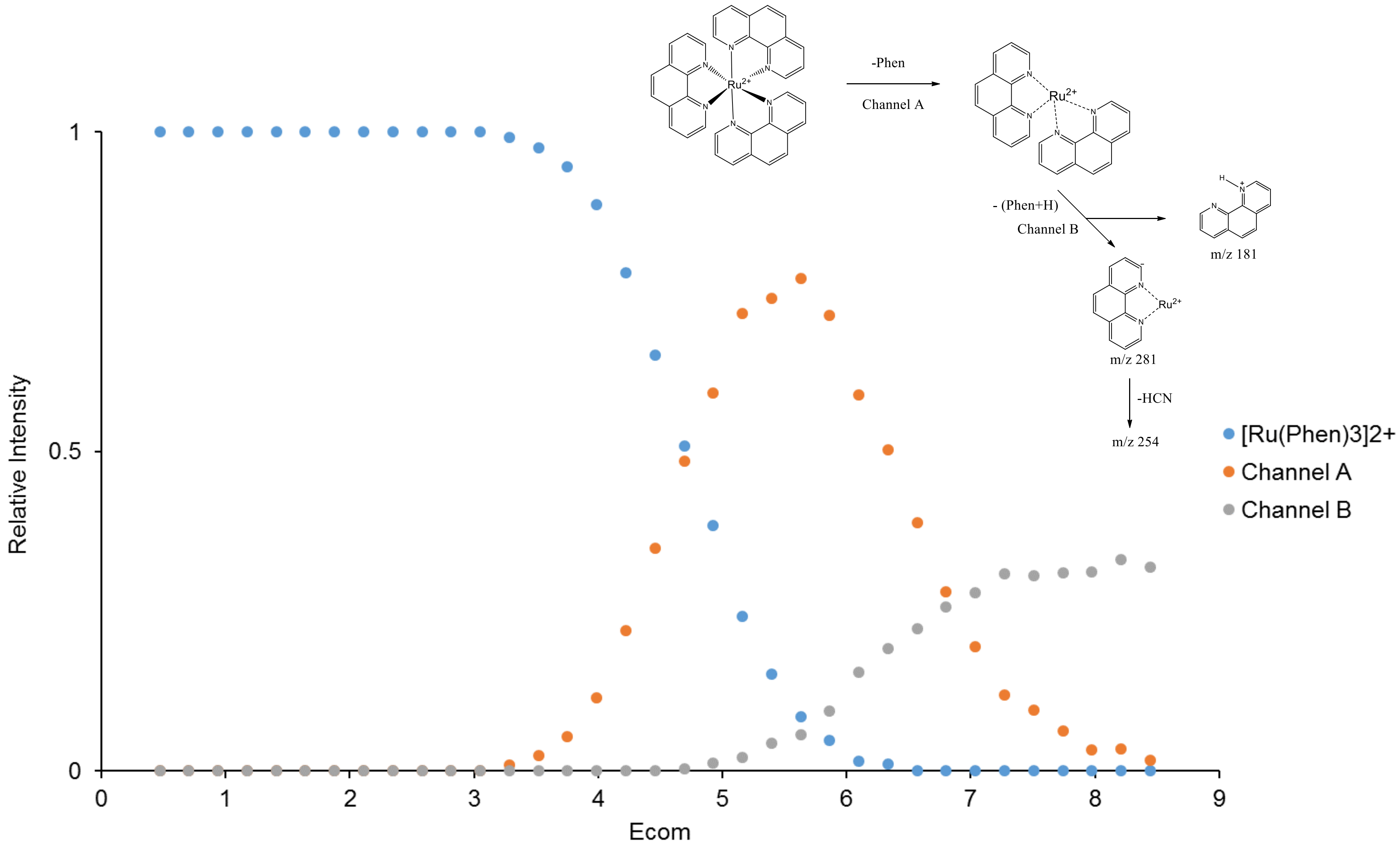

**Figure S7.** Breakdown curve for $[Ru(phen)_3]^{2+}$. Also shown is the fragmentation mechanism. Channel A corresponds to the intensity of $[Ru(phen)_2]^{2+}$. Channel B represents the average intensity of $[Ru(phen) - H]^+$, $[Ru(phen) - H -HCN]^+$, and $[phen + H]^+$

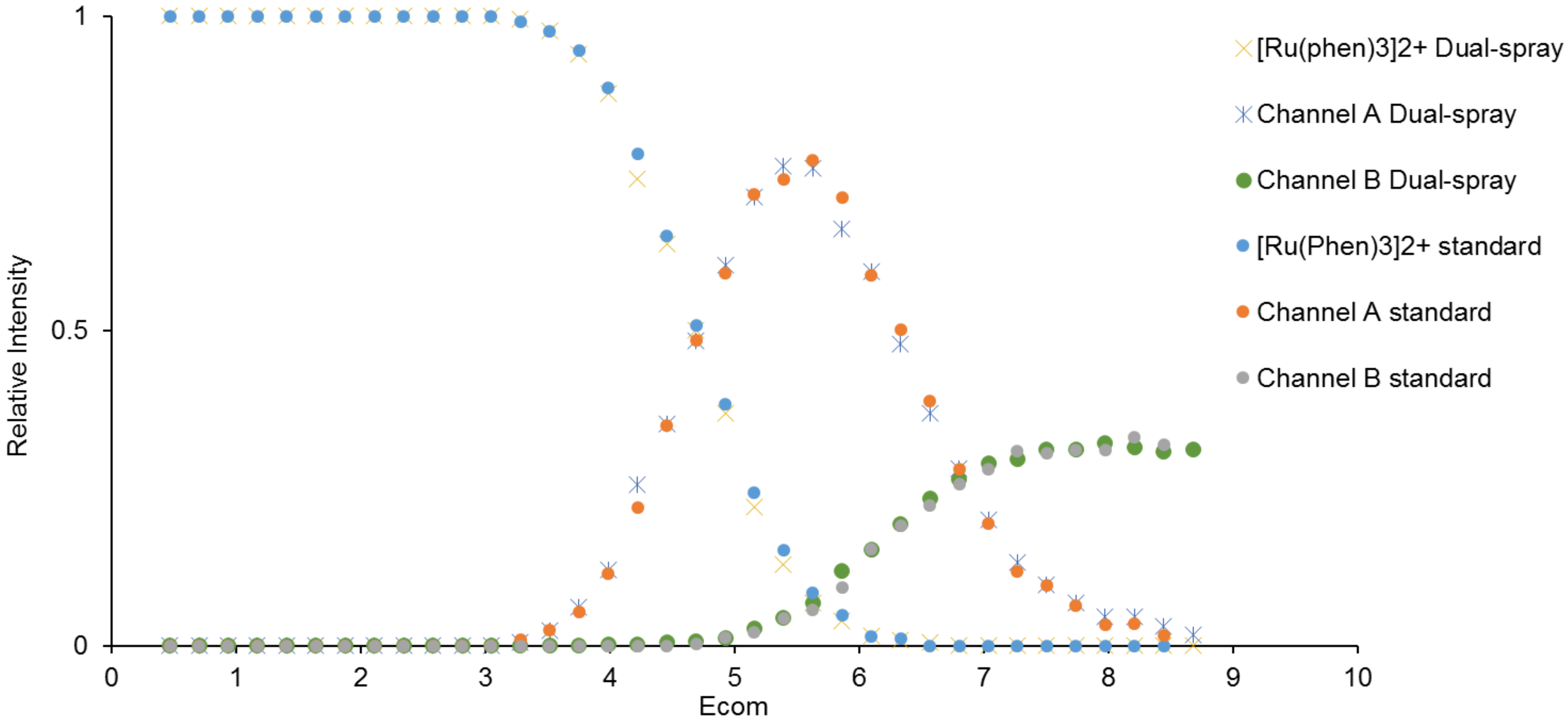

**Figure S8.** Overlapping breakdown curves for [Ru(phen)$_3$]$^{2+}$ standard and complex formed by dual-spray.

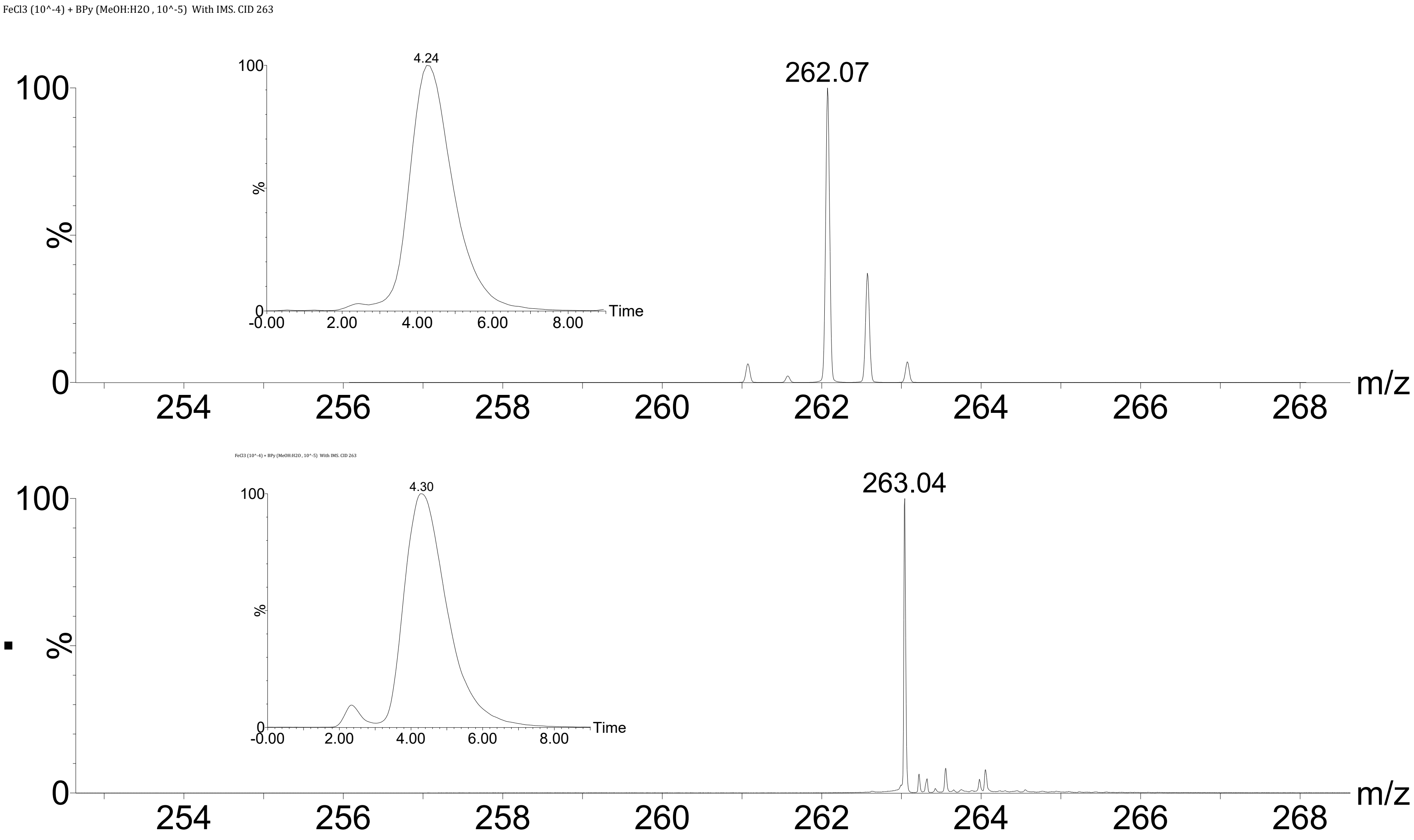

**Figure S9.** (**A**) Mass spectrum of $[Fe(bpy)_3]^{2+}$ reference standard indicating the isotopic distribution for the complex, the inset shows the ion mobility drift time distribution for the $[Fe(bpy)_3]^{2+}$ reference standard. (**B**) Mass spectrum and ion mobility drift time distribution of the dual-spray product while electrospraying solutions of 2,2-bipyridine and $FeSO_4$ and setting the resolving quadrupole to m/z 263.

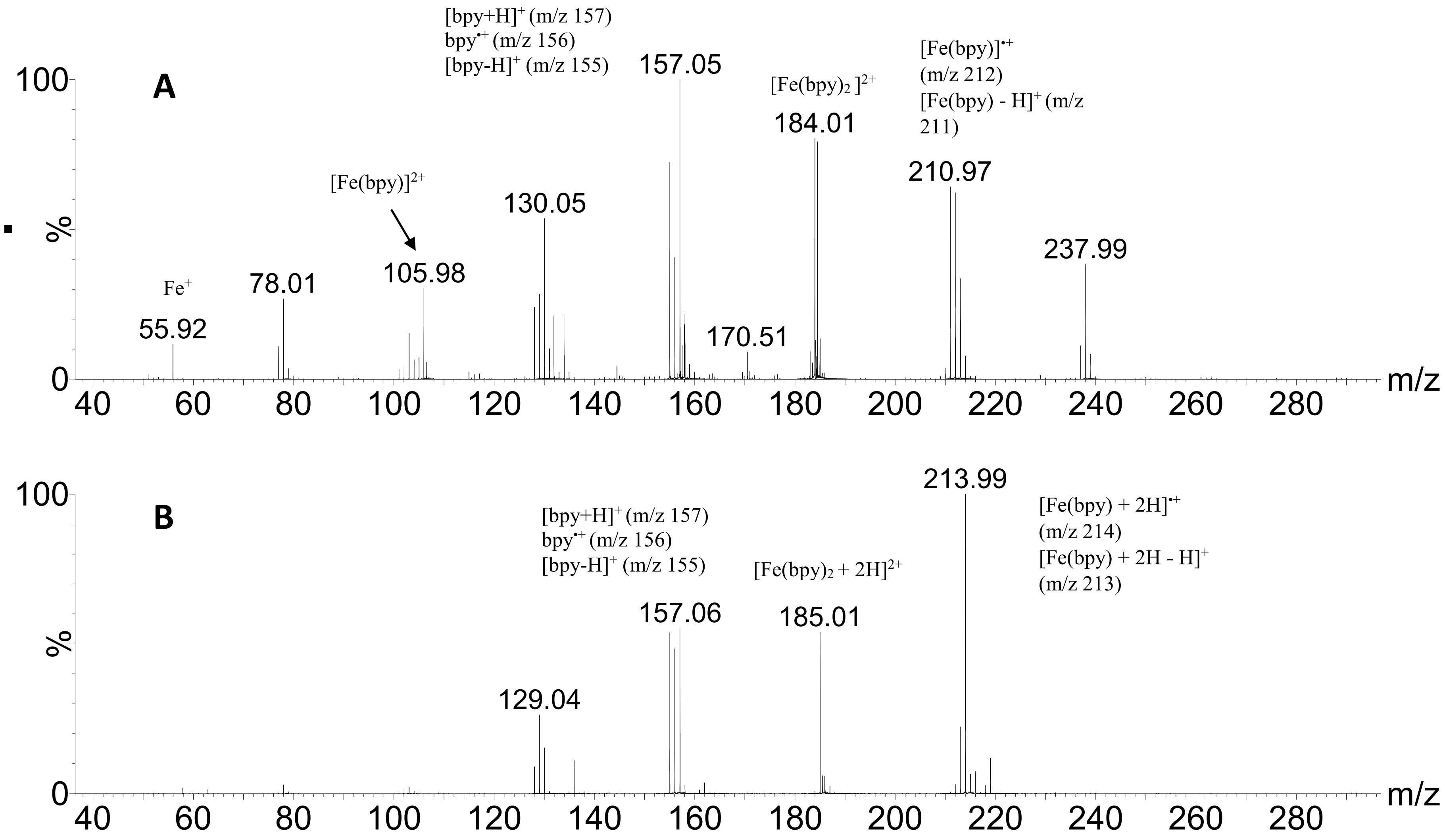

**Figure S10. (A)** CID of $[Fe(Bpy)_3]^{2+}$ (m/z 262) at $E_{com}$ = 7.37 eV. **(B)** CID of $[Fe(Bpy)_3 + 2H]^{2+}$ (m/z 263) at $E_{com}$ = 7.06 eV.

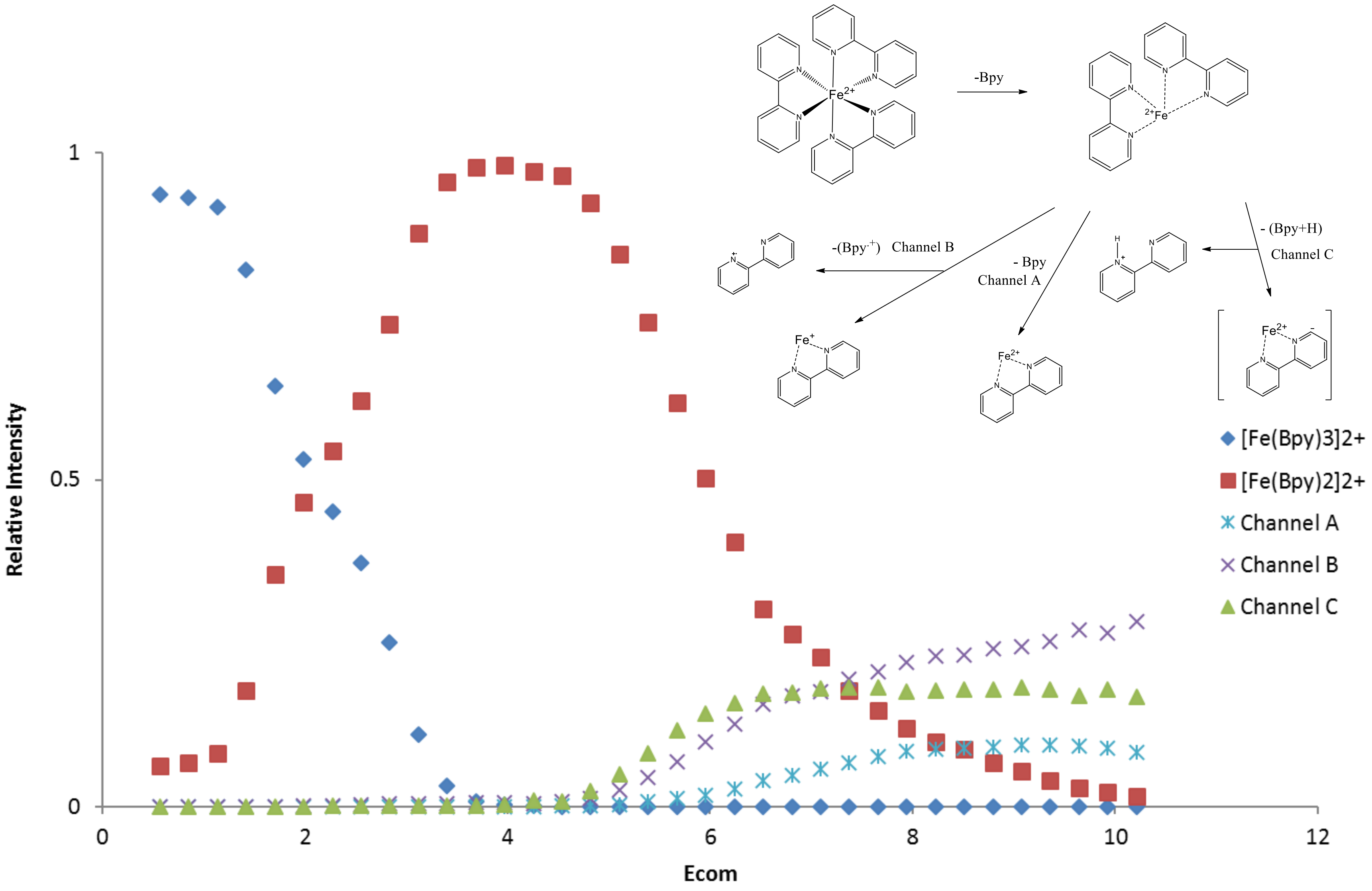

**Figure S11.** Breakdown curve for $[Fe(bpy)_3]^{2+}$. Also shown is the fragmentation mechanism. Channel A corresponds to the intensity of $[Fe(bpy)]^{2+}$. Channel B represents the average intensity of $[Fe(bpy)]^{\bullet+}$, $bpy^{\bullet+}$, and $[bpy - H]^{+}$ Channel C corresponds to the average intensity of $[Fe(bpy) - H]^{+}$ and $[bpy + H]^{+}$.

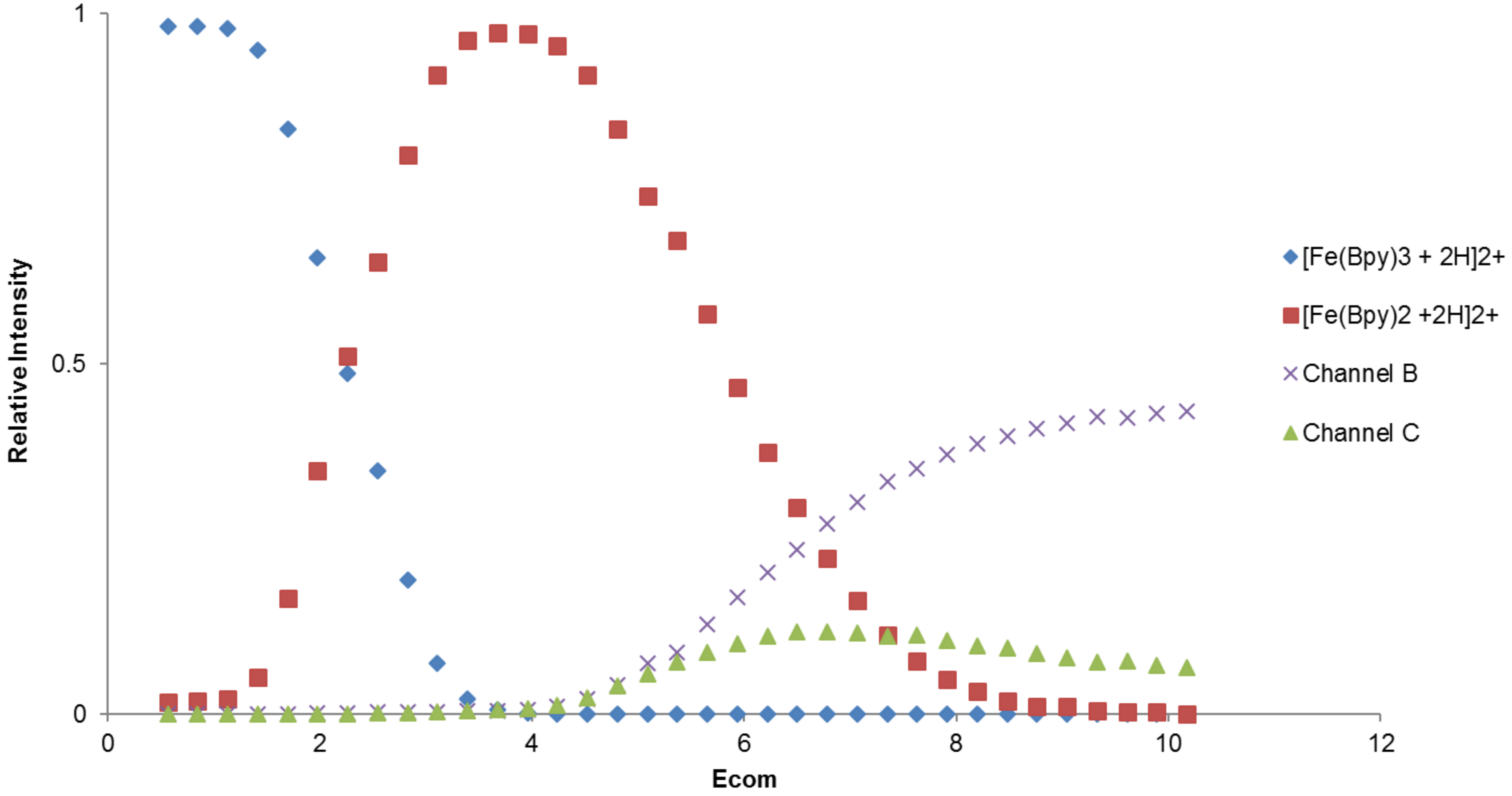

**Figure S12.** Breakdown curve for $[Fe(bpy)_3 + 2H]^{2+}$. Channel B represents the average intensity of $[Fe(bpy)]^{\bullet+}$, $bpy^{\bullet+}$, and $[bpy – H]^{+}$. Channel C corresponds to the average intensity of $[Fe(bpy) - H]^{+}$ and $[bpy + H]^{+}$.

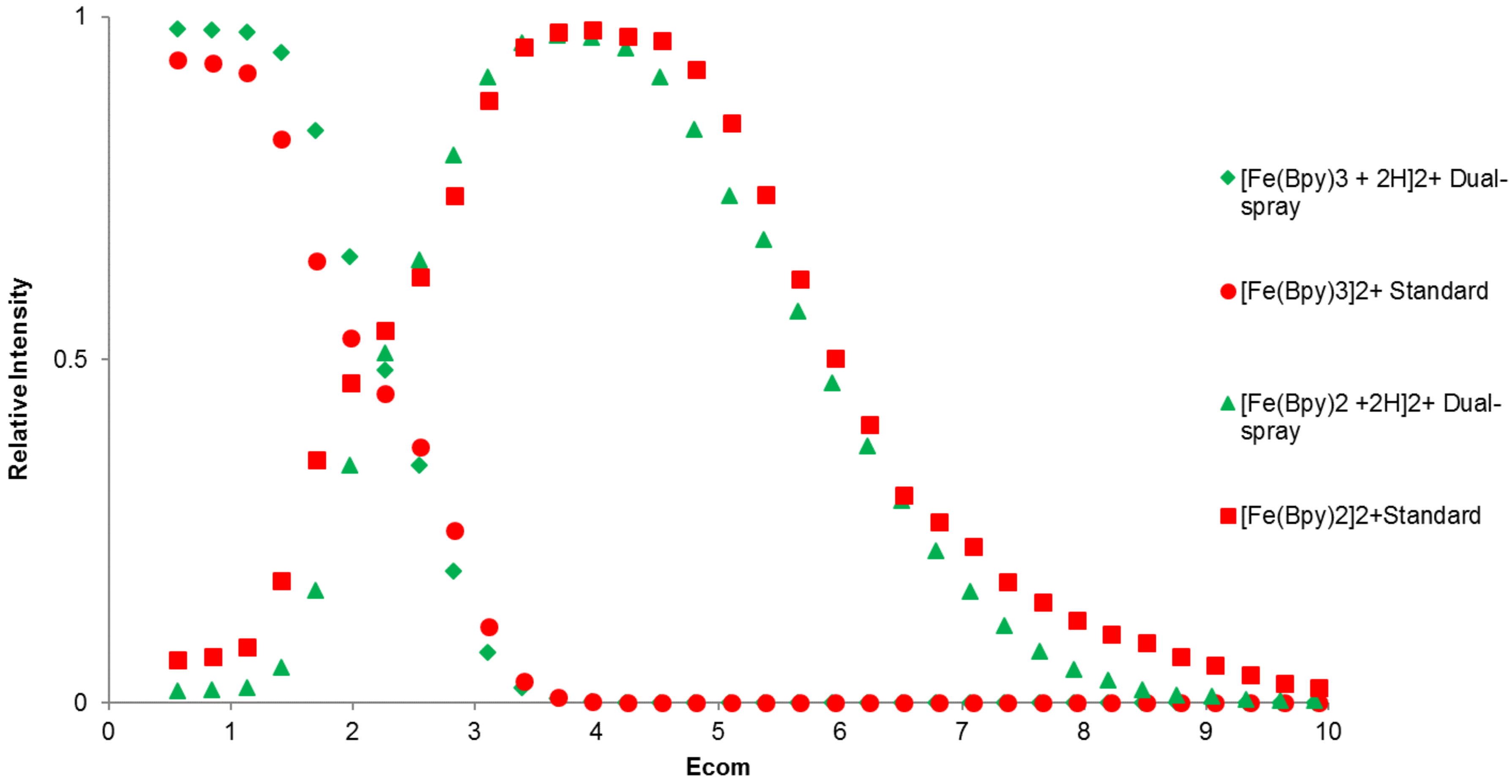

**Figure S13.** Overlapping breakdown curves for $[Fe(bpy)_3]^{2+}$ reference standard and the dual-spray product $[Fe(bpy)_3 + 2H]^{2+}$.

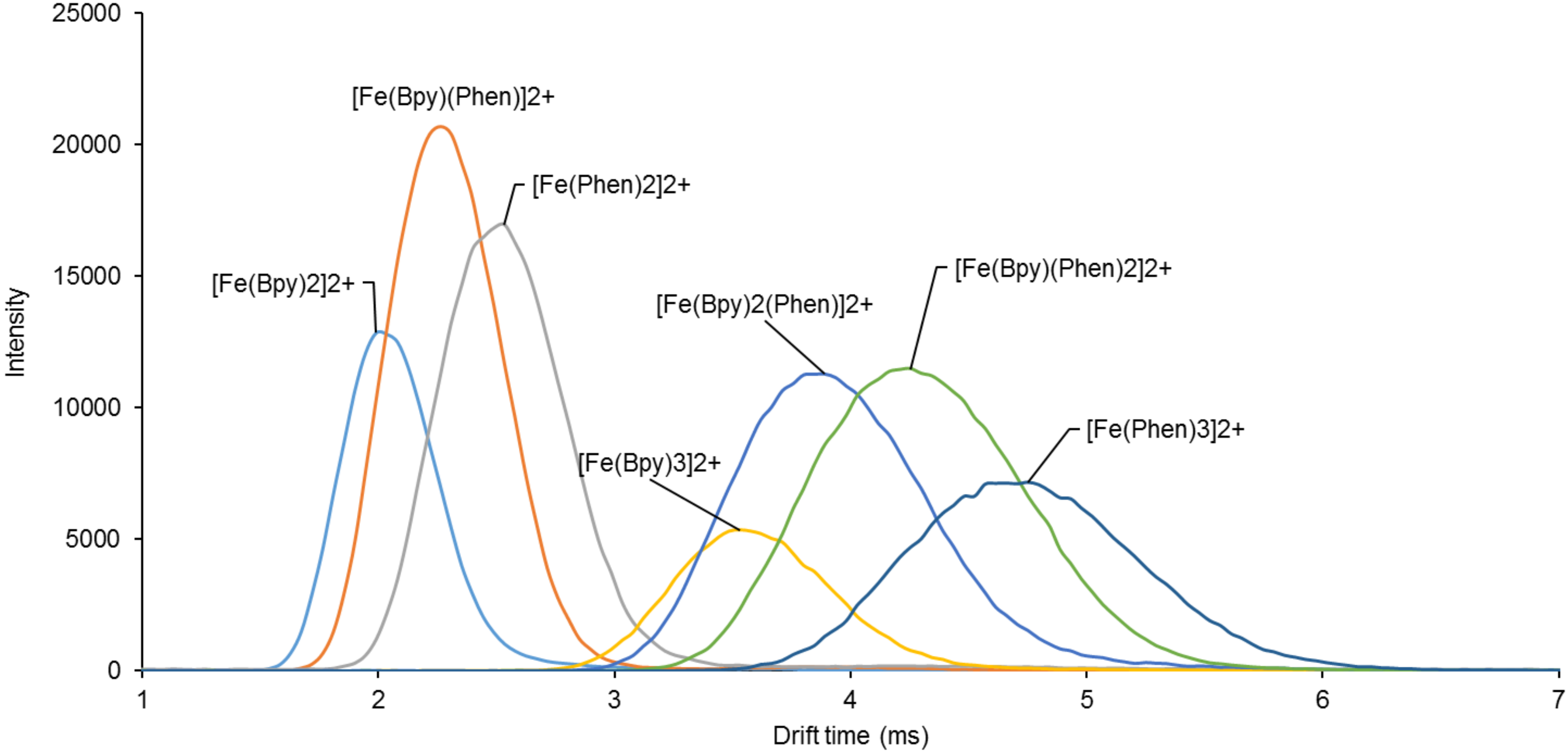

**Figure S14.** Ion mobility drift time distributions for all iron complexes generated in methanolic solution containing 20 μM $FeSO_4$, 1 μM 1,10-Phenanthroline, and 1 μM 2,2'-bipydine.

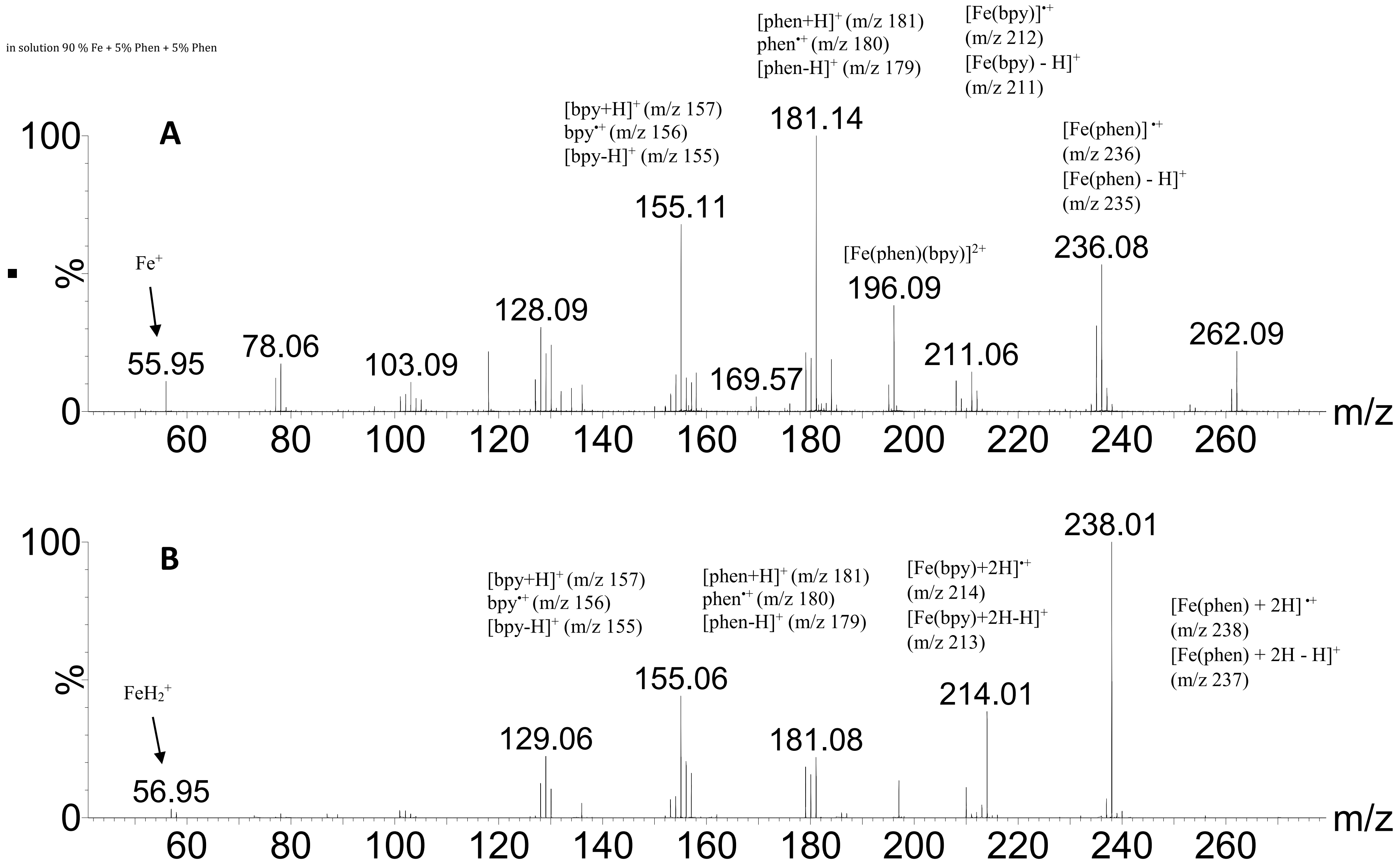

**Figure S15.** **(A)** CID of diligated $[Fe(phen)(bpy)]^{2+}$ (m/z 196) at $E_{com} = 3.70$ eV. **(B)** CID of dual-spray product $[Fe(phen)(bpy) + 2H]^{2+}$ (m/z 197) at $E_{com} = 3.33$ eV.